

Spring 2017

Behavior and Strength of RC Spandrel Members Under Unsymmetrical Bending and Torsion Including CFRP Retrofitting

Muhammad Fahim
Old Dominion University

Follow this and additional works at: https://digitalcommons.odu.edu/cee_etds

 Part of the [Civil Engineering Commons](#), and the [Structural Materials Commons](#)

Recommended Citation

Fahim, Muhammad. "Behavior and Strength of RC Spandrel Members Under Unsymmetrical Bending and Torsion Including CFRP Retrofitting" (2017). Doctor of Philosophy (PhD), dissertation, Civil/Environmental Engineering, Old Dominion University, DOI: 10.25777/qts4-z016
https://digitalcommons.odu.edu/cee_etds/16

This Dissertation is brought to you for free and open access by the Civil & Environmental Engineering at ODU Digital Commons. It has been accepted for inclusion in Civil & Environmental Engineering Theses & Dissertations by an authorized administrator of ODU Digital Commons. For more information, please contact digitalcommons@odu.edu.

**BEHAVIOR AND STRENGTH OF RC SPANDREL MEMBERS UNDER
UNSYMMETRICAL BENDING AND TORSION INCLUDING CFRP
RETROFITTING**

by

Muhammad Fahim

B.Sc. November 2007, University of Engineering and Technology, Peshawar, Pakistan
M.Sc. May 2010, University of Engineering and Technology, Peshawar, Pakistan

A Dissertation Submitted to the Faculty of
Old Dominion University in Partial Fulfillment of the
Requirements for the Degree of

DOCTOR OF PHILOSOPHY

CIVIL AND ENVIRONMENTAL ENGINEERING

OLD DOMINION UNIVERISTY
May 2017

Approved by:

Zia Razzaq (Director)

Duc T. Nguyen (Member)

Julie Z. Hao (Member)

Mojtaba B. Sirjani (Member)

ABSTRACT

BEHAVIOR AND STRENGTH OF RC SPANDREL MEMBERS UNDER UNSYMMETRICAL BENDING AND TORSION INCLUDING CFRP RETROFITTING

Muhammad Fahim
Old Dominion University, 2017
Director: Dr. Zia Razzaq

This dissertation presents the outcome of an experimental and theoretical investigation of the behavior and strength of reinforced concrete spandrel members both with and without carbon fiber reinforced polymer (CFRP) retrofitting. Both isolated spandrel members with L-shaped cross section as well as those integrated with reinforced concrete slabs are studied. A series of isolated spandrel members were tested under separate and combined actions of unsymmetrical bending and torsion. Six of these specimens were retrofitted externally with high-strength CFRP strips. Materially nonlinear analysis procedures are also formulated and programmed for the spandrel members with and without CFRP retrofitting. Furthermore, ultimate bending-torsion interaction expressions for the spandrel members are developed including the influence of CFRP retrofitting. Tests are also conducted on three slab-beam systems up to their load-carrying capacities. Theoretically predicted behavior and strength of the spandrel members and slab-beam systems are found to be in good agreement with those based on the laboratory tests. The study shows that CFRP retrofitting results in a significant to a dramatic increase in the bending strength of L-shaped spandrel members. The use of CFRP retrofitting is also shown to increase the torsional strength of such members by up to fifty percent.

Copyright, 2017, by Muhammad Fahim, All Rights Reserved.

To my parents; Khan Jee and Baibay.

ACKNOWLEDGEMENTS

الحمد لله

I would like to express my deepest appreciation and sincere gratitude to my research adviser and committee chair, Dr. Zia Razzaq, Professor, Department of Civil and Environmental Engineering, ODU, for his continuous guidance, encouragement, and support throughout my studies at Old Dominion University. I would also like to thank all my committee members for their valuable guidance throughout the work.

I am extremely thankful to Kevin Colvin, Tom Galloway, and the rest of the staff at the Engineering Model Shop at Old Dominion University for their help in preparing the test specimens and setups.

I would also like to thank many of my friends who contributed to the completion of this work. Special thanks are due to Irfan Shaukat, Mohammad Tayyem, Tasawar Baig, Wajid Khan, Herish Hussain, Mamaduo Konate, Ali Alousi, Yasser Al Zannan, Mohammad Imran, Farooq Chughtai, and Mohammad Faraz Akhtar for their help in the preparation of the concrete specimens and during the experiments.

Finally, I would like to thank my family, especially my parents, whose love and prayers are the greatest driving force in my life.

Muhammad Fahim

TABLE OF CONTENTS

LIST OF TABLES	viii
LIST OF FIGURES	ix
1. INTRODUCTION	1
1.1 Introduction.....	1
1.2 Literature Review.....	2
1.3 Problem Definition.....	5
1.4 Objectives and Scope.....	10
1.5 Assumptions and Conditions	11
2. EXPERIMENTAL STUDY.....	12
2.1 Introduction.....	12
2.2 Material Properties.....	12
2.3 Test Specimens	19
2.4 Specimen Preparation	39
2.5 Test Setup.....	40
2.6 Test Procedures.....	54
2.7 Test Results of Isolated Members.....	55
2.8 Slab Specimens Test Results	89
2.9 Comparison and Discussion.....	101
3. THEORETICAL ANALYSIS	103
3.1 Introduction.....	103
3.2 Bending Strength Analysis	103
3.3 Nonlinear Moment-Curvature Relations.....	111
3.4 Retrofitting Schemes for L-shaped section under Unsymmetrical Bending	125

3.5 Member Analysis under Unsymmetrical Bending.....	129
3.6 Cracking Torsional Strength.....	131
3.7 Ultimate Torsional Strength.....	133
3.8 Flexural-Torsional Interaction Relations	134
3.9 Torque versus Angle of Twist Relations	135
3.10 Ultimate Load of Slab-beam Systems.....	142
4. EXPERIMENTS VERSUS THEORY.....	145
4.1 Introduction.....	145
4.2 Moment-deflection Relations.....	145
4.3 Cracking Torsional Strength.....	152
4.4 Ultimate Torsional Strength.....	154
4.5 M-T Interaction for ultimate torque.....	155
4.6 Torque versus Angle of Twist Relations	162
4.7 Ultimate Load of Slab-beam Specimen	166
5. CONCLUSIONS AND FUTURE RESEARCH.....	167
5.1 Conclusions.....	167
5.2 Future Research	168
REFERENCES	169
APPENDICES	172
A. ACI CODE PROVISIONS FOR TORSION	172
B. ULTIMATE BENDING STRENGTH PROGRAM USING PATTERNS	176
C. MOMENT-CURVATURE PROGRAM USING TANGENT STIFFNESS METHOD.....	183
D. MOMENT-DEFLECTION PROGRAM USING PLFD	190
VITA	191

LIST OF TABLES

Table	Page
1. Summary of concrete cylinder test results	14
2. Reinforcement details of isolated members	20
3. Reinforcement details of slabs with spandrel members.....	21
4. Summary of test results for spandrel members.....	102
5. Results of uncracked section analysis.....	106
6. Results of ultimate bending strength analysis.....	111
7. Summary of results of moment-curvature analysis	125
8. Maximum bending capacity for a given number of CFRP strips	126
9. Maximum bending capacity for a given number of CFRP strips	127
10. Maximum bending capacity for a given number of CFRP strips	128
11. Torque at cracking under pure torsion	152
12. Cracking torsional strength under combined bending and torsion	153
13. Peak torque under pure torsion	154
14. Ultimate torsional strength under combined bending and torsion.....	161
15. Peak load of SL specimens	166

LIST OF FIGURES

Figure	Page
1. Spandrel member with applied loads	7
2. Schematic of specimen and its cross section	8
3. Slab-beam specimen with one point load	9
4. Slab-beam specimen with two point loads.....	9
5. (a) Concrete test cylinder with strain gage (b) Compression apparatus	13
6. Stress-strain relationship of concrete	14
7. Typical rebar test setup	15
8. Stress strain relationship for #2 steel rebars	16
9. Stress strain relationship of #3 rebars	17
10. Stress strain relationship of CFRP strips	18
11. Two components of the epoxy.....	19
12. Cross section of SS01	22
13. Long section of SS01	22
14. Cross section of SS02	23
15. Long section of SS02.....	23
16. Cross section of SS03	24
17. Long section of SS03	24
18. Cross section of SM04.....	25
19. Long section of SM04.....	26
20. Cross section of SM05-SM07.....	26
21. Long section of SM05-SM07	27
22. Cross section of SM08-SM10.....	28
23. Long section of SM08-SM10	28
24. Cross section of SM11-SM13.....	29
25. Long section of SM11-SM13	29
26. Cross section of SM14 having two external CFRP strips.....	30
27. Long section of SM14.....	30
28. Cross section of SM15.....	31
29. Long section of SM15.....	31

Figure	Page
30. Cross section of SM16.....	32
31. Long section of SM16.....	32
32. Cross section of SM17-SM19 with internal CFRP strips.....	33
33. Long section of SM17-SM19	33
34. Plan of SL01 showing slab reinforcement.....	35
35. Slab cross section of SL01	35
36. Cross section of spandrel member in SL01	36
37. Long section of spandrel member in SL01	36
38. Plan of SL02 and SL03 showing slab reinforcement.....	37
39. Slab cross section of SL02 and SL03	38
40. Cross section of spandrel members in SL02 and SL03	38
41. Long section of spandrel members in SL02 and SL03	39
42. Formwork with reinforcement for spandrel members	39
43. Reinforcement skeleton in formwork for slab specimens.....	40
44. Bending test setup for spandrel members	42
45. Schematic of portion of apparatus for applying bending [28].....	43
46. Lower end gimbal [28].....	44
47. Schematic of moment arm attached to upper gimbal [28].....	44
48. Torsion test setup for spandrel members	46
49. Schematic of a portion of the apparatus for applying torque [28].....	47
50. Steel box for connecting and holding specimen	48
51. Schematic of test setup for slab with spandrel members	49
52. Test setup for SL01	50
53. Test setup for SL02.....	50
54. Test setup for SL03	51
55. Dial gages for measuring displacements.....	52
56. Dial gages to calculate rotation of spandrel members	53
57. Location of strain gages on spandrel members.....	54
58. Moment-deflection relation for SS01	56
59. Torque versus angle of twist relation for SS01.....	57

Figure	Page
60. Final crack pattern of SS01	57
61. Moment-deflection relation for SS02	58
62. Torque versus angle of twist relation for SS02.....	59
63. Final crack pattern of SS02.....	59
64. Moment-deflection relation for SS03	60
65. Torque-angle of twist relation for SS03.....	61
66. Final crack pattern for SS03	61
67. Torque versus angle of twist relation for SM04	62
68. Final crack pattern for SM04	63
69. Torque versus angle of twist relation for SM05	64
70. Final crack pattern for SM05	64
71. Final crack pattern of SM06	65
72. Moment-deflection relation for SM07	66
73. Torque versus angle of twist relation for SM07	67
74. Final crack pattern of SM07	67
75. Torque versus angle of twist relation for SM08	68
76. Final crack pattern of SM08	69
77. Moment-deflection relation for SM09	70
78. Final crack pattern of SM09	70
79. Moment-deflection relation for SM10	71
80. Torque versus angle of twist relation for SM10	72
81. Final crack pattern of SM10	72
82. Torque versus angle of twist relation for SM11	73
83. Final crack pattern of SM11	74
84. Moment-deflection relation for SM12.....	75
85. Torque versus angle of twist relation for SM12	75
86. Final crack pattern of SM12	76
87. Torque versus angle of twist relation for SM13	77
88. Moment-deflection relation for SM13	77
89. Final crack pattern of SM13	78

Figure	Page
90. Torque versus angle of twist relation for SM14	79
91. Final crack pattern of SM14	79
92. Moment-deflection relation for SM15	80
93. Torque versus angle of twist relation for SM15	81
94. Final crack pattern of SM15	81
95. Moment-deflection relation for SM16	82
96. Torque versus angle of twist relation for SM16	83
97. Final crack pattern of SM16	83
98. Torque versus angle of twist relation for SM17	84
99. Final crack pattern of SM17	85
100. Moment-deflection relation for SM18	86
101. Final crack pattern for SM18	86
102. Moment-deflection relation for SM19	87
103. Torque versus angle of twist relation for SM19	88
104. Final crack pattern of SM19	88
105. Load-deflection relation for slab of SL01	89
106. Load-deflection relation for spandrel members of SL01	90
107. Cracks at the bottom surface of slab in SL01	91
108. Cracks in spandrel member of SL01 at a load of 25.72 kip.....	92
109. Bottom view of SL01 after test.....	93
110. Load-deflection relation for slab of SL02.....	94
111. Load-deflection relation for spandrel members of SL02.....	95
112. Bottom view of SL02 after test.....	96
113. Final cracking pattern in typical spandrel member of SL02.....	96
114. Load-deflection for slab of SL03	97
115. Load-deflection relation of SMB in SL03	98
116. Load-deflection relation of SMD in SL03	99
117. Bottom view of SL03 after test.....	100
118. Final crack pattern of SMB in SL03	100
119. Final crack pattern of SMD in SL03.....	101

Figure	Page
120. Typical cross section for transformed area method	103
121. Pattern 1 for ultimate strength analysis.....	107
122. Pattern 2 for ultimate strength analysis.....	108
123. Member segment schematic under biaxial bending.....	112
124. Partitioning of the cross section.....	113
125. Moment-curvature relation of SS01.....	120
126. Moment-curvature relation of SS02 and SS03	120
127. Moment-curvature relation of SM04	121
128. Moment-curvature relation of SM05-SM07	121
129. Moment-curvature relation of SM08-SM10	122
130. Moment-curvature relation of SM11-SM13	122
131. Moment-curvature relation of SM14	123
132. Moment-curvature relation of SM15	123
133. Moment-curvature relation of SM16	124
134. Moment-curvature relation of SM17-SM19	124
135. Ultimate bending moment with given CFRP area for SM05.....	129
136. Bending moment about x-axis and corresponding deflections	130
137. Equilibrium of cracked model [36].....	136
138. An element in the shear flow zone [37].....	137
139. Section subjected to torsion [37].....	138
140. Deformation of top wall [37]	139
141. Strain and stress distribution in concrete struts.....	139
142. Solution algorithm flowchart for torsional analysis using CFT.....	141
143. Yield line pattern for rectangular slab with one point load [38].....	143
144. Yield line pattern for rectangular slab with two point loads [38].....	144
145. Moment-deflection relation of SS01	146
146. Moment-deflection relation of SS02.....	146
147. Moment-deflection relation of SS03.....	147
148. Moment-deflection relation of SM07	147
149. Moment-deflection relation of SM09	148

Figure	Page
150. Moment-deflection relation of SM10	148
151. Moment-deflection relation of SM12	149
152. Moment-deflection relation of SM13	149
153. Moment-deflection relation of SM15	150
154. Moment-deflection relation of SM16	150
155. Moment-deflection relation of SM18	151
156. Moment-deflection relation of SM19	151
157. M-T interaction for SS01	155
158. M-T interaction for SS02	156
159. M-T interaction for SS03	156
160. M-T interaction for SM07	157
161. M-T interaction for SM10	157
162. M-T interaction for SM12	158
163. M-T interaction for SM13	158
164. M-T interaction for SM15	159
165. M-T interaction for SM16	159
166. M-T interaction for SM17	160
167. Torque versus angle of twist for SS03	162
168. Torque versus angle of twist for SM05	163
169. Torque versus angle of twist for SM07	163
170. Torque versus angle of twist for SM08	164
171. Torque versus angle of twist for SM11	164
172. Torque versus angle of twist for SM14	165
173. Torque versus angle of twist for SM16	165

1. INTRODUCTION

1.1 Introduction

Spandrel members are often used in reinforced concrete buildings such as the outermost beam-like members integrated with reinforced concrete slabs. These members are generally subjected to unsymmetrical bending and torsion. The cross section of the spandrel member is L-shaped due to the contribution of the connecting slab approximated as a flange. The available methods for analyzing and designing spandrel members are flawed in that they make unjustifiable approximations such as assuming a horizontal neutral axis under unsymmetrical bending moments subsequently combined with applied torsional loading effects.

The strength and behavior of reinforced concrete rectangular sections subjected to combined bending and torsional moments have been extensively studied in the past both theoretically and experimentally. This includes development of ultimate strength interaction relations between bending and torsion. However, the methods developed for predicting the response of spandrel members of L-shaped cross sections subjected to unsymmetrical bending, torsion, or combined unsymmetrical bending and torsion have not adequately been developed previously.

In addition to a need for the development of theoretical behavior and strength prediction models for spandrel members, it is also becoming increasingly important to devise retrofitting procedures for enhancing their flexural-torsional capacity. One particular retrofitting technique utilizes high strength Carbon Fiber Reinforced Polymer (CFRP) strips bonded externally to steel-reinforced concrete members. The use of CFRP retrofitting methods for reinforced concrete members with rectangular cross sections has been studied in the past. However, such a methodology has not been developed for spandrel members of L-shaped cross sections with unsymmetrical bending, torsion, or combined unsymmetrical bending and torsion.

The primary goal of this dissertation is to present the outcome of a theoretical and experimental study of isolated spandrel members subjected to unsymmetrical bending, torsion, and combined unsymmetrical bending and torsion both with and without CFRP retrofitting. The theoretical behavior and strength prediction models account for material nonlinearities. The experimental study is conducted on scaled-down spandrel members using a bending-torsion testing apparatus.

In addition to the member level study, three steel-reinforced slabs with four surrounding spandrel members are also tested without CFRP and their load carrying capacities compared to those predicted theoretically. Finally, the effectiveness of CFRP retrofitting for a typical spandrel member as an integral part of a slab-beam system is demonstrated through use of a flexural-torsional interaction expression presented in this dissertation that accounts for CFRP retrofitting.

1.2 Literature Review

Chen and Shoraka [1] used tangent stiffness method to develop moment-thrust-curvature relations for rectangular reinforced concrete sections. They studied the influence of concrete strength, reinforcement strength, and percentage of reinforcement on the shape of the curves.

Historically, the very first equation to determine the strength of a homogenous elastic section under torsion was developed by Coulomb in 1784 while conducting experiments on electric charges [2]. However, his equation was completely empirical without any theoretical basis. Navier was the first person to develop a torsion theory for linear elastic and homogenous materials with circular cross sections in 1826 [3]. St. Venant [2] extended the theory to rectangular sections and accounted for warping deformations in 1856. He used a semi inverse method to solve all fifteen differential and algebraic equations in theory of elasticity developed by Cauchy [2]. According to St. Venant's theory, the maximum shear stress occurs on the outside face of a rectangular section at midpoint of each long side.

In 1896, Bredt [2] derived a formula for constant shear flow in thin-walled tubular sections subject to torsion. In 1903, Prandtl [2] discovered membrane analogy by observing that both the stress function in torsion problem and the deflection of a membrane under uniform loading are governed by Laplace's harmonic differential equation and must satisfy the same boundary conditions. This analogy has been used to determine torsional properties of complicated cross sections.

Bach [2] proposed a simplification of St. Venant's theory for thin walled open sections in 1911. Based on the assumption that the angle of twist is the same for all rectangular components of a flanged section, the strength of the entire section is the algebraic sum of rectangular components. In 1923, Nadai [2] extended the membrane analogy to plastic materials which is called Nadai's sand-heap analogy.

Both elastic and plastic theories have been used to predict the torsional capacity of plain concrete members by assuming a failure criteria that a plain concrete member fails when the maximum principal tensile stress reaches the tensile strength of concrete [2]. Since maximum tensile stress equals maximum shear stress under pure torsion, it can be substituted in equations for torsion to obtain torsional strength. Hsu [4] developed an equation for the torsional strength of plain concrete members by assuming a bending-type failure and utilizing an empirical relation for the modulus of rupture as a measure of tensile strength of concrete. He also derived an equation to find angle of twist at failure which is independent of material properties of concrete.

The first theory of torsion for reinforced concrete members was presented by Rausch [2] in 1929 known as “Rausch Space Truss Analogy”. Rausch proposed that a reinforced concrete member under torsion can be modelled as a space truss that consists of 45° concrete struts in compression and longitudinal and transverse rebars in tension. Cowan [5] introduced an efficiency coefficient by considering non-uniform stresses in reinforcement bars and considered the contribution of concrete. Hsu[6] concluded that the cracking torque of a reinforced concrete member is 1.0-1.3 times the failure torque of the corresponding plain concrete member. Hsu [7] presented skew bending theory in 1968.

Nadai [8] sand-heap analogy can be used to determine the torsional strength of flanged concrete sections. Hsu [4] attempted to develop equation for the torsional strength of flanged cross sections using the skew bending theory but concluded that the mathematical complexity has rendered it useless in practice.

The most important factors affecting the behavior of reinforced concrete spandrel members subjected to combined bending and torsion are T/M ratio, amount and distribution of transverse and longitudinal reinforcement, cross section shape, and concrete strength [9].

The bending-torsion interaction for members without transverse reinforcement has been experimentally studied by various researchers. For rectangular sections, McMullen and Woodhead [10] suggested a linear interaction, Kemp et al. [11] proposed a trilinear interaction, and Zia [12] observed that a circular interaction curve serves as a lower bound for most experimental results. Hsu [13] recommended a trilinear interaction for members without stirrups.

McMullen and Warwaruk [14] developed the normalized bending-torsion interaction curves for symmetrically and unsymmetrically reinforced sections. For unsymmetrically reinforced beams,

the torsional strength increases in the presence of a small flexural moment. With the addition of a bending moment equal to 40 percent of the pure flexure strength, McMullen and Warwaruk [14] observed an increase of up to 30 percent in the torsional strength and Onsongo [15] observed a 25 percent increase. In the case of pure torsion, the additional bottom reinforcement doesn't increase the ultimate strength because the top weaker reinforcement is critical. The compression introduced by flexure in the top reinforcement increases its resistance to torsional shear stresses [9]. Onsongo [15] observed only a 6 percent increase in torsional strength with the addition of flexural moment in over-reinforced beam. Onsongo [15] also developed the interaction for two series of unsymmetrically reinforced sections with different ratios of compression to tension longitudinal reinforcement yield force. The torsion predominant member is subjected to overall reverse curvature because the weaker top reinforcement elongates more than the bottom reinforcement [9].

Haug et al. [16] introduced a functional interaction formula for a symmetrically reinforced concrete section under combined axial, bending, shear, and torsion. They used experimental data available in literature to find the coefficients through calibration. They also deduced an interaction between less than four actions as special cases. They only considered one moment and one shear.

For flanged sections, Victor and Ferguson [17] proposed a trilinear interaction for L-sections and square interaction for T-sections. Lim and Mirza [18] also suggested a square interaction for T-sections. Zararis and Penelis [19] observed 18 percent increase in torsional strength with the addition of flexural moment for unsymmetrically reinforced T-sections.

For members with only longitudinal steel reinforcement, the torque twist relationship is very close to that of plain concrete before cracking. After cracking, the member may collapse suddenly if the reinforcement ratio is small. The ultimate strength may exceed cracking torque if the member is heavily reinforced but the increase is usually less than 15 percent. Therefore, the relations developed for plain concrete members can be used to find the strength of concrete sections with only longitudinal reinforcement [2].

Hsu [6] found that about 1% of total steel, the ultimate strength of the beam is almost equal to the cracking torque and the beam fails in a ductile fashion with the torque-twist curve showing a long horizontal plateau. McMullen and Warwaruk [14] experimentally developed torque-twist

curves for 6 x 12 in symmetrically reinforced beams at $T/M = 0$ to 0.25. They observed that the presence of bending moment significantly reduced the torsional strength, ductility, and post-cracking stiffness. The cracking torque is a mild function of the total steel reinforcement.

The post cracking torsional stiffness of unsymmetrically reinforced members increases significantly with the addition of a small bending moment [15]. The torsional ductility reduces in the presence of flexural moment for both symmetrically and unsymmetrically reinforced beams [14, 15]. The torque-twist diagrams show that the ultimate torsional strength was reached at a smaller value of twist in the presence of flexural moment for both symmetrically and unsymmetrically reinforced beams. Onsongo [15] developed the torque-twist curves for unsymmetrically under-reinforced hollow sections at various T/M ratios.

American Concrete Institute (ACI) established Committee 438 on torsion in 1958. In 1977, Committee 426 was merged with 438 and Committee 445 (shear and torsion) was formed. Torsion provisions were first added to the 1971 code which were applicable to only nonprestressed rectangular sections. Provisions for torsion limit design of spandrel members were added to the 1977 code [20]. A new procedure was adopted in the 1995 code [21].

To the best of the author's knowledge, the study of spandrel members including CFRP retrofitting and its application to slab-beam systems has not been published in the past.

1.3 Problem Definition

The primary problem addressed in this dissertation is to develop theoretical behavior and strength prediction models for spandrel members subjected to unsymmetrical bending, torsion, and combined unsymmetrical bending and torsion both with and without CFRP retrofitting. The experimental part of the problem is to conduct a series of experiments on isolated spandrel members of square and L-shaped cross sections and on spandrel members as part of a slab-beam system and compare the results with the theoretical predictions.

A typical isolated spandrel member with CFRP retrofitting is shown in Figure 1. A small axial compressive force, P , is applied in the beginning of each experiment. A bending moment, M_x , is applied at the top end of the specimen which varies linearly to a zero value at the bottom end. A torsional moment T is applied at the bottom end of the member which remains uniform along the length of the specimen. A schematic of an isolated spandrel member is shown in Figure 2 where

L_t is the total length between end gimbals and L is the clear length of specimen. A detailed description of the test setup is given in Chapter 2.

The spandrel members in the slab-beam specimens are subjected to bending and torsional moments developed by transverse point load(s) applied on the surface of the slabs. The first slab-beam specimen was subjected to one concentrated load applied at the middle of the slab as shown in Figure 3. The remaining two specimens were subjected to two point loads, as shown in Figure 4.

Another problem addressed in this dissertation is to determine the effectiveness of a CFRP retrofitting scheme for improving flexural-torsional capacity of L-shaped spandrel members. The CFRP retrofitting was used for both undamaged and pre-damaged specimens.

The theoretical challenge in this research study is to develop nonlinear behavior and strength models for unsymmetrical bending and torsion to predict the observed experimental behavior. These include development of expressions for cracking and ultimate bending capacity by assuming various failure patterns with inclined neutral axis and moment-curvature relations for unsymmetrical bending using tangent stiffness method. The torsion part of the problem includes the development of an iterative algorithm based on Modified Compression Field Theory (MCFT) for predicting complete torque-twist behavior of members. Finally, the problem of flexural-torsional interaction is addressed by assuming a parabolic interaction relation.

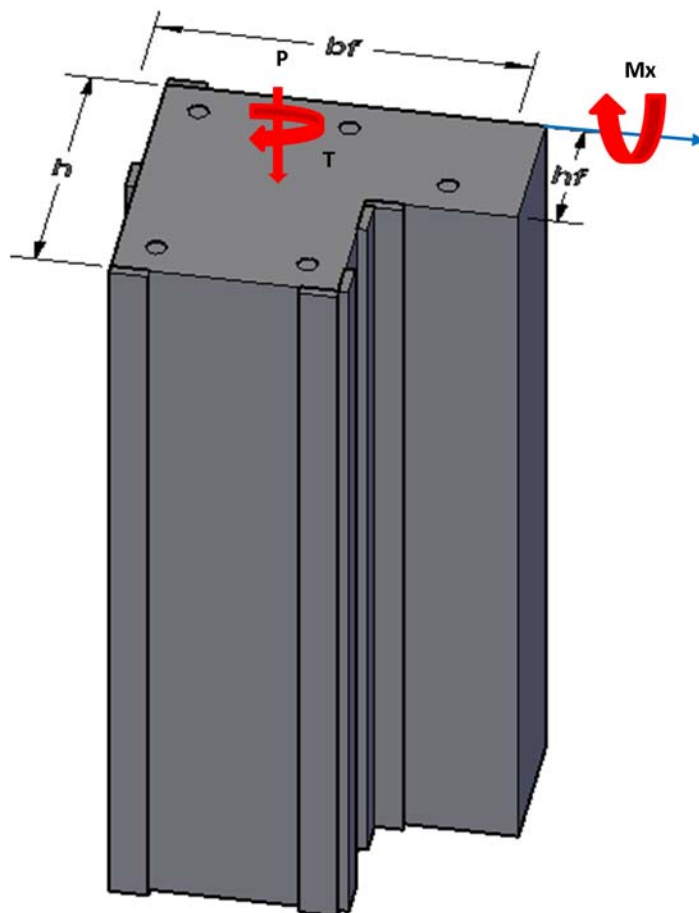


Figure 1. Spandrel member with applied loads

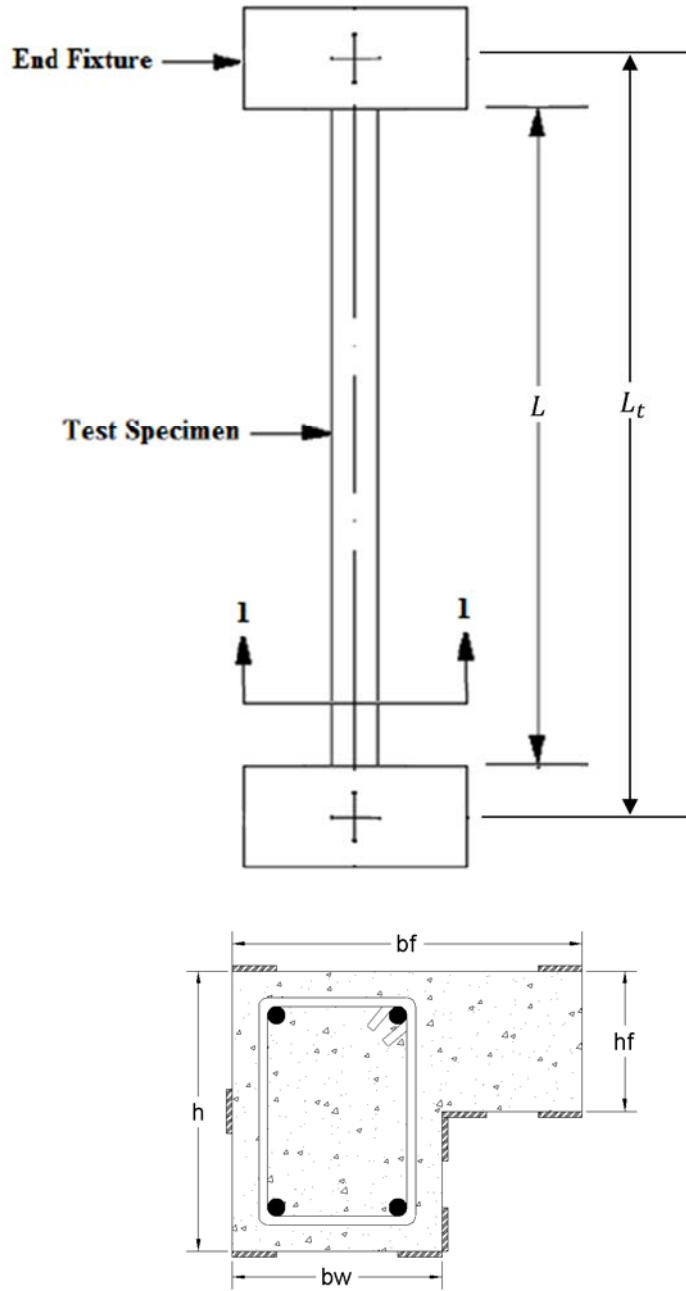


Figure 2. Schematic of specimen and its cross section

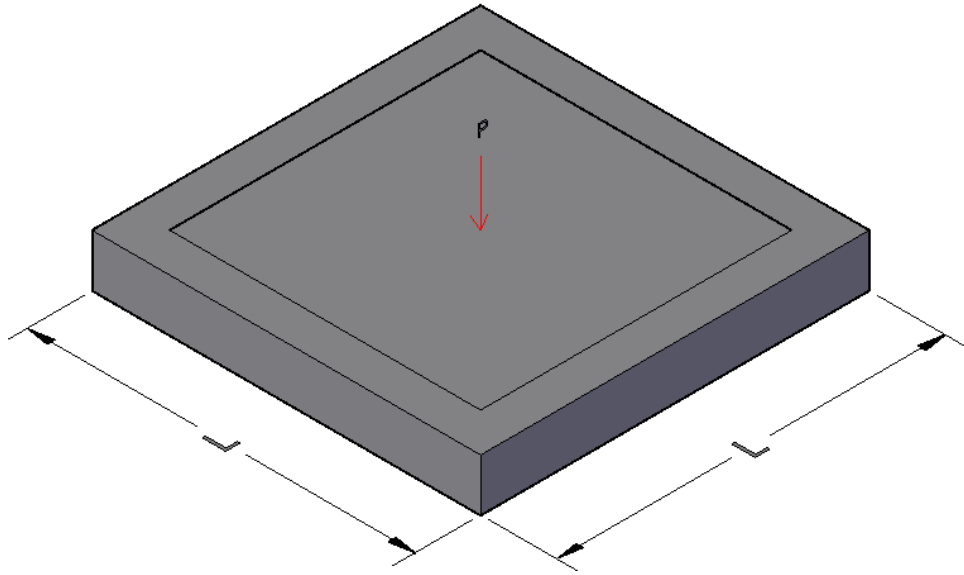


Figure 3. Slab-beam specimen with one point load

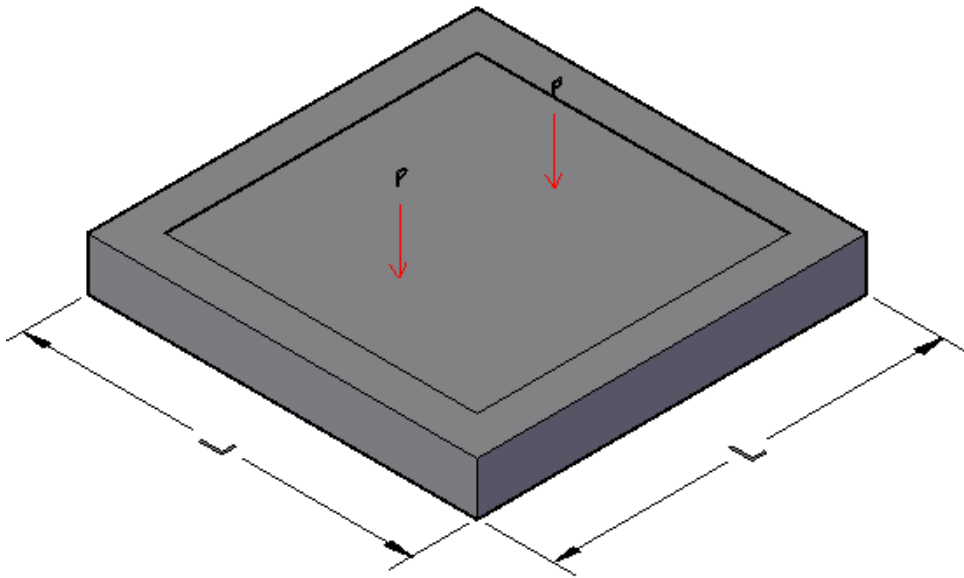


Figure 4. Slab-beam specimen with two point loads

1.4 Objectives and Scope

This research presents the outcome of experimental and theoretical investigations of reinforced concrete spandrel members under the action of separate and combined unsymmetrical bending and torsion with and without CFRP retrofitting. The main objectives of this study are as follows:

1. Conduct a series of tests on isolated RC spandrel members under separate and combined unsymmetrical bending and torsion to calculate their ultimate capacity, cracking patterns, and load-deformation relations.
2. Investigate the behavior of spandrel members as part of a slab-beam system subjected to combined bending and torsion transferred from the slab under the application of point load(s).
3. Develop cracking and ultimate bending capacity expressions for L-shaped reinforced concrete members.
4. Develop moment-curvature relations for unsymmetrical bending of reinforced concrete square and L-shaped cross sections.
5. Develop an iterative algorithm for L-shaped cross sections incorporating Modified Compression Field Theory (MCFT) to predict their torsional behavior.
6. Develop an effective retrofitting scheme for spandrel members of L-shaped cross sections to enhance their bending and torsion capacities.
7. Verify the parabolic interaction relation of bending and torsion for L-shaped RC members with and without CFRP retrofitting.
8. Develop a relation linking the bending and torsion interaction of isolated spandrel members to the spandrel members in slab-beam specimens.

Three isolated members of square cross section, sixteen isolated spandrel members, and three slab-beam specimens are tested in this research study. The concrete used in the fabrication of these specimens has a specified 28-day ultimate compressive strength of 5,000 psi. Grade 50, #2 steel rebars are used as both longitudinal and transverse reinforcements in the isolated spandrel members and as shear reinforcement in the spandrel members of slab-beam specimens. Grade 60, #3 rebars are used as slab reinforcement and as longitudinal reinforcement in the spandrel members of slab-beam specimens. The CFRP strips used for retrofitting purposes have a specified tensile strength of 250 ksi.

1.5 Assumptions and Conditions

The following and assumptions and conditions have also been made:

1. Plane sections before bending remain plane after bending.
2. Small deflection theory is applicable.
3. Shear deformation is ignored in the analysis of spandrel members.
4. Perfect bond between reinforcing bars and surrounding concrete exists.
5. Effects of shrinkage and creep are ignored.
6. A monotonically increasing load is considered in the analysis.
7. No material unloading is considered.

2. EXPERIMENTAL STUDY

2.1 Introduction

This chapter presents the experimental part of the research conducted. Three isolated members of a square cross section were first tested to gain a basic understanding of their behavior under combined bending and torsion. A total of sixteen isolated spandrel members of L-shaped cross section, both non-retrofitted and CFRP-retrofitted, were then tested to collapse condition under gradually increasing quasi-static unsymmetrical bending, uniform torsion, and combined unsymmetrical bending and torsion. Lastly, three slab specimens with monolithic spandrel members along all four slab edges were tested.

2.2 Material Properties

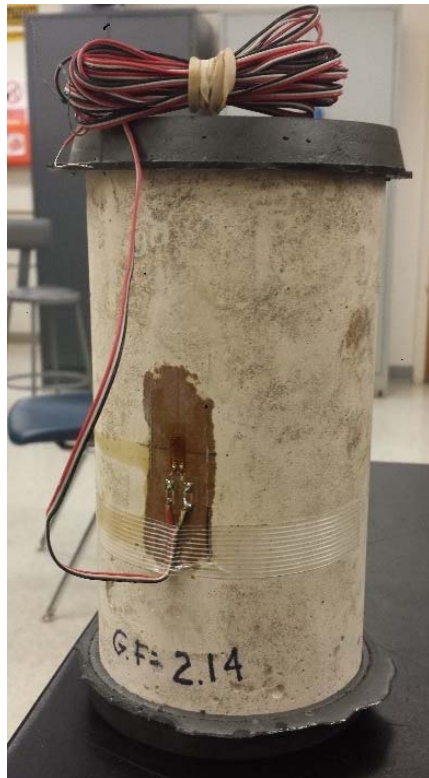
The specimens tested in the experimental part of the study were fabricated using three types of materials, namely concrete, steel reinforcing rebars, and high strength Carbon Fiber Reinforced Polymer (CFRP) strips. The mechanical properties of these materials were found by conducting appropriate tests following ASTM standards. The details of these tests and the results are presented in this section. These properties are utilized in the analyses presented in Chapter 3.

2.2.1 Concrete

Companion test cylinders having 4 in. diameter and 8 in. height were cast to determine actual compressive strength of concrete for each specimen. A minimum of 28-day curing period was used for all cylinders. Figure 5(a) shows one such cylinder mounted with a longitudinal strain gage. A P3 strain indicator box, made by Vishay Micromeritics, is used to record the values of strain. Figure 5(b) shows the compression testing apparatus made by Tinius Olsen used for cylinder tests. Figure 6 shows a couple of experimental stress-strain relations along with a second degree curve approximation [22]:

$$f_c = f'_c \left[\frac{2\epsilon}{\epsilon_0} - \left(\frac{\epsilon}{\epsilon_0} \right)^2 \right] \quad (1)$$

where f'_c represents the ultimate compressive strength of concrete, ϵ_0 is the strain corresponding to f'_c , and f_c is concrete stress at any strain level ϵ . Table 1 shows the average cylinder values of ultimate and failure strains and stresses for each specimen where f'_u and ϵ_u represent stress and strain at failure, respectively.



(a)



(b)

Figure 5. (a) Concrete test cylinder with strain gage (b) Compression apparatus

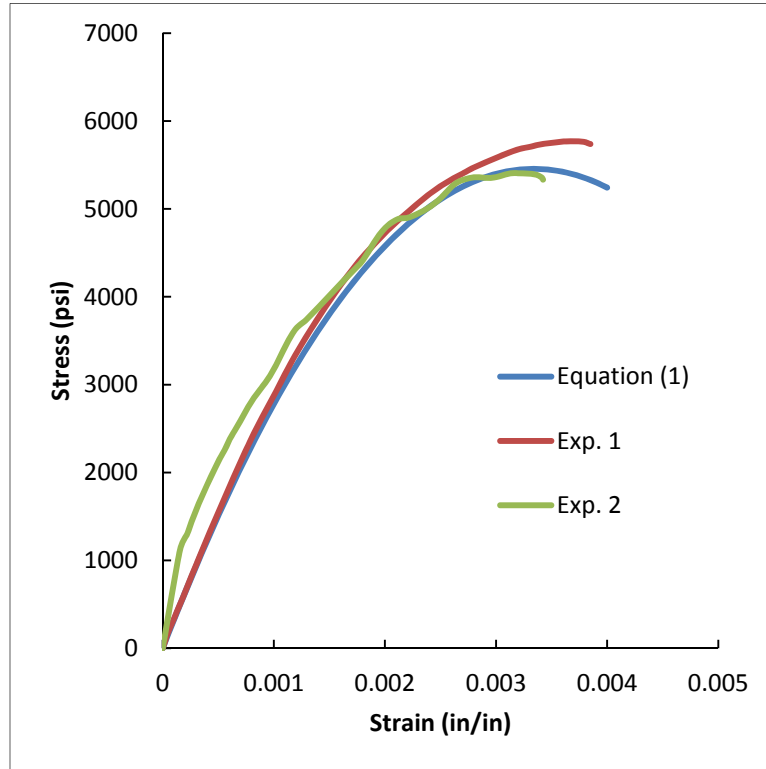


Figure 6. Stress-strain relationship of concrete

Table 1. Summary of concrete cylinder test results

Batch No.	Specimens	f'_c (psi)	ϵ_0 (in/in)	f'_u (psi)	ϵ_u (in/in)
1	SL01	3697	-	-	-
2	SL02	5149	0.00267	4997	0.00284
3	SL03	4667	0.00294	4379	0.00350
4	SS01—SS03	5365	0.00389	5268	0.00399
5	SM04—SM07	5765	0.00362	5516	0.00398
6	SM08—SM10	5849	0.00332	5588	0.00353
7	SM11—SM13	6416	0.00368	6030	0.00406
8	SM14—SM16	5765	0.00362	5516	0.00398
9	SM17—SM19	5392	0.00287	5201	0.00323

2.2.2 Steel Reinforcement

There were two types of reinforcing bars used in this study; Grade 60, #3 rebar (3/8 in. diameter) and Grade 50, #2 rebar (2/8 in. diameter). The #3 rebar was used in the slab specimens as slab reinforcement as well as longitudinal rebar in the spandrel members. The #2 rebar was used in the isolated spandrel members as both longitudinal and transverse reinforcement and as transverse reinforcement in spandrel members of slab specimens. Figure 7 shows tensile test setup for a typical rebar. The test specimens were mounted with extensometer to record strain values during tests.



Figure 7. Typical rebar test setup

Tension test results of #2 and #3 rebar are shown in Figure 8 and Figure 9, respectively. The stress-strain relationship was found to be initially a straight line with a constant slope. This initial straight part is followed by an almost horizontal part, as shown in Figure 8 and Figure 9. For #2 rebar, the average tensile yield strength was found to be 49.5 ksi. The modulus of elasticity (E)

for #2 rebars was found to be 28700 ksi. Similarly for #3 rebars, the average tensile strength was determined to be 63.5 ksi and the modulus of elasticity for #3 rebars was found to be 29420 ksi.

The stress-strain relationship for steel rebars is idealized by a bilinear approximation in the numerical analysis given in Chapter 3. The bilinear approximation is represented mathematically as:

$$f_s = E \varepsilon_s \quad \text{when } |\varepsilon_s| \leq \varepsilon_y \quad (2)$$

$$f_s = f_y \quad \text{when } |\varepsilon_s| > \varepsilon_y \quad (3)$$

where f_y represents the yield strength of steel rebars and ε_y is the corresponding yield strain.

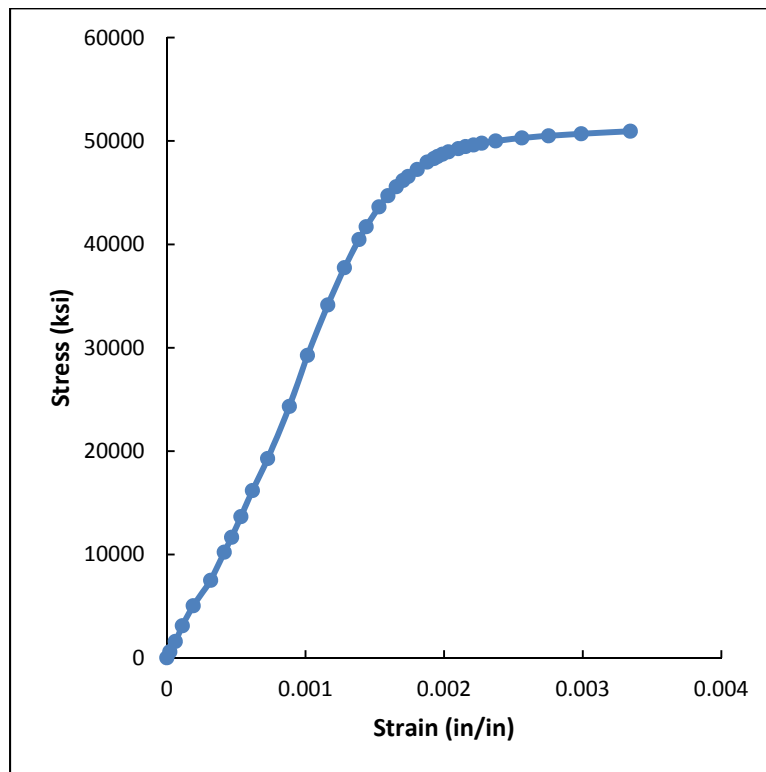


Figure 8. Stress strain relationship for #2 steel rebars

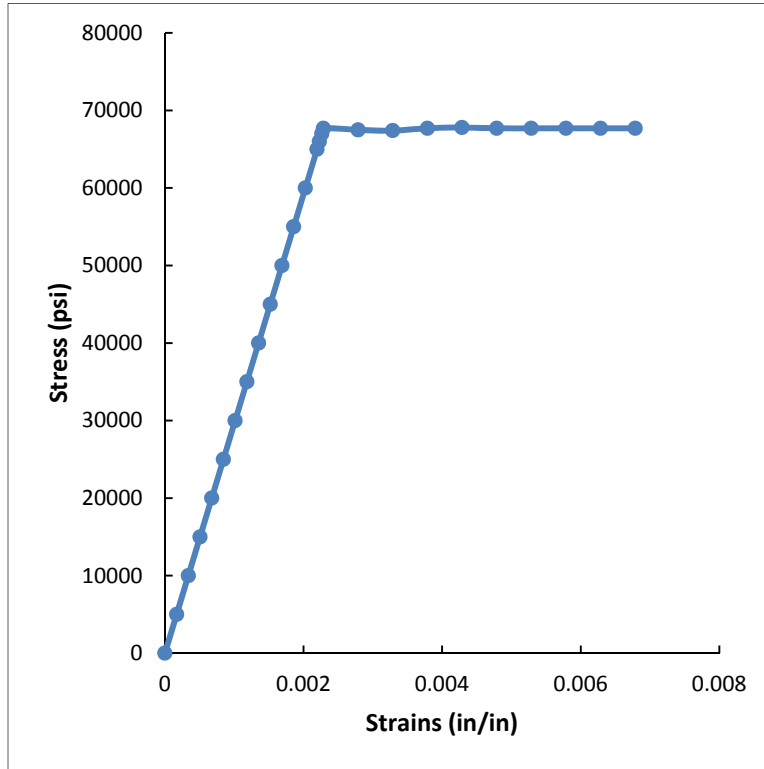


Figure 9. Stress strain relationship of #3 rebar

2.2.3 Carbon Fiber Reinforced Polymer (CFRP) Strips

Carbon Fiber Reinforced Polymer (CFRP) strips with commercial name “Aslan 500 6mm Tape” sold by Hughes Brothers is used for retrofitting purposes. The strips are 0.63 in. wide and 0.079 in. thick with a cross sectional area of 0.0498 in². These strips have been tested by Nakul [23] for tensile properties using ASTM D7205/D7205M-06. The tensile strength was found to be 255.6 ksi at an ultimate strain of 0.01325 in/in. The modulus of elasticity (E_f) was found to be 20×10^6 psi. The linear approximation of the stress-strain relationship is represented graphically in Figure 10 and mathematically as:

$$f_f = E_f \varepsilon_f \quad \text{when } |\varepsilon_f| \leq \varepsilon'_f \quad (4)$$

$$f_f = 0 \quad \text{when } |\varepsilon_f| > \varepsilon'_f \quad (5)$$

where f_f is the stress level at a strain ϵ_f and ϵ'_f represents the ultimate strain in CFRP strips. As indicated by the graph, the CFRP is less stiff than steel and has no ductility. The details about the number of CFRP strips used and their locations for each member are given in the subsequent sections.

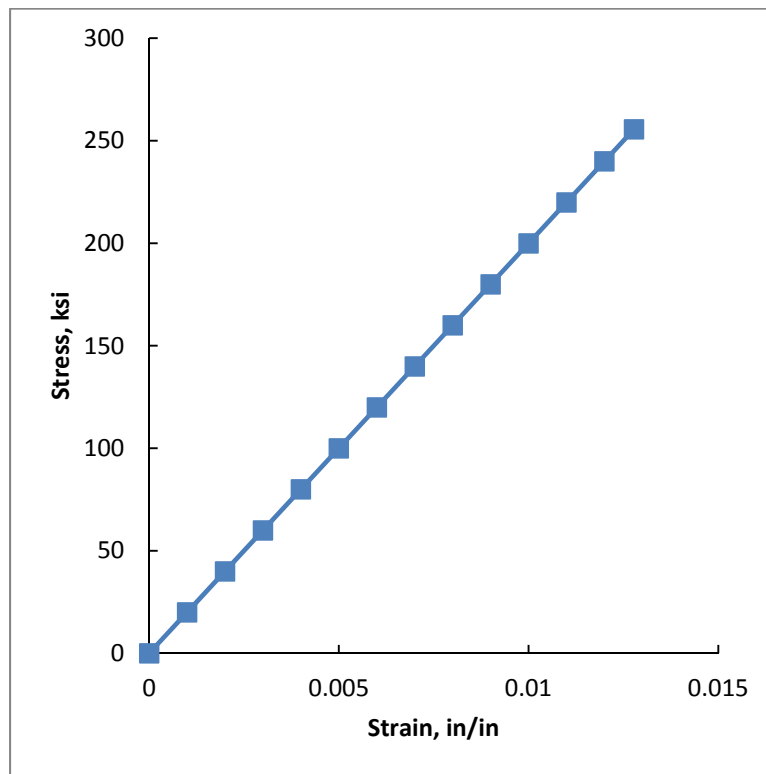


Figure 10. Stress strain relationship of CFRP strips

2.2.4 Sikadur 30 Epoxy Paste Adhesive

The CFRP strips are bonded externally with concrete members using Sikadur 30 epoxy paste. Sikadur 30 is a high modulus and high strength structural epoxy paste adhesive. It is a 2-component, hundred percent solids, and moisture-insensitive adhesive. It conforms to the current ASTM C-881 and AASHTO M-235 specifications. Figure 11 shows the two components which

were mixed in a 3:1 ratio as recommended. The paste should be used within seventy minutes of mixing the two components and the member should not be disturbed for a minimum of 24 hours. Sikadur 30 needs a seven days curing time at room temperature to gain its design strength.



Figure 11. Two components of the epoxy

2.3 Test Specimens

Table 2 presents the reinforcement details of square section members and L-shaped spandrel members tested in the laboratory. In this table, square section members are designated as Specimens SS01 through SS03 whereas L-shaped spandrel members are named as Specimens SM04 through SM19. The last column in Table 2 shows the type of loading applied on a given specimen and the loading sequence where applicable. The unsymmetric applied bending moment M_x and the torque T are shown in Figure 1. A detailed description of each specimen is given in the subsequent sections.

Table 2. Reinforcement details of isolated members

Specimen	No. of Rebars	Shear Reinforcement	No. of CFRP strips	Loading
SS01	-	-	-	M_x , T
SS02	4, # 2	-	-	M_x , T
SS03	4, # 2	#2 @ 5 in c/c	-	M_x , T
SM04	-	-	-	T
SM05	4, # 2	#2 @ 5 in c/c	-	T
SM06	4, # 2	#2 @ 5 in c/c	-	M_x
SM07	4, # 2	#2 @ 5 in c/c	-	M_x , T
SM08	5, # 2	#2 @ 5 in c/c	-	T
SM09	5, # 2	#2 @ 5 in c/c	-	M_x
SM10	5, # 2	#2 @ 5 in c/c	-	M_x , T
SM11	5, # 2	#2 @ 5 in c/c	-	T
SM12	5, # 2	#2 @ 5 in c/c	-	M_x , T
SM13	5, # 2	#2 @ 5 in c/c	-	T, M_x
SM14	4, # 2	#2 @ 5 in c/c	2	T
SM15	4, # 2	#2 @ 5 in c/c	6	M_x , T
SM16	4, # 2	#2 @ 5 in c/c	6	M_x , T
SM17	5, # 2	#2 @ 5 in c/c	4	T
SM18	5, # 2	#2 @ 5 in c/c	4	M_x , T
SM19	5, # 2	#2 @ 5 in c/c	4	M_x , T

In addition to the isolated members, three slab-beam specimens with monolithic spandrel members on all four edges were also tested. Table 3 shows reinforcement and loading details for the slab-beam specimens. All three slabs were isotropically reinforced for positive bending moment with no negative reinforcement. In the first slab (SL01), the spandrel members had only longitudinal tensile reinforcement with no compression rebars or shear stirrups. However, spandrel members of the remaining two slabs were reinforced with longitudinal and transverse rebars. The one- and two-point loading conditions indicated in the last column of Table 3 are schematically shown in Figure 3 and Figure 4. Further details are given in the subsequent sections.

Table 3. Reinforcement details of slabs with spandrel members

Specimen	Slab Reinforcement (Isotropic)	Spandrel Member Tension Rebars	Spandrel Member Compression Rebars	Spandrel Member Shear Reinforcement	Point Loading
SL01	#3 @ 3 in c/c	2, # 3	-	-	One point
SL02	#3 @ 4 in c/c	2, # 3	2, # 3	#2 @ 6 in c/c	Two point
SL03	#3 @ 4 in c/c	2, # 3	2, # 3	#2 @ 6 in c/c	Two point

2.3.1 Isolated Members of Square Cross Section

Three isolated members having square cross section were tested under the combined action of bending and torsional moments. All specimens were 28 in. long and had 5 in. x 5 in. cross section. The first specimen (SS01) was a plain concrete member without any steel reinforcement. This member served as a control specimen for square spandrel members. The cross sectional details are shown in Figure 12 and the longitudinal details are shown in Figure 13.

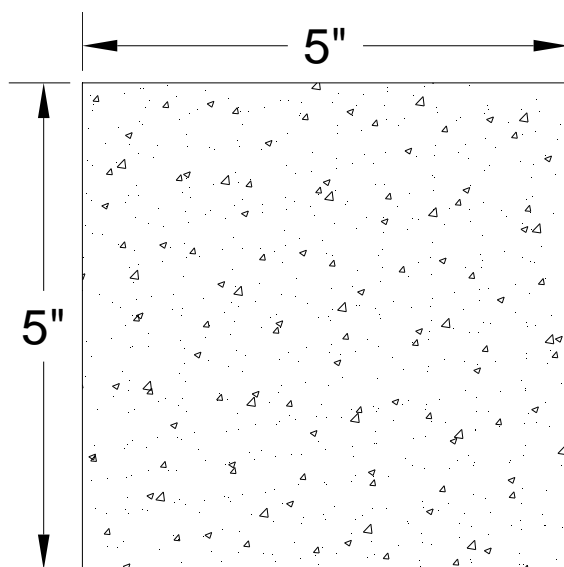


Figure 12. Cross section of SS01

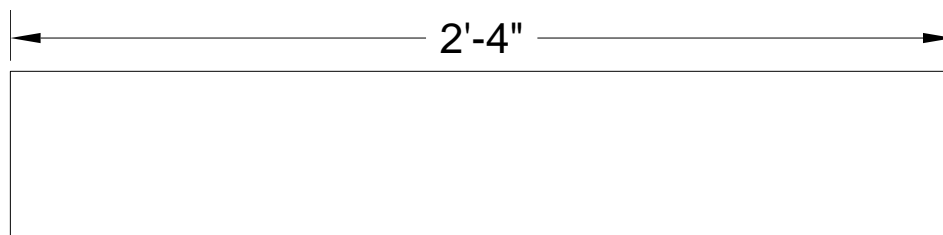


Figure 13. Long section of SS01.

The second specimen (SS02) had only longitudinal reinforcement without any transverse stirrups. The reinforcement consists of 4, #2 rebars as shown in Figure 14. The rebars were held in place by a #2 rebar stirrup at each end as shown in long section of specimen in Figure 15.

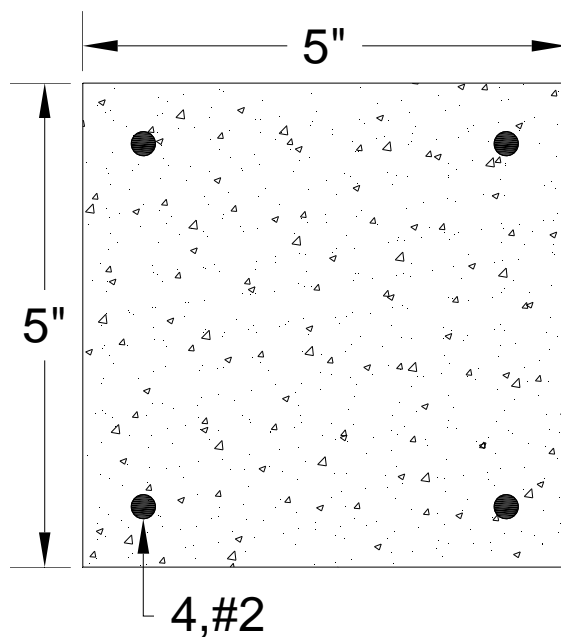


Figure 14. Cross section of SS02

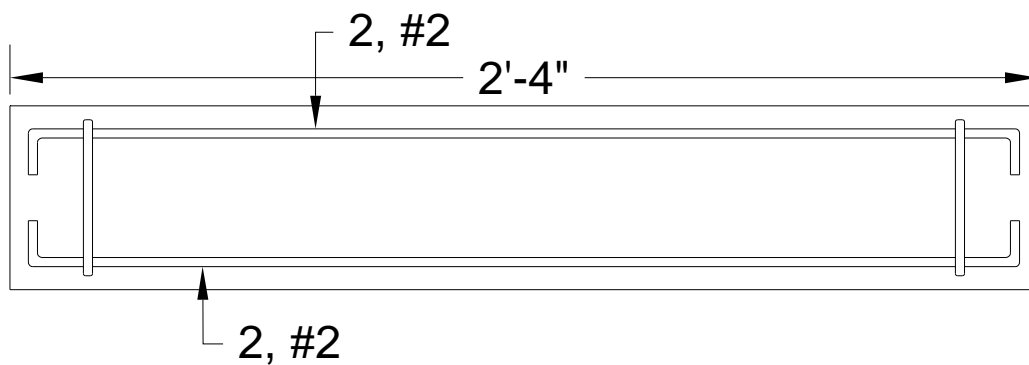


Figure 15. Long section of SS02

The third specimen (SS03) had both longitudinal reinforcement and transverse stirrups. The longitudinal reinforcement consists of 4, #2 rebars as shown in Figure 16. The shear reinforcement was provided by #2 stirrups at a distance of 5 in. center-to-center as shown in long section of specimen in Figure 17.

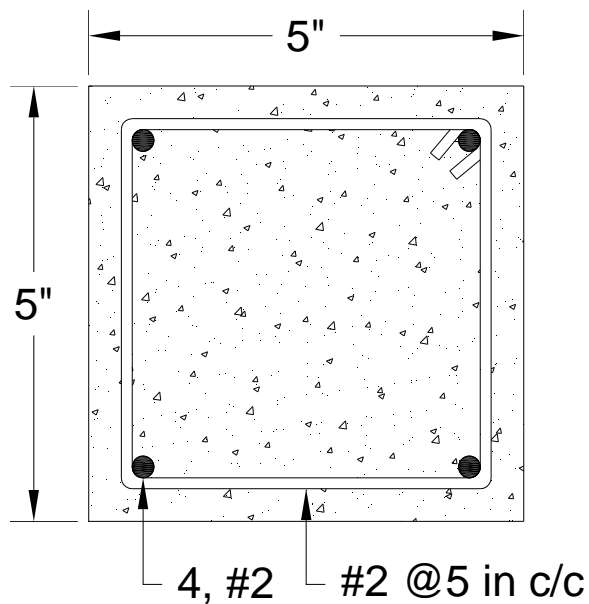


Figure 16. Cross section of SS03

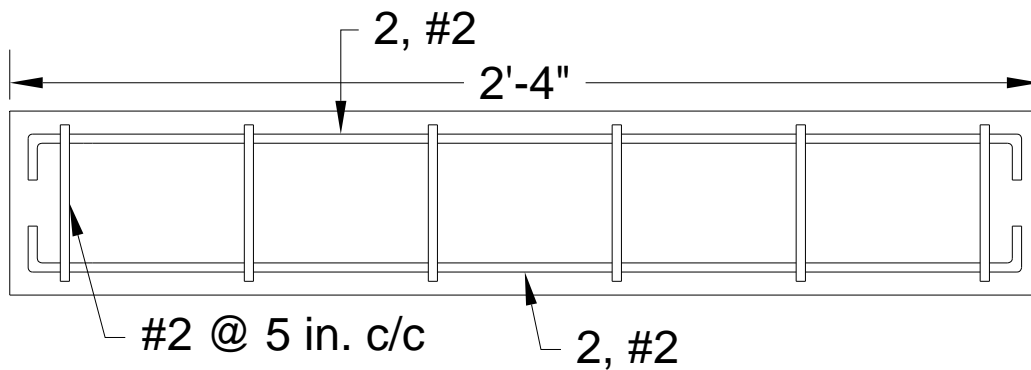


Figure 17. Long section of SS03

2.3.2 Spandrel Members of L-Shaped Cross Section

A total of sixteen isolated spandrel members of L-shaped cross section were tested. A plain concrete specimen was tested first as a control member. The cross sectional details of this member are shown in Figure 18 and the long section is given in Figure 19. The cross sectional dimensions shown in Figure 18 are used for all L-shaped spandrel members. According to ACI 8.12.3 [24], the effective flange width was calculated to be 2 in. These dimensions correspond to the dimensions of spandrel members of the slab-beam specimens. A geometric scale factor of 2 was used to scale down the dimensions to half of that used in slab-beam specimens. For example, the overall depth of isolated spandrel members is 4 in. as compared to 8 in. in slab specimens.

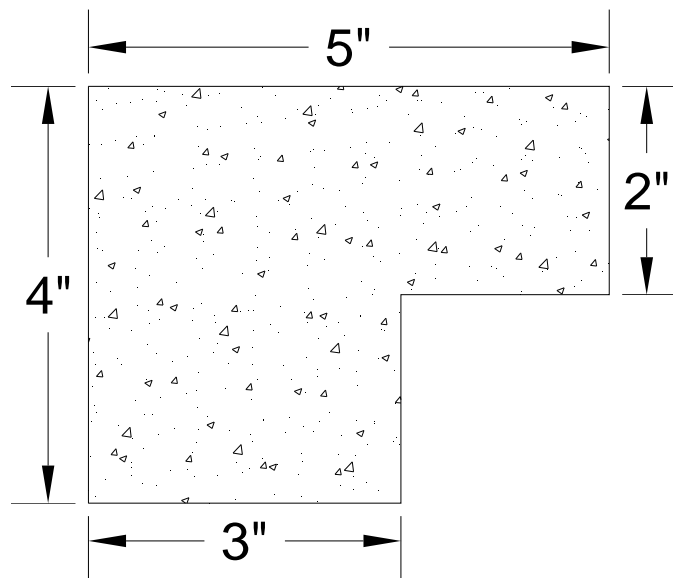


Figure 18. Cross section of SM04

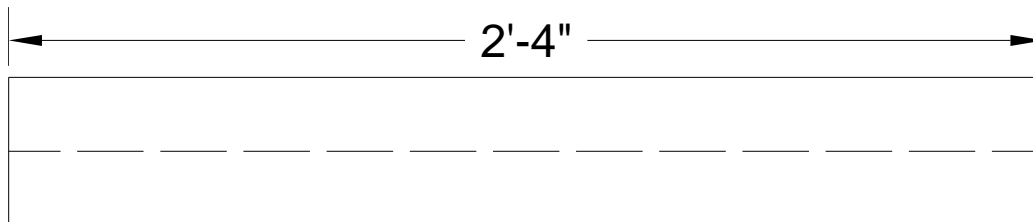


Figure 19. Long section of SM04

The remaining 15 L-shaped spandrel members consist of five sets with three specimens in each set. The cross sectional and long sectional details of the first set are shown in Figure 20 and Figure 21, respectively. The longitudinal reinforcement consists of 2, #2 rebars on the tension side and 2, #2 rebars on the compression side. The shear reinforcement is provided by closed stirrups of the same #2 size rebars at 5 in. center-to-center. All specimens have a total length of 28 in.

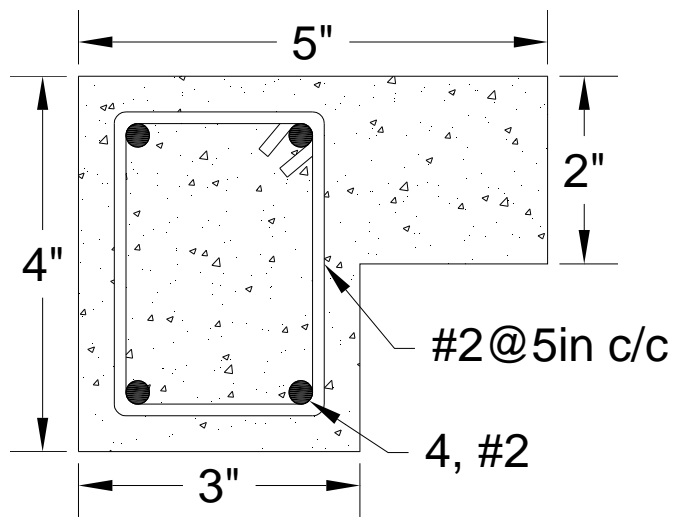


Figure 20. Cross section of SM05-SM07

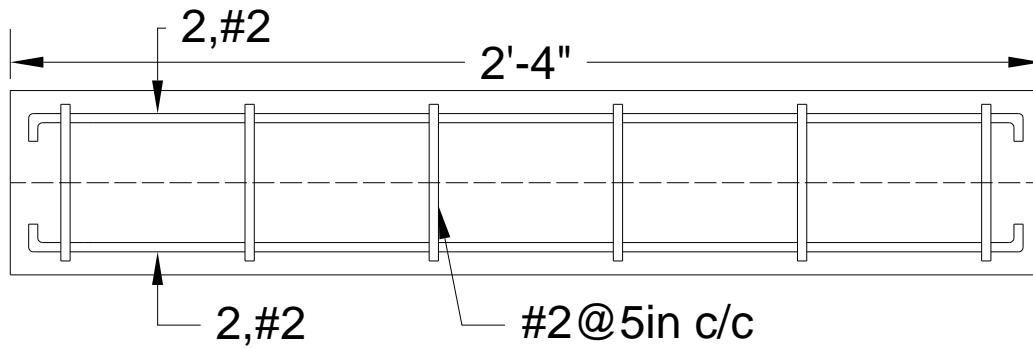


Figure 21. Long section of SM05-SM07

In addition to the longitudinal and transvers reinforcement provided in the web of the cross section as in the first set of specimens, the second set of specimens have a longitudinal rebar in the flange part of each member cross section. Since the flange is actually a part of the slab, therefore this rebar is provided to study the effects of slab reinforcement parallel to the length of the member on the strength and behavior of spandrel members. This rebar was provided in the middle of the flange with a concrete cover of 0.5 in. Figure 22 and Figure 23 show the cross section and long section of the second set of specimens, respectively.

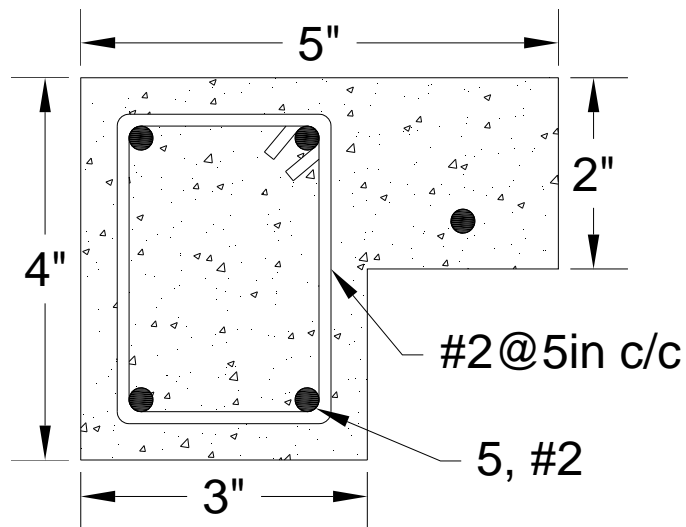


Figure 22. Cross section of SM08-SM10

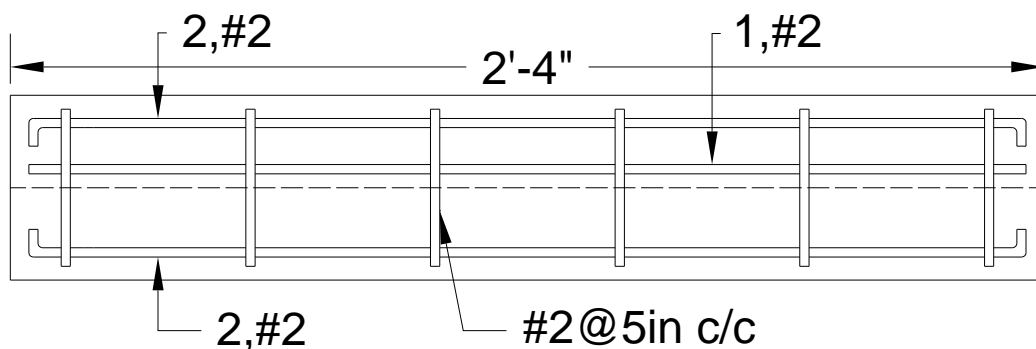


Figure 23. Long section of SM08-SM10

The longitudinal reinforcement of set 3 specimens is similar to that of set 2. However, these specimens have additional transverse straight rebars representing the transverse positive reinforcement in the slab. They are located at 5 in. center-to-center in the middle of transverse stirrups. Figure 24 and Figure 25 show the cross section and long section of set 3 specimens, respectively.

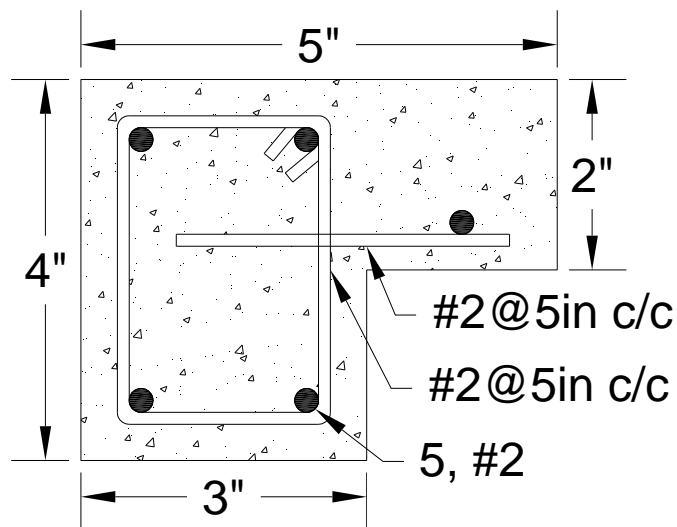


Figure 24. Cross section of SM11-SM13

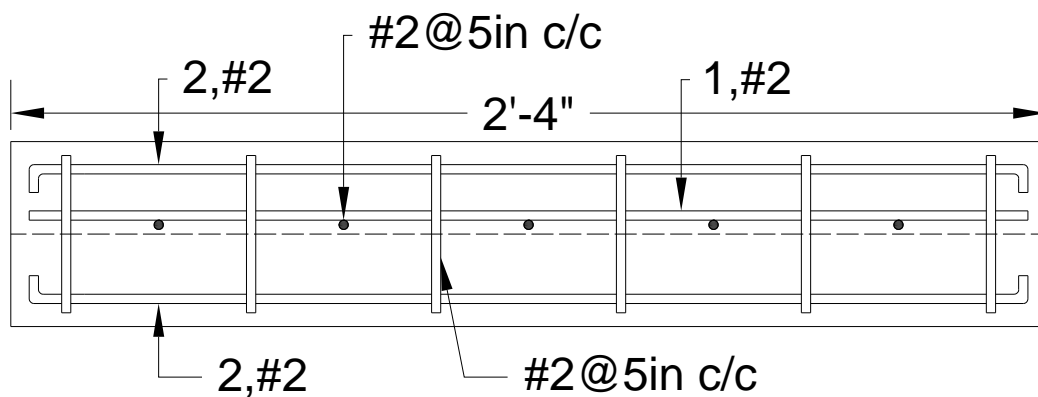


Figure 25. Long section of SM11-SM13

High strength Carbon Fiber Reinforced Polymer (CFRP) strips were used as retrofitting for members in the last two sets of specimens. Three specimens of set 4 have CFRP strips mounted externally and the last three specimens of set 5 have CFRP strips as internal reinforcement. Figure 26 and Figure 27 show the cross section and long section of SM14, respectively. This specimen was tested under torsional moment only. Therefore the retrofitting was applied at the reentrant corner to diminish the stress concentration at the corner.

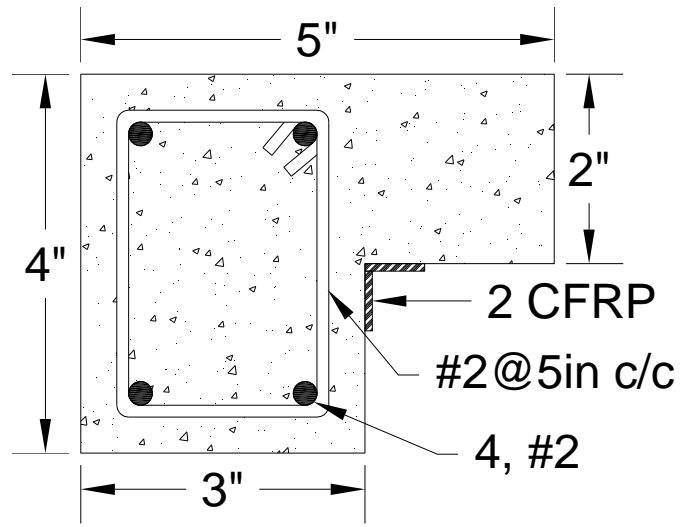


Figure 26. Cross section of SM14 having two external CFRP strips

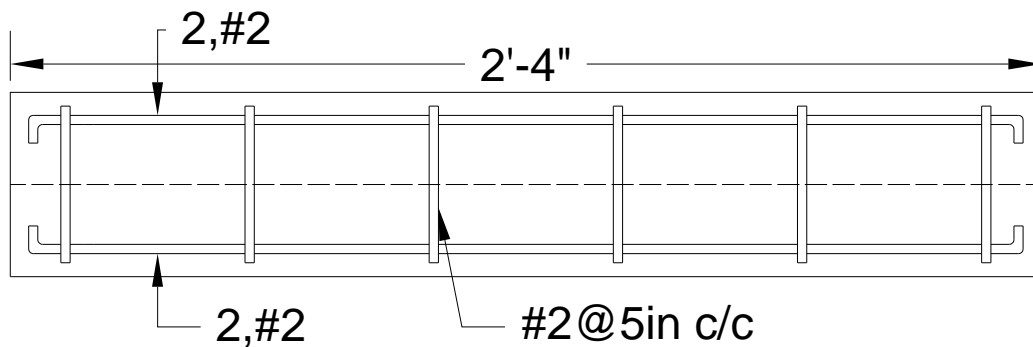


Figure 27. Long section of SM14

The details of steel reinforcement and CFRP retrofitting for SM15 are shown in Figure 28 and Figure 29. This specimen was tested under combined unsymmetrical bending and torsion. Therefore, in addition to the two CFRP strips provided at the reentrant corner in SM14, three CFRP strips were installed on the tension side and one on the compression side as shown in Figure 28. The exact locations of these elements were decided based on the cracking pattern of

similar unretrofitted specimens and after numerically comparing the results of many possible combinations. The details of this numerical study is given in Chapter 3.

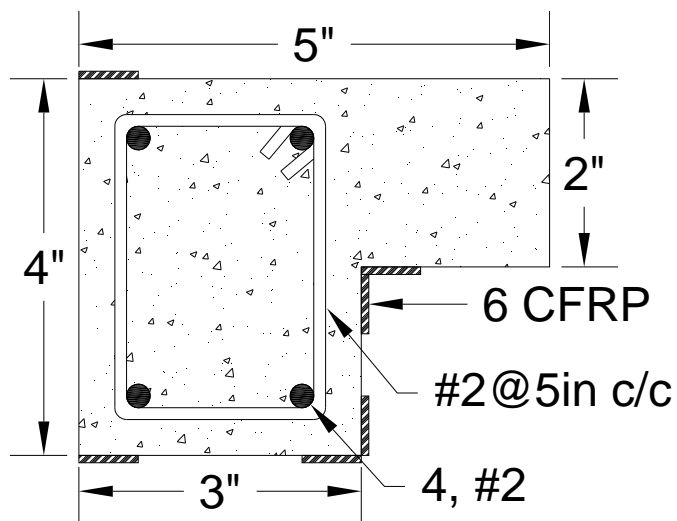


Figure 28. Cross section of SM15

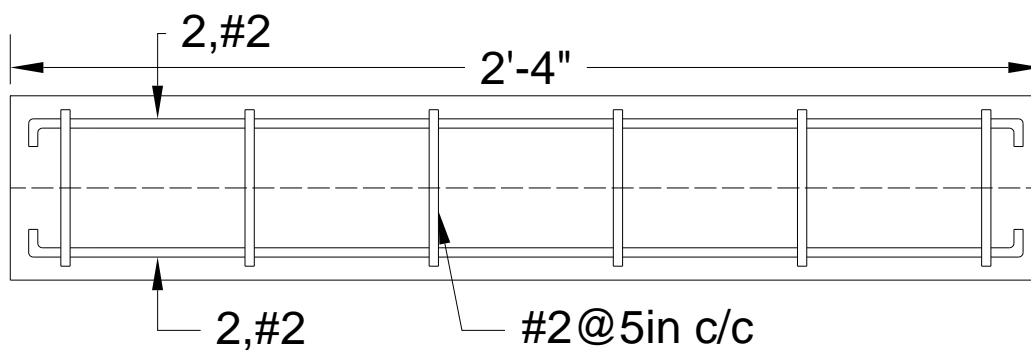


Figure 29. Long section of SM15

The details of steel reinforcement and CFRP retrofitting for SM16 are shown in Figure 30 and Figure 31. In addition to six CFRP provided for SM15, two strips were installed on the flange tip

on each side and one strip at mid depth on the web. The flange experienced cracking in the unretrofitted tests of similar specimens, therefore additional strips were installed on the flange to study the effectiveness in avoiding such cracking. Similarly diagonal cracks were observed in the unretrofitted specimens on the outer side of the web, therefore a CFRP was installed in the mid depth location to evaluate its effectiveness in avoiding or delaying such cracking.

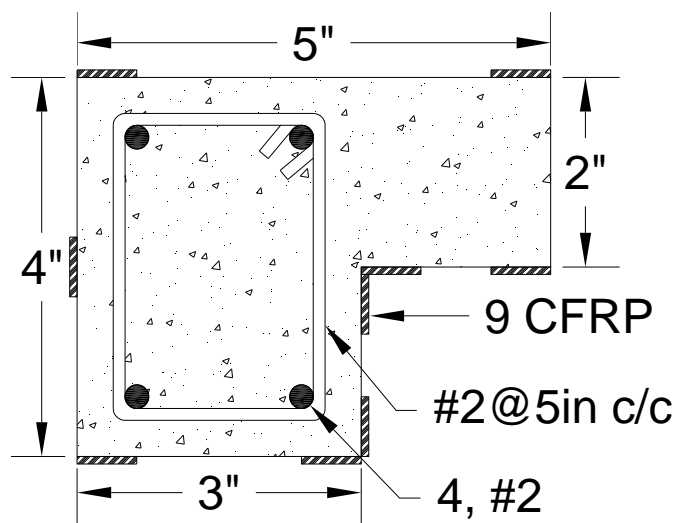


Figure 30. Cross section of SM16

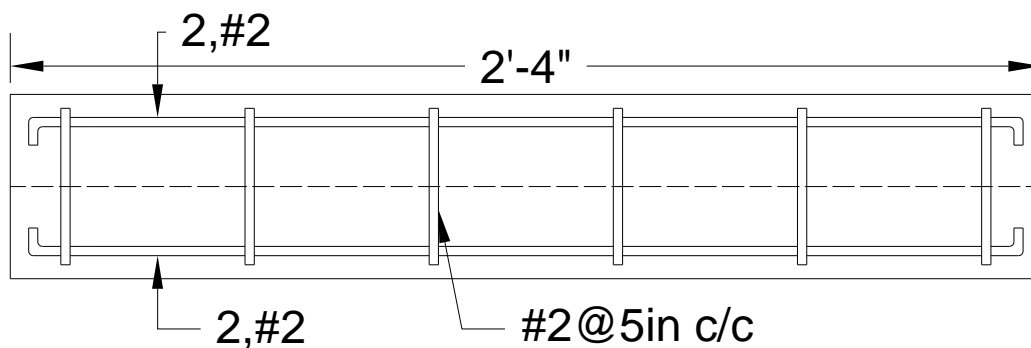


Figure 31. Long section of SM16

The fifth and final set of specimens have an additional steel rebar in the flange and four CFRP strips installed internally before pouring of concrete. The reinforcement and CFRP details are as shown in Figure 32 and Figure 33. The CFRP strips were attached to the steel stirrups with the help of binding wire. These specimens were similar to set 2 in terms of steel reinforcement and were intended to study effects of internal CFRP strips.

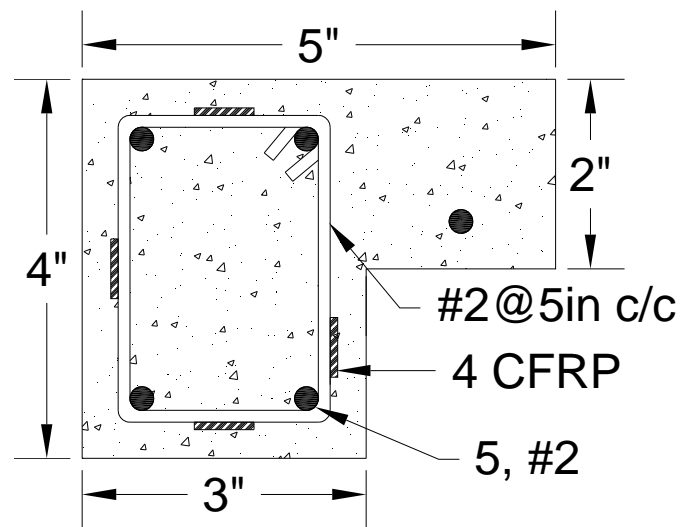


Figure 32. Cross section of SM17-SM19 with internal CFRP strips

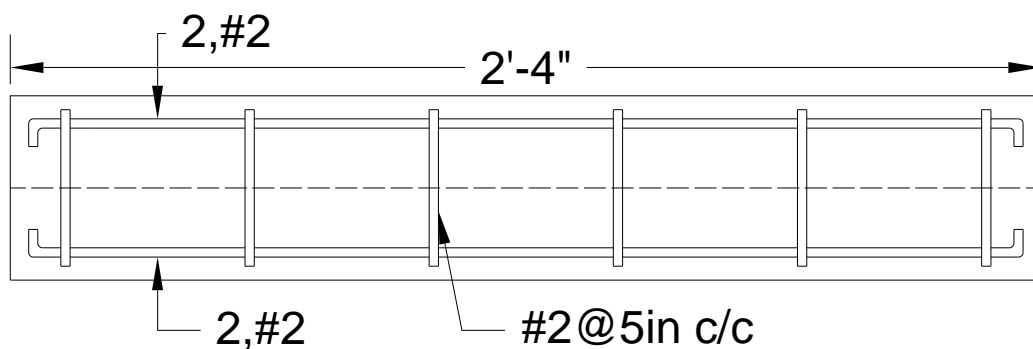


Figure 33. Long section of SM17-SM19

2.3.3 Slabs with Spandrel Members

The third type of specimens investigated as part of the research study consisted of slabs with spandrel members on all four edges. The spandrel members were cast monolithically with the slab and were subjected to bending and torsional moments transferred from the slab under concentrated transverse loading. A total number of three such specimens were fabricated and tested.

The slab specimens represent a scaled model of typical room slab with four edge beams. A geometric scale factor of 2 was selected to arrive at dimensions suitable for the testing facilities available. For example, the overall plan dimensions of 4.5 ft. x 4.5 ft. of the slab correspond to a room dimension of 9 ft. x 9 ft. Companion test cylinders were cast along with each slab specimen. A minimum of 28 days curing period was allowed before the test.

The first slab specimen (SL01) was fabricated and tested under a point load applied at the center of the slab. Based on the results obtained from this test, the dimensions and loading for the final two slab specimens (SL02 and SL03) were modified as discussed in the subsequent sections.

The first slab specimen (SL01) had overall plan dimensions of 48 in. x 48 in. including spandrel members as shown in Figure 34. The slab had a thickness of 2.5 in. The reinforcement was provided isotropically with #3 rebars at a distance of 3 in. center-to-center in both directions, as shown in Figure 35.

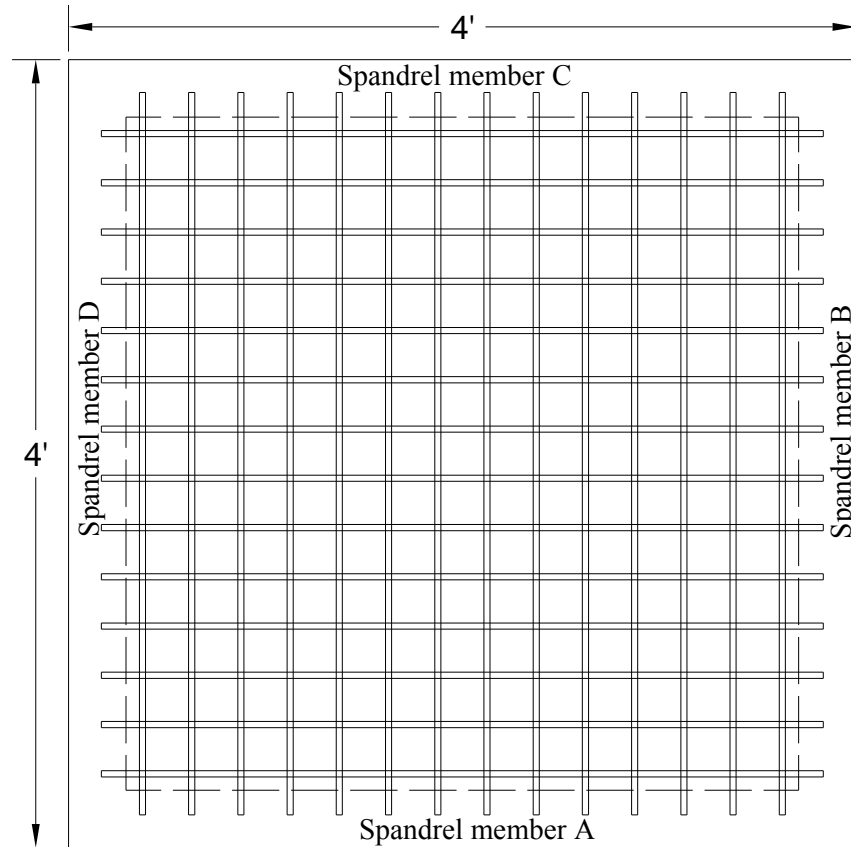


Figure 34. Plan of SL01 showing slab reinforcement

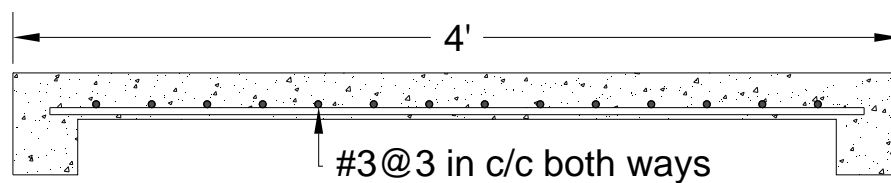


Figure 35. Slab cross section of SL01

The slab was supported on all four edges by spandrel members. Figure 36 and Figure 37 show details of the dimensions and reinforcement for spandrel members in SL01. The spandrel members were 5.5 in. deep and 3.5 in. wide. The spandrel members and slab were cast monolithically so that part of the slab acted as a flange for the spandrel members. According to

ACI 8.12.3 [24], the effective flange width was calculated to be 4 in. The longitudinal reinforcement of the spandrel members was provided by 2, #3 rebars on the tension side. The rebars had a concrete cover of 0.5 in. at the bottom and on the sides. The rebars were bent at the ends to provide appropriate development length. The spandrel members had no shear reinforcement in the first slab specimen.

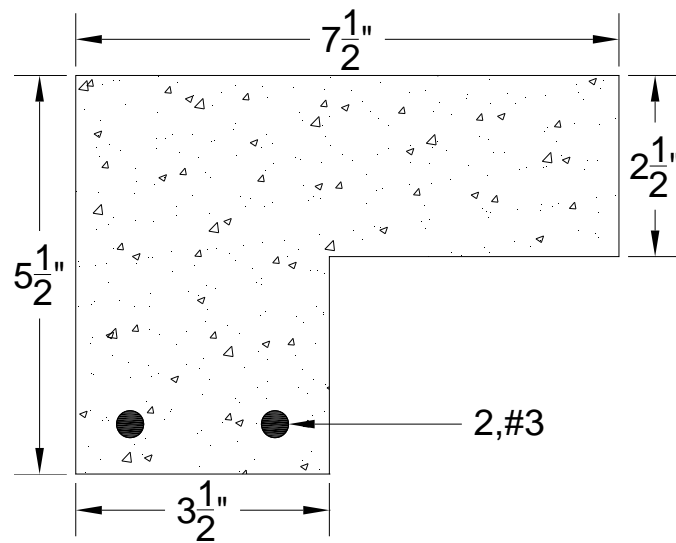


Figure 36. Cross section of spandrel member in SL01

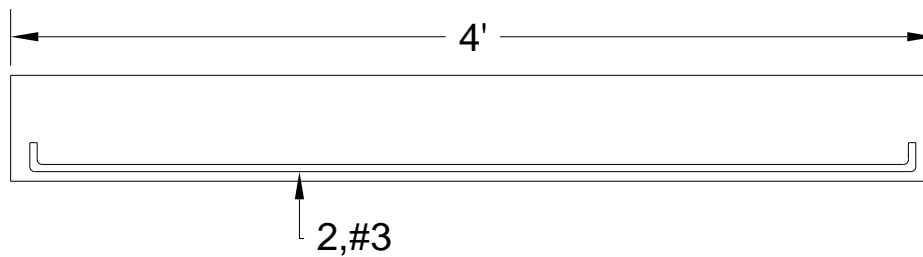


Figure 37. Long section of spandrel member in SL01

The last two slabs (SL02 and SL03) had overall plan dimensions of 54 in. x 54 in. including spandrel members as shown in Figure 38. The slab thickness was 4 in., relatively thick to make sure failure occurs at the spandrel members. The reinforcement was provided isotropically with of #3 rebars at 4 in. center-to-center in both directions, as shown in Figure 39.

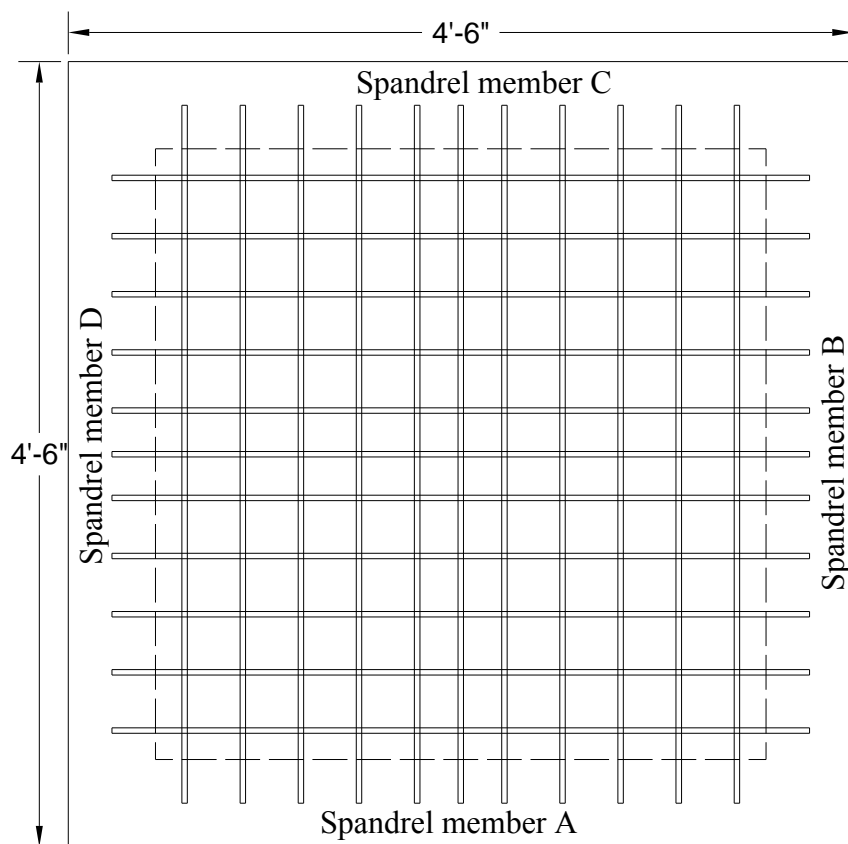


Figure 38. Plan of SL02 and SL03 showing slab reinforcement

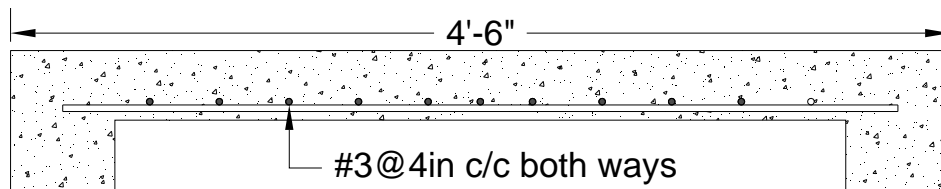


Figure 39. Slab cross section of SL02 and SL03

The spandrel members were provided on all four edges of the slab having dimensions of 8 in. deep and 6 in. wide as shown in Figure 40 and Figure 41. The longitudinal reinforcement consisted of 2, #3 rebars on the tension side and 2, #3 rebars on the compression side. The transverse reinforcement was provided by stirrups at a distance of 6 in. center-to-center. The standard 135-degree hooks were provided in the stirrups. The effective flange width was calculated to be 4 in. based on ACI 8.12.3 [24].

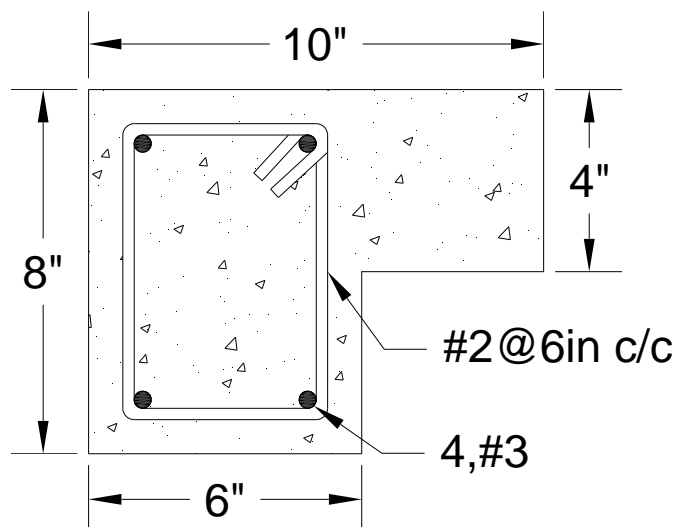


Figure 40. Cross section of spandrel members in SL02 and SL03

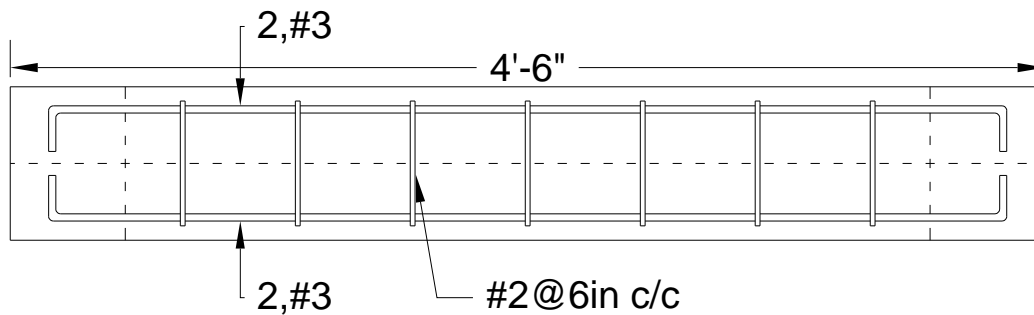


Figure 41. Long section of spandrel members in SL02 and SL03

2.4 Specimen Preparation

The specimen was fabricated at the casting yard of the structural engineering laboratory at Old Dominion University. The reinforcement skeleton was first made and placed in the formwork before pouring of concrete as shown in Figure 42 and Figure 43. Spacers were used to ensure sufficient cover at the bottom and sides. Two hooks made up of reinforcement rebars were placed in slab specimens for lifting. The hooks were anchored with slab reinforcement to avoid overstressing of the slab concrete in the lifting process. Companion test cylinders were cast for each batch of concrete.



Figure 42. Formwork with reinforcement for spandrel members



Figure 43. Reinforcement skeleton in formwork for slab specimens

2.5 Test Setup

All specimens were tested under monotonically increasing quasi static loading. The isolated members were subjected to end moments and torsion. The slab-beam specimens were subjected to point load(s) which induces bending and torsion in the spandrel members at the edges. The subsequent sections discuss the test setups in detail.

2.5.1 Test Setup for Isolated Spandrel Members

The testing apparatus developed by Razzaq and McVinnie [25] for biaxial bending of steel beam-column was used for testing the isolated spandrel members. A similar type of apparatus was designed and fabricated in the Structural Engineering Laboratory of Old Dominion University and used by Sanders [26] and Zhao [27]. Konate [28] modified the same apparatus to apply torsion at the end for testing steel members.

The bending part of the test setup along with a test specimen is shown in Figure 44. The main components shown in the figure are upper end gimbal, lower end gimbal, steel casing for Hydraulic Jack A with Load Cell A, Hydraulic Jack B, and Load Cell B. Figure 45 shows schematic of the bending part of the test setup. A closer view of the lower gimbal is shown in

Figure 46. The upper end gimbal is bolted to the heavy steel cross beam in an upside down position. The cross beam is attached at its ends to steel columns which in turn are anchored to the laboratory test bed forming a large reaction frame.

A solid rectangular steel moment arm having dimensions 1.0 in. x 2.0 in. x 24.0 in. is bolted to the upper gimbal inner box to apply bending moment at the top end of the member as shown schematically in Figure 47. The load is applied through two 75 in. long tie rods having 0.75 in. diameter. The rods are separated at each end by 12 in. long and 0.5 in. thick steel plates. The top plate B sits on the machined arm with the help of ball and socket arrangement. The bottom plate B is attached to a 22 kips. capacity compression Load Cell B through a similar arrangement. Load Cell B is mounted on Hydraulic Jack B as illustrated in Figure 45. The Hydraulic Jack B is firmly bolted to a small steel reaction frame. The reaction frame is mounted to the laboratory test bed. The Hydraulic Jack B is controlled through an Enerpac manual hydraulic pump.

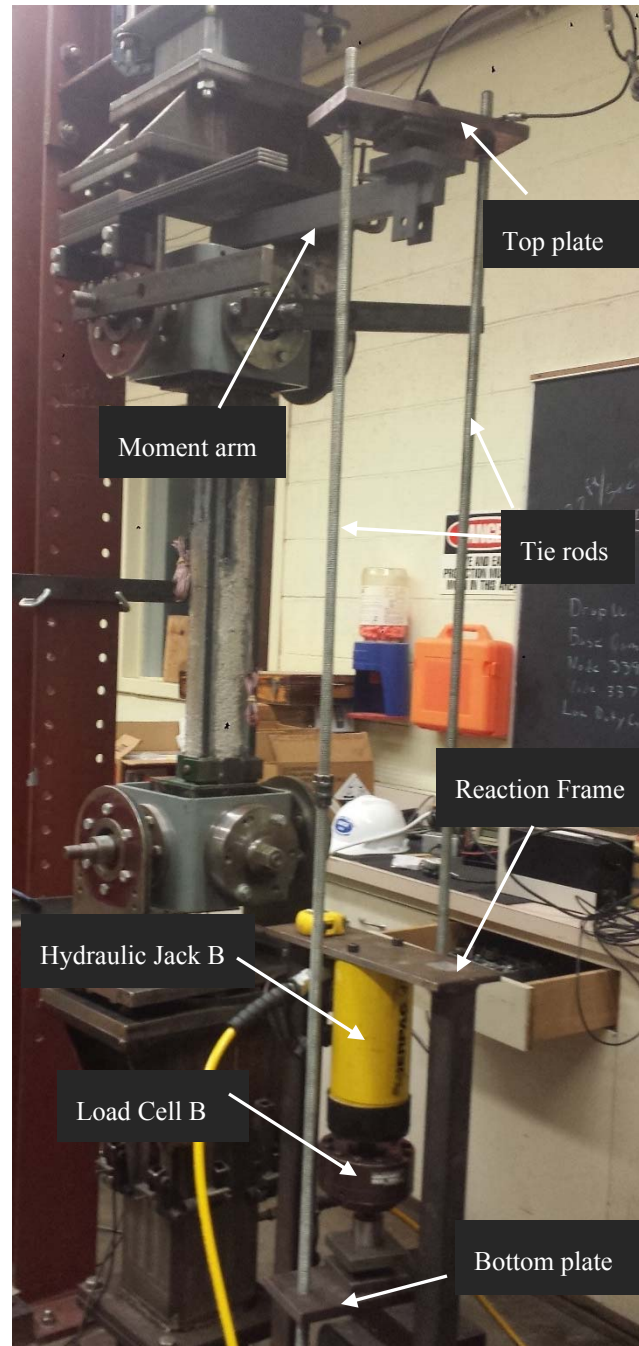


Figure 44. Bending test setup for spandrel members

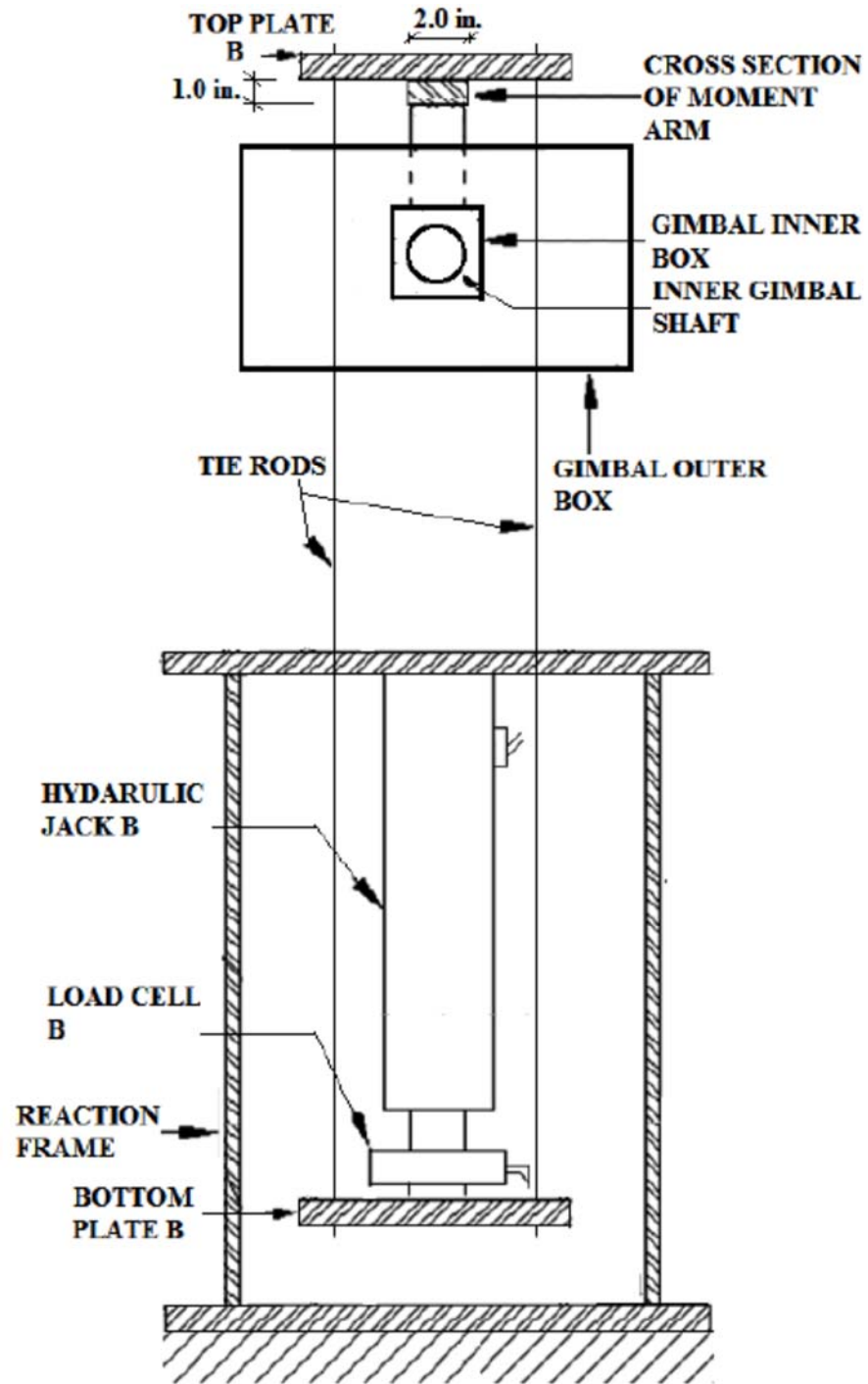


Figure 45. Schematic of portion of apparatus for applying bending [28]

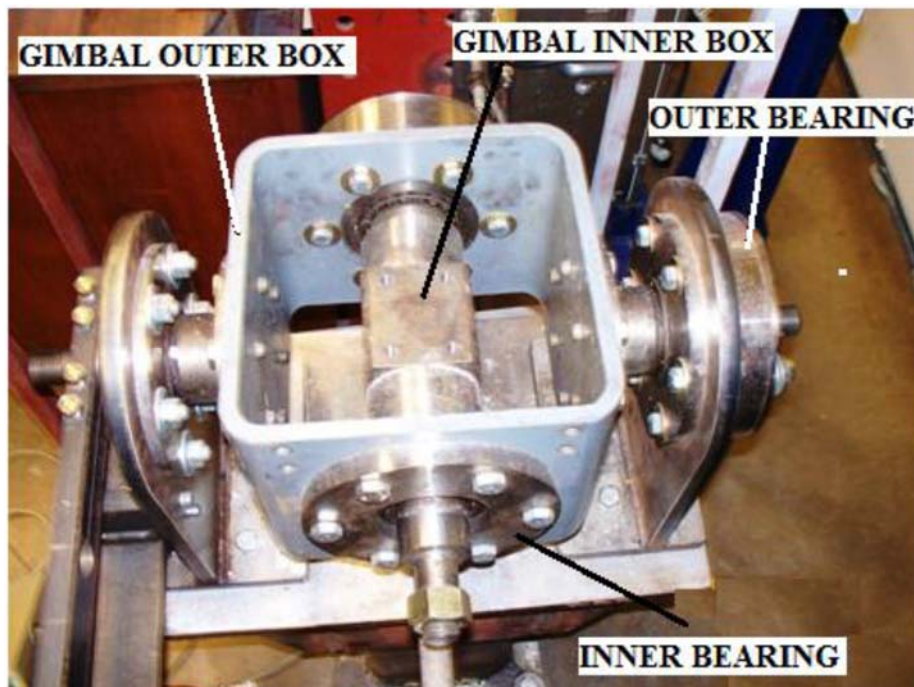


Figure 46. Lower end gimbal [28]

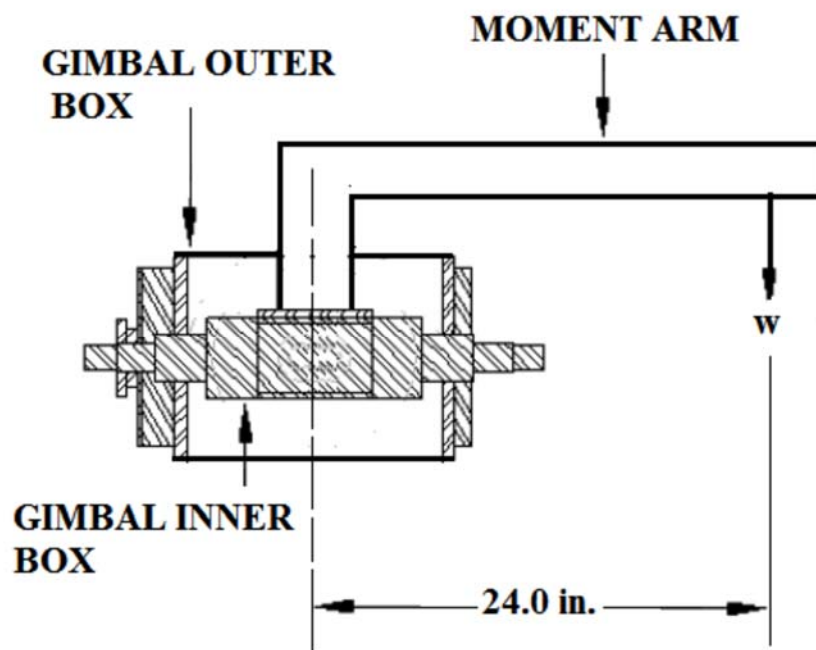


Figure 47. Schematic of moment arm attached to upper gimbal [28]

The torsion apparatus along with a test specimen is shown in the Figure 48 and Figure 49 shows schematic of the portion of the apparatus for applying torsional moment. The eccentric force generating torsional moment at the bottom end is applied through Hydraulic Jack C and measured by Load Cell C. The load is transmitted to the specimen by a chain, as shown in Figure 48. The bottom end gimbal is attached to Steel Plate 1 which rotates on solid steel spheres, as shown schematically in Figure 49. A shaft is welded to the Steel Plate 2 which is connected to the circular bearing on Steel Plate 1. When an eccentric load is applied, Steel Plate 2 rotates freely on Steel Plate 1.

The apparatus is further modified for testing concrete specimens. A square steel box of plane dimensions 6 in. x 6 in. and height 2 in. is attached to the lower gimbal to provide a plan surface for the concrete specimens. Steel plates were welded on the top of the box except on one side which is bolted after placing the specimen. These plates hold the specimens in place during test. Figure 50 shows one such box for L-shaped spandrel members.

The distance between the centerlines of the end gimbals is 37.75 in., which is shown as L_t in Figure 2, and is the length used in the analysis given in Chapter 3. This length includes the actual length L of the specimen and the solid portions of the end fixtures. The bending and torsional moments are applied slowly and incrementally with regular stops to manually record the output data during tests.



Figure 48. Torsion test setup for spandrel members

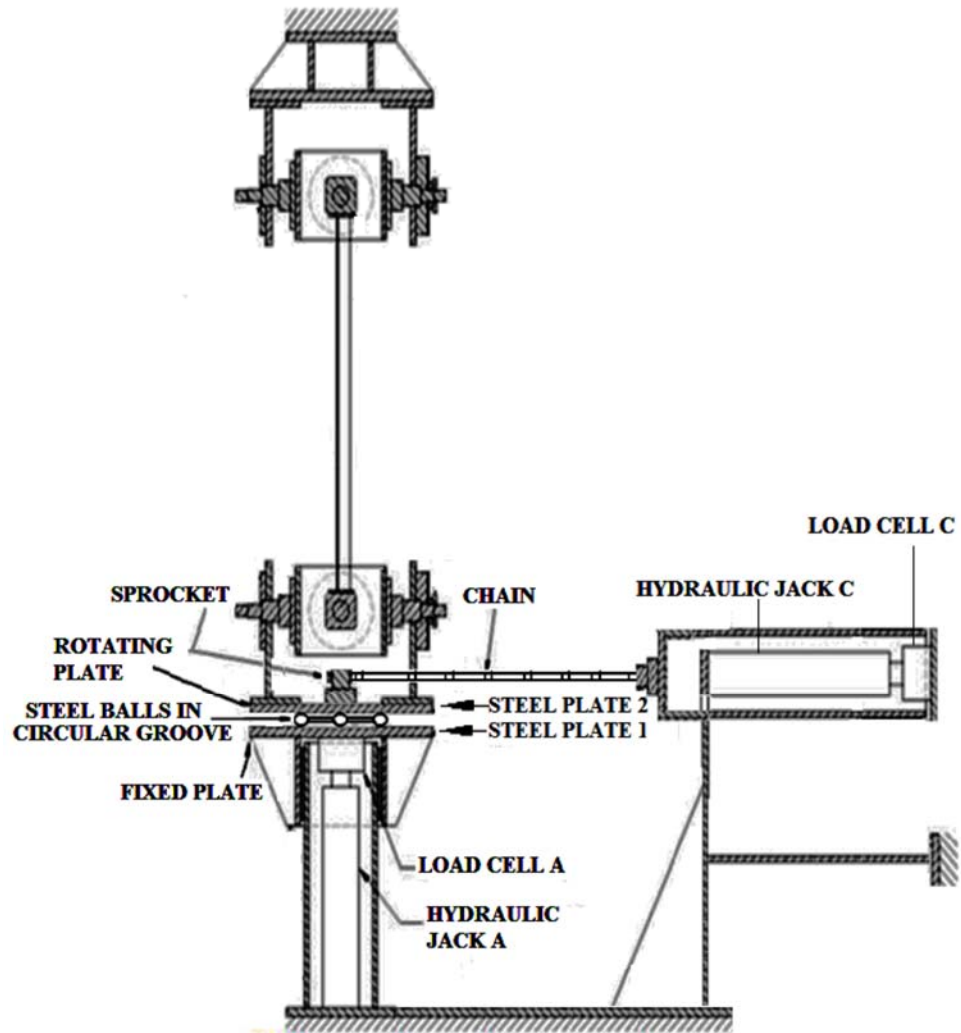


Figure 49. Schematic of a portion of the apparatus for applying torque [28]

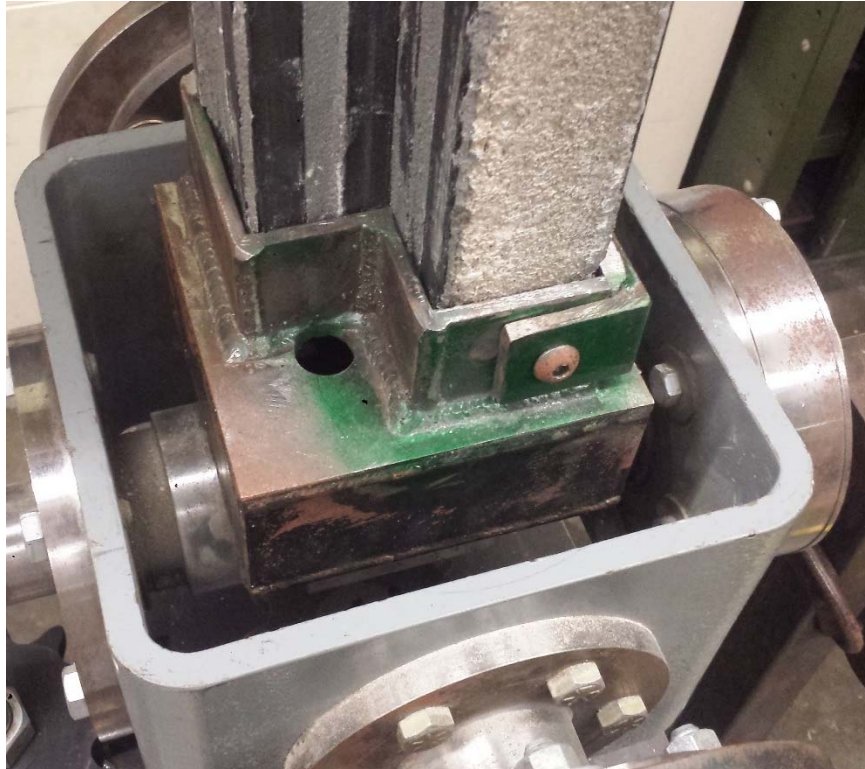


Figure 50. Steel box for connecting and holding specimen

2.5.2 Test Setup for Slab with Spandrel Members

The schematic of a typical test setup for slab specimens is shown in Figure 51 along with a test specimen. A steel frame was constructed to support the specimen during testing. The spandrel members of the specimen were simply supported at four corners on heavy steel columns. The steel columns were made up of 8 in. x 8 in. tubes with $\frac{3}{4}$ in. thick walls as shown in Figure 51. The steel columns were connected through braces so as to avoid any lateral movement during the application of load on the slab. The hydraulic jacks were firmly bolted to a heavy steel cross beam bolted at its ends to steel columns. The columns are anchored to the laboratory test bed. The cross beam along with the steel columns form a strong reaction frame supporting the hydraulic jacks. A 22 kips capacity load cell is attached to each hydraulic jack. The hydraulic jacks were controlled manually through hydraulic pumps. The first slab specimen was tested

under one point load as shown in Figure 52. The remaining two slab specimens were tested under two concentrated loads, as shown in Figure 53 and Figure 54.

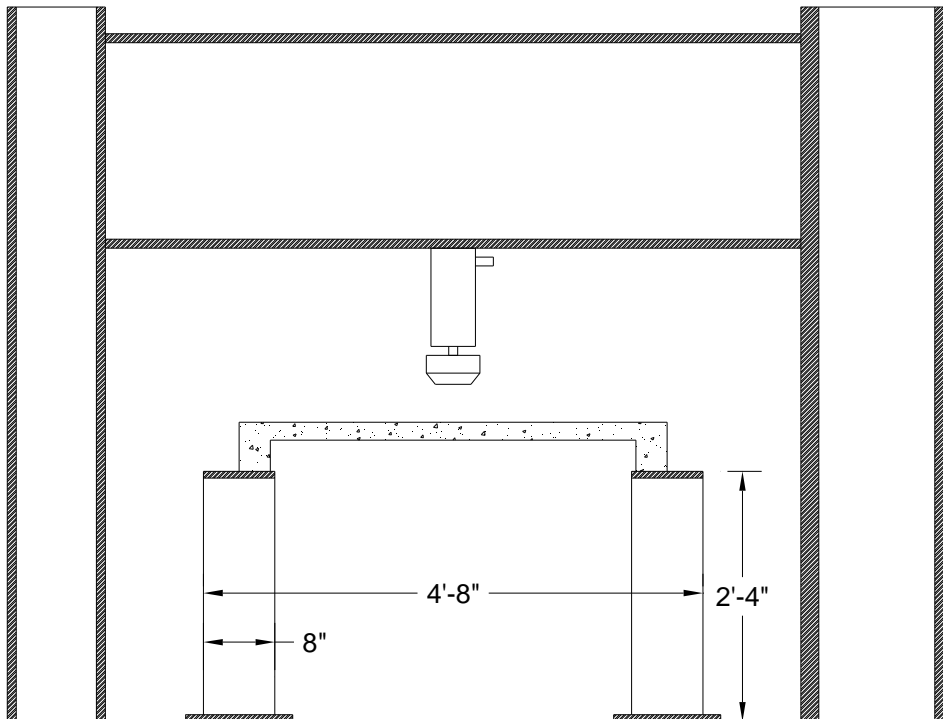


Figure 51. Schematic of test setup for slab with spandrel members



Figure 52. Test setup for SL01



Figure 53. Test setup for SL02



Figure 54. Test setup for SL03

2.5.3 Measurement of Deflection

A number of dial gages were installed to measure displacement at critical points, as shown in Figure 55 for each isolated spandrel member. For isolated spandrel members, the displacement was measured at the supports to monitor their movements, if any, and at the mid height of specimens in both orthogonal directions. Similarly, for the slab specimens, one dial gage was installed at the center of the slab on the bottom side to measure the vertical deflection of slab. The vertical and horizontal deflections of spandrel members were recorded at mid span by means of additional dial gages. The dial gages have a least count of 0.01 in. The dial gages were installed perpendicular to the surface and checked for free movement before the start of each test. Initial readings of all dial gages were noted before the application of load, and also after each subsequent load increment. The load-deflection relations are given in the subsequent sections.

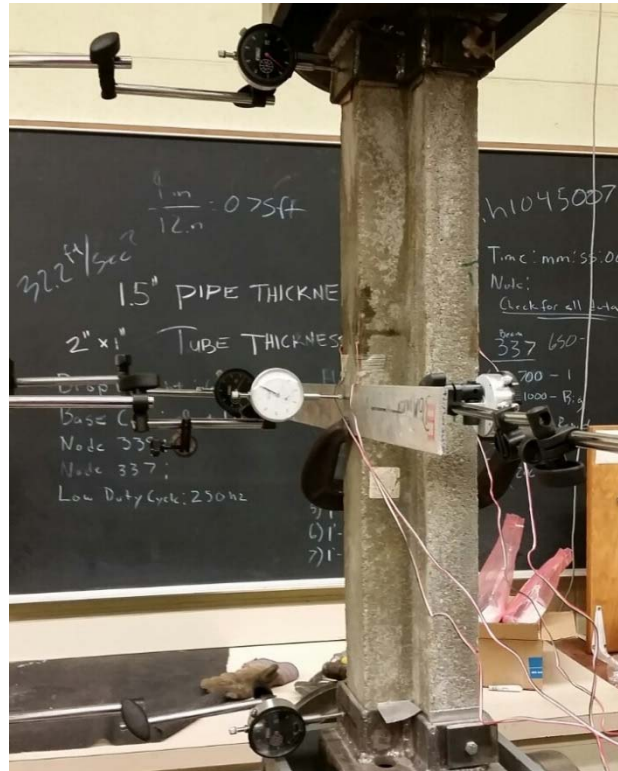


Figure 55. Dial gages for measuring displacements

2.5.4 Measurement of Rotation

Two dial gages were installed at the same location to measure deflections for calculating rotation at a particular section. These dial gages gave two values of member deflections in one direction, so with the distance between the gages known, the rotation of the members can be readily calculated. Figure 56 shows such arrangement of gages for a spandrel member in the slab specimens.

The rotation of the isolated spandrel members was calculated at the bottom and at midheight for specimens involving torsional moment. Similarly for each spandrel member in the slab specimens, the rotation was calculated at midspan. The initial readings of the dial gages were noted down before the application of any load. Then the readings were recorded after each subsequent increments of load. These readings were taken after the system came to a complete static equilibrium as demonstrated by no changes in displacement readings after the application

of each load increment. The torque-angle of twist relations are given and discussed in the subsequent sections.

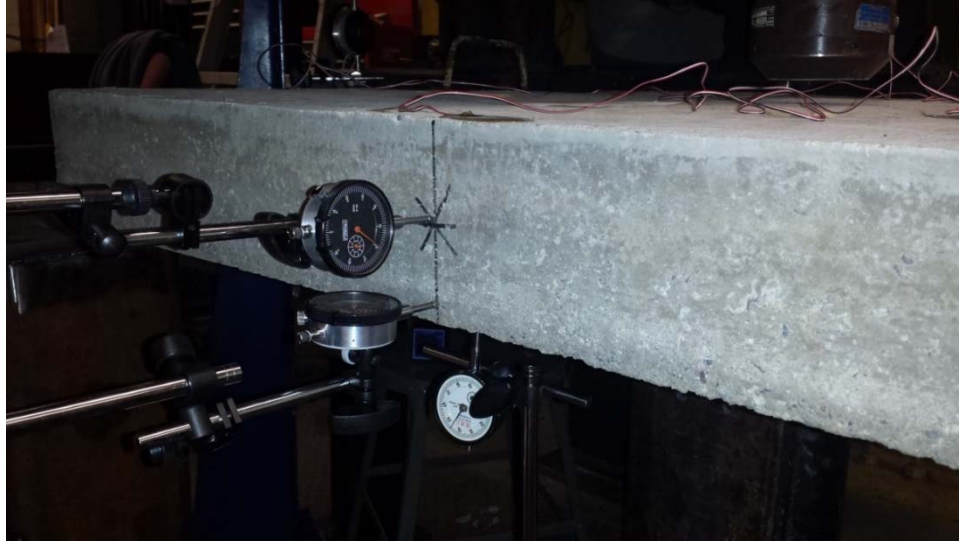


Figure 56. Dial gages to calculate rotation of spandrel members

2.5.5 Measurement of Strains

Four strain gages were installed on each isolated spandrel member at different locations depending upon the type of loading used during the test. They were either installed parallel to the axis of the member to capture maximum normal strains due to bending or at an angle of 45 degrees with the axis of the member to capture maximum normal strains due to torsion. For the retrofitted specimens, some of the strain gages were installed on top of the CFRP strips.

For the first two slab specimens (SL01 and SL02), one strain gage was mounted on each spandrel member to measure the strain on the compression side of the member. They were mounted along the axis of each member at mid span. In case of the third slab (SL03), ten strain gages were mounted at different locations of the spandrel members. Two spandrel members had four strain gages in the same plan at mid span, two on the compression side and two on the

tension side. Each of the remaining two spandrel members had one strain gage on the compression side. Strain readings were recorded using Model P3 strain indicator and recorder by Vishay Micromeasurements, as shown in Figure 57.

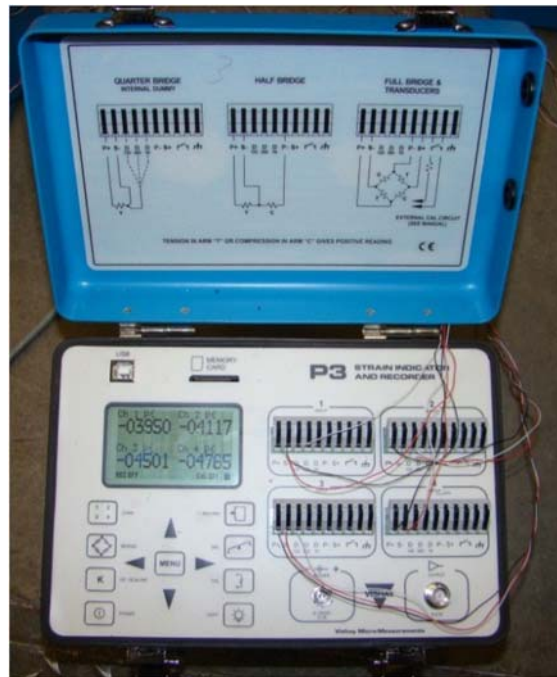


Figure 57. Location of strain gages on spandrel members

2.6 Test Procedures

All isolated spandrel members were subjected to monotonically increasing static loading until failure. The following steps were followed to complete each test:

1. The strain gages were installed on the specimen at proper locations and left untouched for a minimum of 24 hours to develop enough bondage with the surface.
2. The dial gages were mounted at required locations and checked for proper movement before applying any load.
3. The strain indicator was properly charged before starting the test.

4. The load cell meters were given a minimum of half hour warming time before the start of each test.
5. The initial readings of dial gages, strain gages, and load cells were noted before applying any load.
6. A small axial compression load was applied in the beginning of each test to hold the specimen in place during test.
7. For tests with combined bending and torsion loading, the bending moment was applied first to a fraction of cracking bending capacity and then the torsion moment was applied until failure.
8. The load was applied in small increments until failure of the specimen.
9. After each load increment, enough time was given until the system came to a static equilibrium by noting the deflection at regular time intervals.
10. Strain and dial gage readings were noted corresponding to each load increment.
11. The progression of cracks was noted by marking each crack with a number and using markers of different colors.
12. A number of photos were taken during and after the test.
13. The data were recorded and plotted using MS Excel during tests which helped in noticing any mistake in recording data or other erroneous activity during the test.
14. The data were further processed and discussed by compiling a report about each test.

2.7 Test Results of Isolated Members

This section presents the experimental results of spandrel members and slab specimens in the form of load deflection relations. The results are compiled and plotted in MS Excel.

2.7.1 Specimen SS01 Test Results

The isolated member SS01 was tested under combined bending and torsional moments. A moment equal to 35% of the cracking moment of the specimen was applied first. The torsional moment was gradually increased next until failure without increasing the applied bending moment. However, the applied torsion caused a gradual release in the bending moment and it dropped to only 12% of the cracking moment at failure. Figure 58 shows the moment-deflection

relation for SS01 which is a straight line indicating linear elastic behavior before the application of torsional moment. The maximum applied moment was 4.08 k-in. producing a deflection of 92.9×10^{-3} in. deflection. The torque versus angle of twist relation for SS01 is shown in Figure 59. The maximum torsional moment was noted as 9.11 k-in. at angle of rotation of 63.77×10^{-3} rad. The specimen failed in a brittle fashion after reaching the maximum torsion. The cracking pattern of the specimen SS01 at the end of the test is shown in Figure 60.

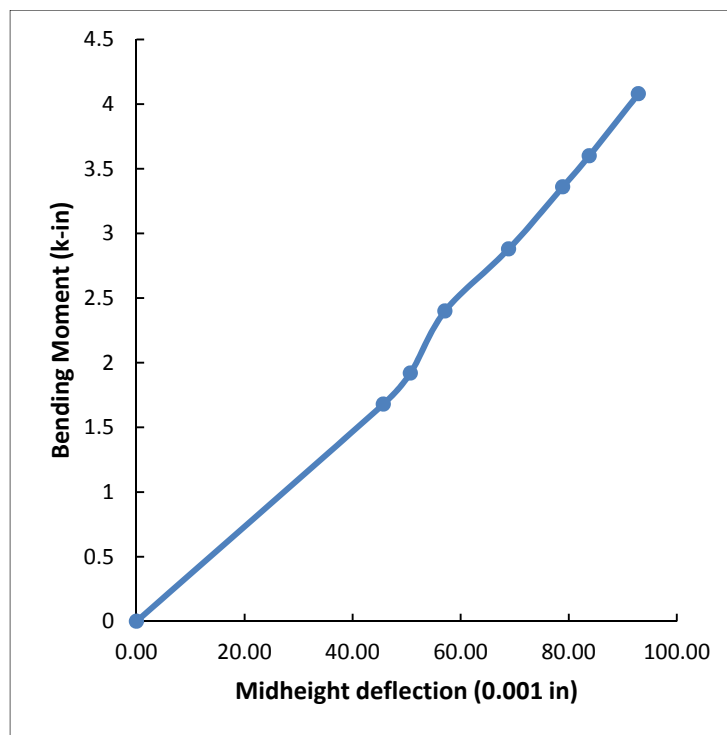


Figure 58. Moment-deflection relation for SS01

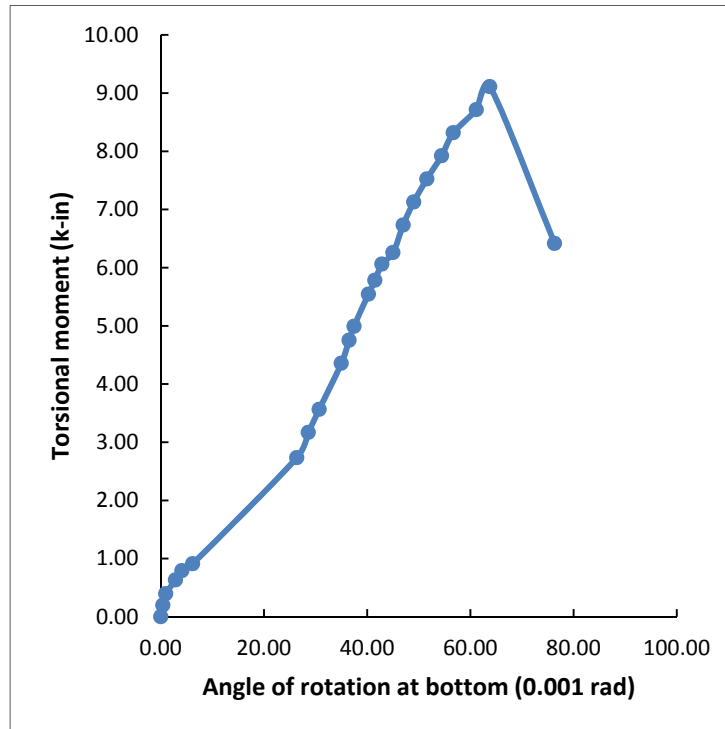


Figure 59. Torque versus angle of twist relation for SS01



Figure 60. Final crack pattern of SS01

2.7.2 Specimen SS02 Test Results

The isolated member SS02 was also tested under combined bending and torsional moments. A moment equal to 25% of the cracking moment of the specimen was applied first. The torsional moment was gradually increased next, until failure without increasing the applied bending moment. However, the applied torsion caused a gradual release in the bending moment and it dropped to only 11% of the cracking moment at failure. Figure 61 shows the moment-deflection relation for SS02 which is almost a straight line indicating linear elastic behavior before the application of torsional moment. The maximum applied moment is 3.12 k-in. producing a deflection of 83.10×10^{-3} in. The torque versus angle of twist relation for SS02 is shown in Figure 62. The maximum torsional moment was recorded as 9.90 k-in. at an angle of rotation of 89.60×10^{-3} rad. The specimen failed in a brittle fashion after reaching the maximum torsion with inclined shear cracking. The cracking pattern of the specimen SS02 at the end of the test is shown in Figure 63.

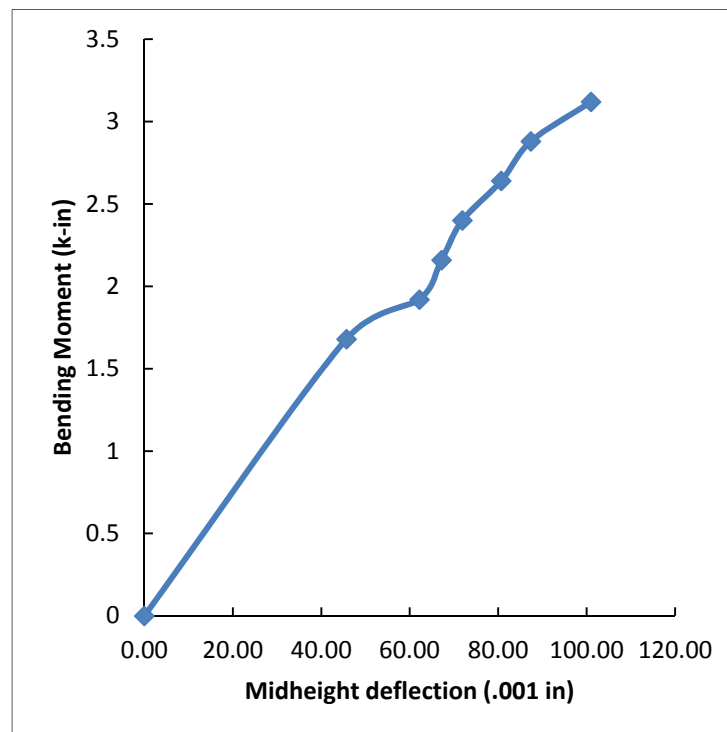


Figure 61. Moment-deflection relation for SS02

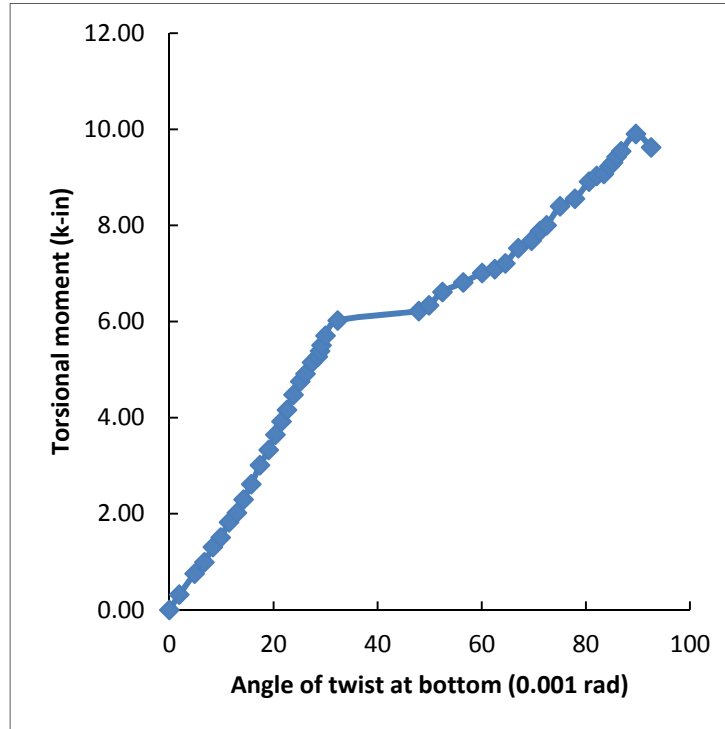


Figure 62. Torque versus angle of twist relation for SS02



Figure 63. Final crack pattern of SS02

2.7.3 Specimen SS03 Test Results

The isolated member SS03 was tested under combined bending and torsional moments. A moment equal to 47% of the cracking moment of the specimen was first applied. The torsional moment was gradually increased next until failure without increasing the applied bending moment. However, the applied torsion caused a gradual release in the bending moment and it dropped to only 11% of the cracking moment at failure. Figure 64 shows the moment-deflection relation for SS03 which is a straight line indicating linear elastic behavior before the application of torsional moment. The maximum applied moment is 6 k-in. producing a deflection of 116×10^{-3} in. The torque versus angle of twist relation for SS03 is shown in Figure 65. The maximum torsional moment was recorded as 13.82 k-in. at an angle of rotation of 104.33×10^{-3} rad. The specimen failed in a brittle fashion due to inclined shear cracking after reaching the maximum torsion. The cracking pattern of the specimen SS03 at the end of the test is shown in Figure 66.

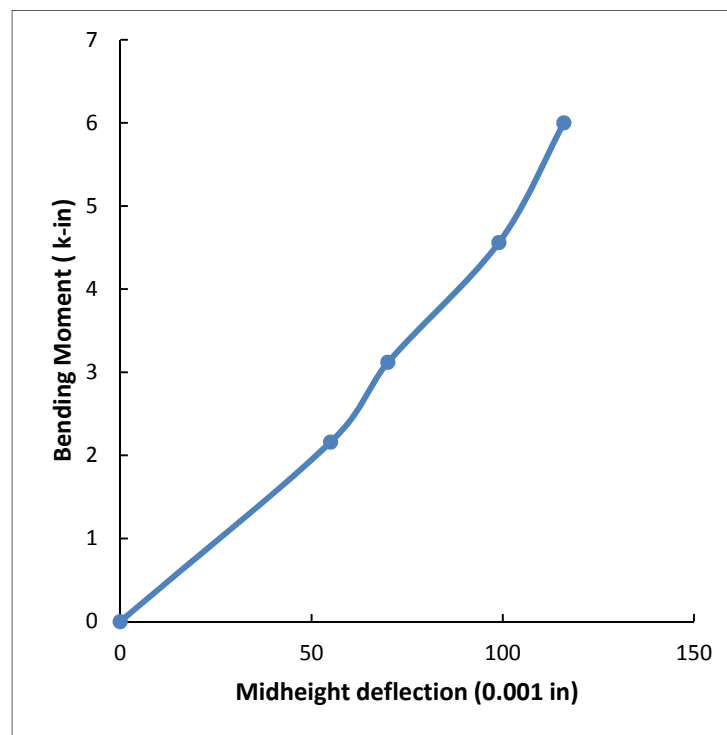


Figure 64. Moment-deflection relation for SS03

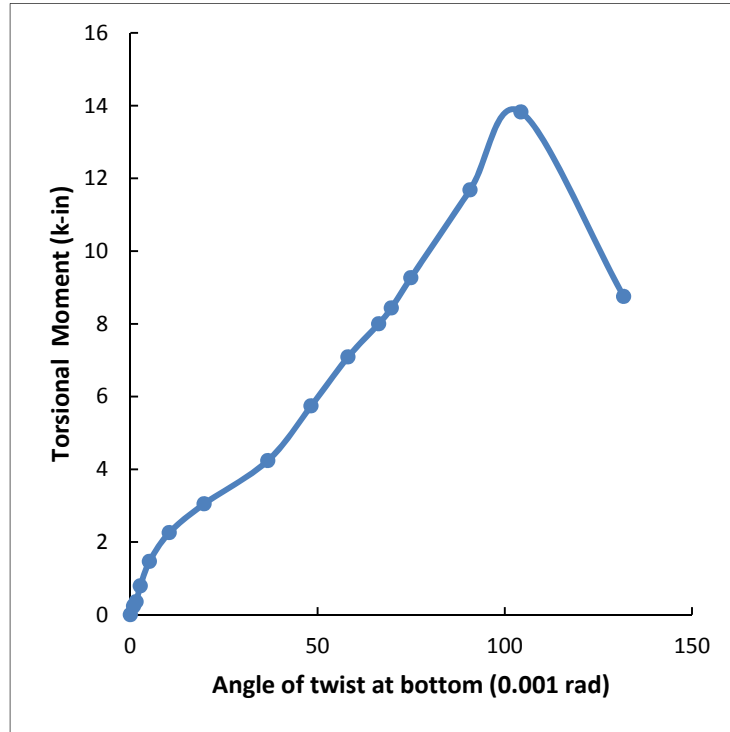


Figure 65. Torque-angle of twist relation for SS03



Figure 66. Final rack pattern for SS03

2.7.4 Specimen SM04 Test Results

The spandrel member SM04 was tested under torsional moment only. Figure 67 shows the torque versus angle of twist relation for SM04. The maximum torsional moment observed was 3.33 k-in. causing a rotation of 26.09×10^{-3} rad. at the bottom. The failure occurred at torsional moment of 2.61 k-in. at an angle of twist equal to 32.36×10^{-3} rad. The relation shows a linear behavior of the member before failure. Figure 68 shows the cracking of the specimen at the end of the test. The cracks are inclined on all the faces except along the depth of the flange and along the width of the web where they are almost normal to the edges. The cracks resulted in a 3D failure surface, as shown in Figure 68.

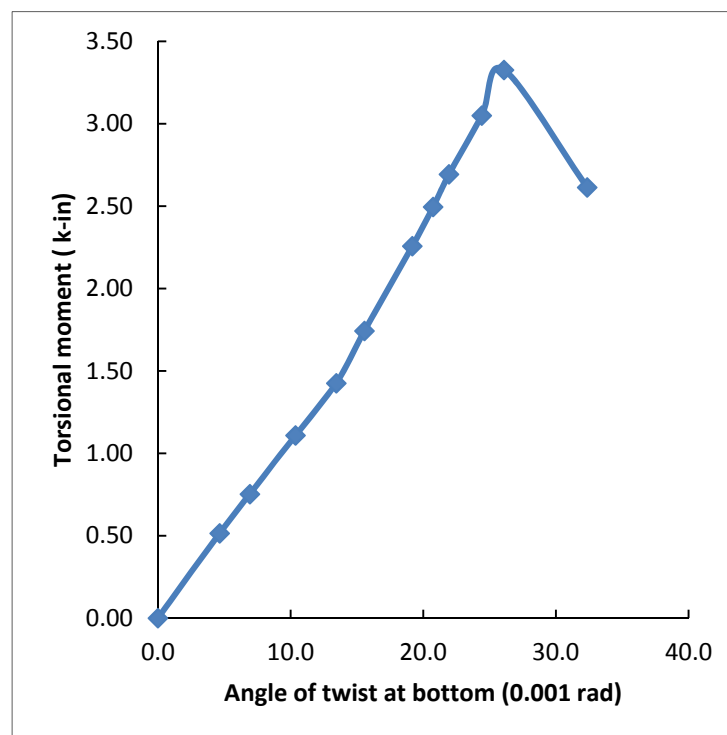


Figure 67. Torque versus angle of twist relation for SM04



Figure 68. Final crack pattern for SM04

2.7.5 Specimen SM05 Test Results

The spandrel member SM05 was tested under torsional moment only. Figure 69 shows the torque versus angle of twist relation for SM05. The maximum torsional moment observed was 4.99 k-in. causing a rotation of 30.80×10^{-3} rad. at the bottom. The failure occurred at torsional moment of 4.40 k-in. at an angle of twist equal to 44.03×10^{-3} rad. Figure 70 shows the cracking of the specimen at the end of the test. The cracks are numbered to show the order of their occurrence. The first crack was developed near the top end at the outside tip of the flange, followed by another crack on the inner tip of the flange at the lower end as marked 1 and 2, respectively. Crack 1 extended along the depth of the flange and further extension occurred with increase in load as marked 3. Crack 4 was the final and longest crack extending along the width of the flange and along depth of the web, as shown in Figure 69.

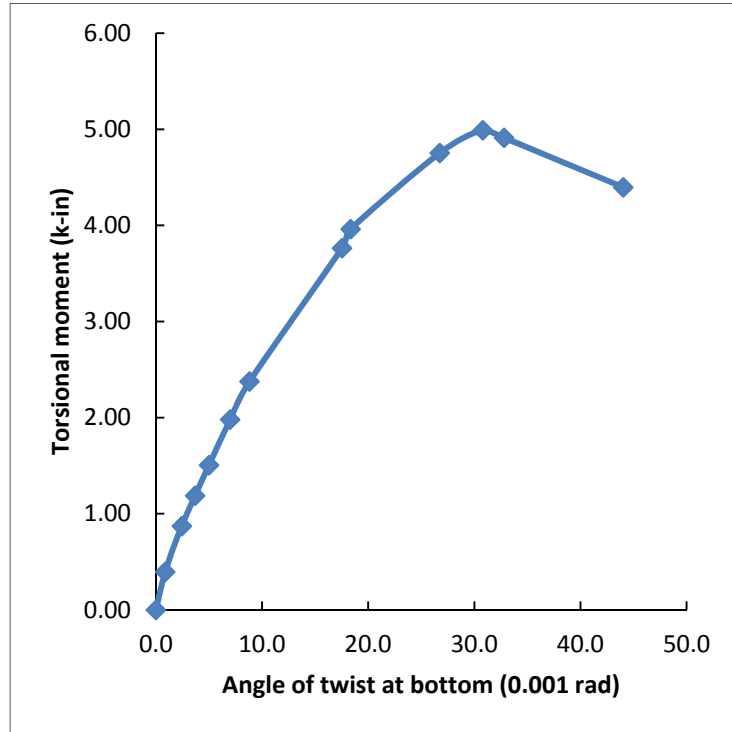


Figure 69. Torque versus angle of twist relation for SM05



Figure 70. Final crack pattern for SM05

2.7.6 Specimen SM06 Test Results

The spandrel member SM06 was tested under bending moment only. However the specimen failed immaturely near the top end of the specimen and no useful data were obtained. The failure pattern is shown in Figure 71. As a result of this test, it was realized that the bending setup (rods and plates) develop a significant bending moment at the top end and must be accounted for in the subsequent tests. In subsequent tests, steel shims were used to fill the gap between the specimen and the steel box at both ends. These shims helped in reducing any slippage and concentration of forces at the ends.



Figure 71. Final crack pattern of SM06

2.7.7 Specimen SM07 Test Results

The spandrel member SM07 was tested under combined bending and torsional moments. A moment equal to 78% of the cracking moment of the specimen was first applied. The torsional moment was then gradually increased until failure without increasing the applied bending moment. However, the applied torsion caused a gradual release in the bending moment and it dropped to only 29% of the cracking moment at failure. Figure 72 shows the moment-deflection relation for SM07. The maximum applied moment is 3.84 k-in. producing a deflection of 31×10^{-3} in. The torque versus angle of twist relation for SM07 is shown in Figure 73. The maximum torsional moment was recorded as 5.15 k-in. at an angle of rotation of 27.71×10^{-3} rad. The failure occurred at torsional moment of 4.36 k-in. at an angle of twist equal to 43.01×10^{-3} rad. Figure 74 shows the cracking of the specimen at the end of the test. The specimen failed in a sudden fashion with no prior cracking. The crack started at the corner of the flange and web, extending in an inclined direction towards the tip of the flange and passing through the whole depth of the flange, as shown in Figure 74.

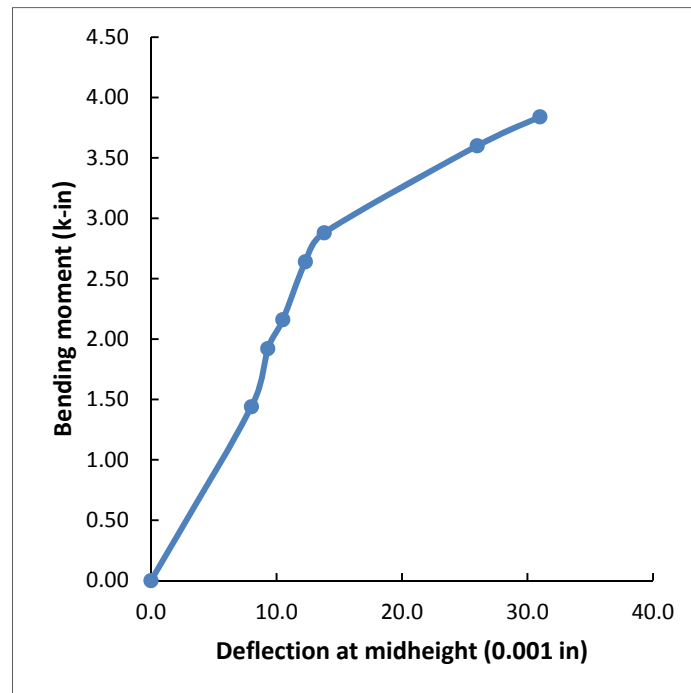


Figure 72. Moment-deflection relation for SM07

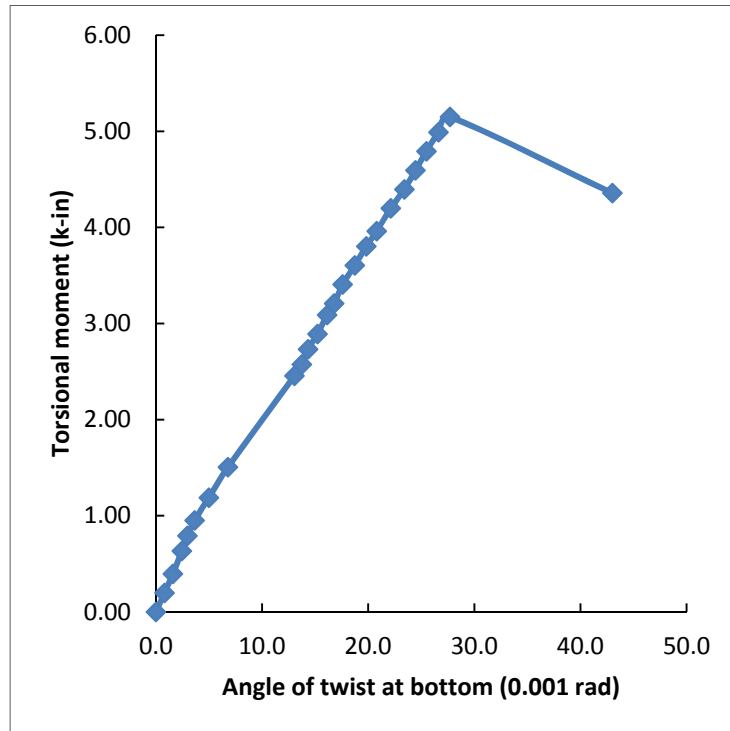


Figure 73. Torque versus angle of twist relation for SM07



Figure 74. Final crack pattern of SM07

2.7.8 Specimen SM08 Test Results

The spandrel member SM08 was tested under torsional moment only. Figure 75 shows the torque versus angle of twist relation for SM08. The maximum torsional moment observed was 5.15 k-in. causing a rotation of 40.67×10^{-3} rad. at the bottom. The failure occurred at torsional moment of 4.36 k-in. at an angle of twist equal to 45.84×10^{-3} rad. Figure 76 shows the cracking of the specimen at the end of the test. The cracking initiated from the corner of the flange and web and extended upward in an inclined direction towards the tip of the flange as shown in the figure. Upon increasing the load, two additional long cracks were developed covering the width of the flange and the depth of the web as marked 3 in Figure 76.

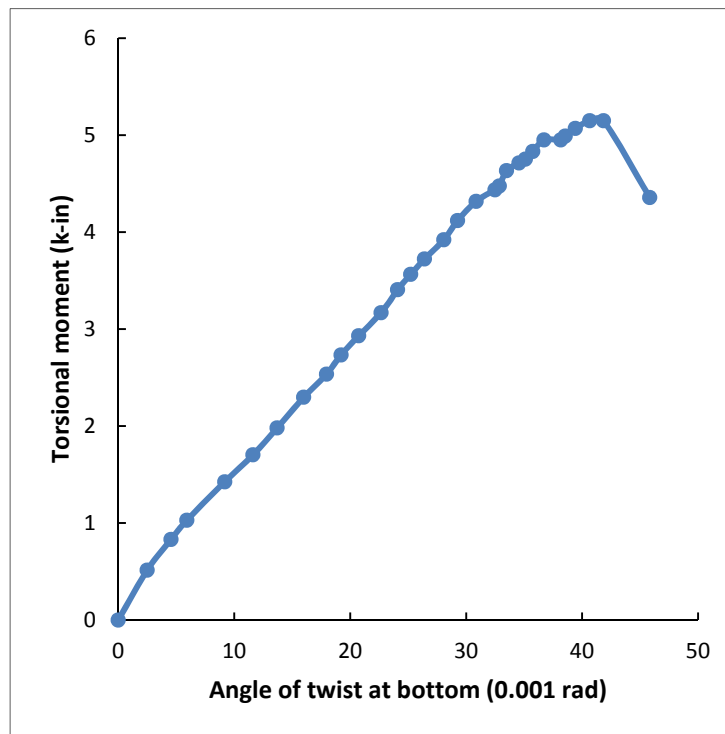


Figure 75. Torque versus angle of twist relation for SM08



Figure 76. Final crack pattern of SM08

2.7.9 Specimen SM09 Test Results

The spandrel member SM09 was tested under bending moment only. Figure 77 shows the moment-deflection relation for SM09. The maximum moment observed was 7.2 k-in. corresponding to a midheight deflection of 293.5×10^{-3} in. The moment at failure was 6.24 k-in. at a midheight deflection of 319×10^{-3} in. Figure 78 shows the cracking pattern of SM09 at the end of the test. The specimen failed locally at the tip of the flange due to high concentrating moment at the top end. No cracks were observed anywhere else in the specimen.

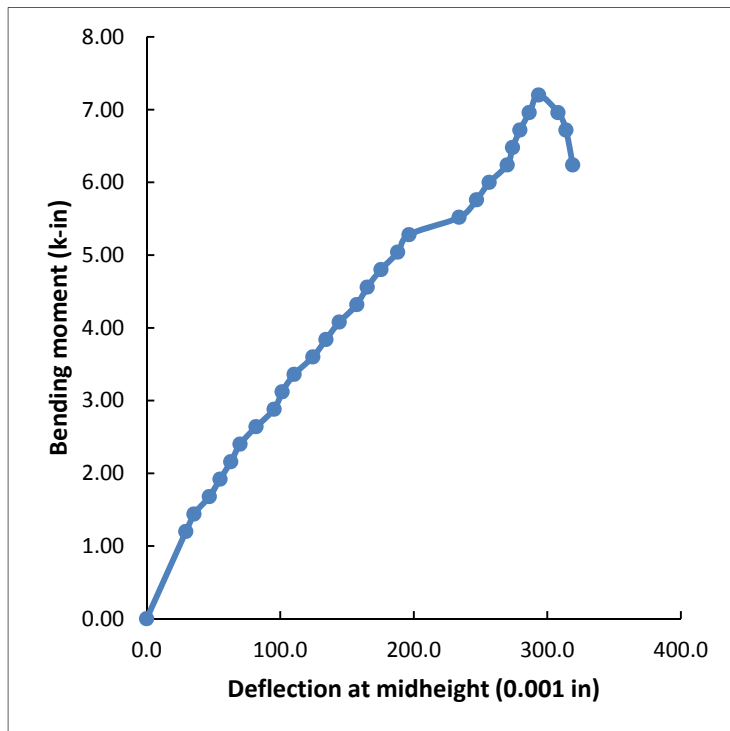


Figure 77. Moment-deflection relation for SM09



Figure 78. Final crack pattern of SM09

2.7.10 Specimen SM10 Test Results

The spandrel member SM10 was tested under the action of combined bending and torsional moments. A moment equal to 49% of the cracking moment of the specimen was first applied. The torsional moment was then gradually increased until failure without increasing the applied bending moment. However, the applied torsion caused a gradual release in the bending moment and it dropped to only 29% of the cracking moment at failure. Figure 79 shows the moment-deflection relation for SM10. The maximum applied moment is 2.40 k-in. producing a deflection of 55.8×10^{-3} in. The torque versus angle of twist relation for SM10 is shown in Figure 80. The maximum torsional moment was recorded as 5.43 k-in. at an angle of rotation of 39.67×10^{-3} rad. The final torsional moment observed was 4.67 k-in. at an angle of twist equal to 42.31×10^{-3} rad. Figure 81 shows the cracking of the specimen at the end of the test. The test was stopped after observing crack 1 extending along the width of the flange and depth of the web, as shown in Figure 81.

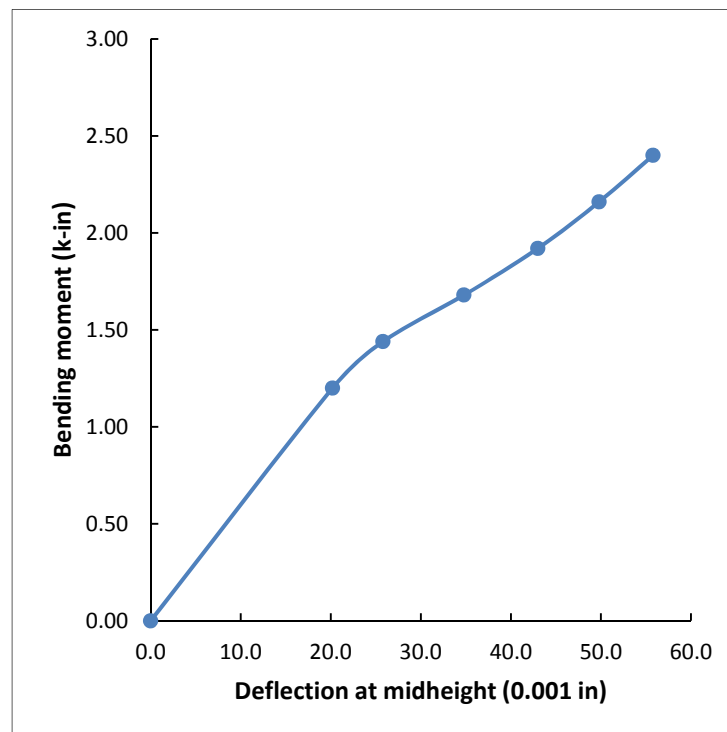


Figure 79. Moment-deflection relation for SM10

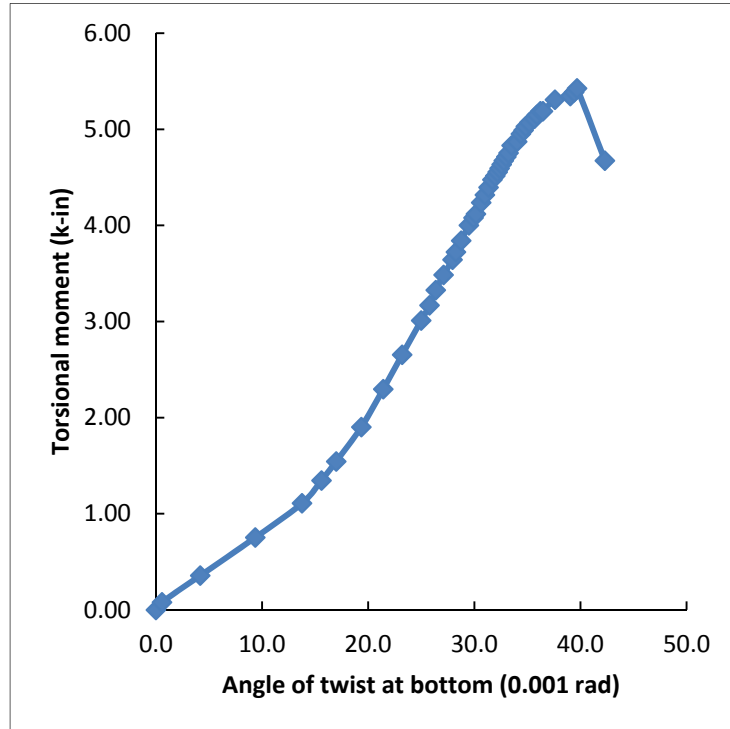


Figure 80. Torque versus angle of twist relation for SM10



Figure 81. Final crack pattern of SM10

2.7.11 Specimen SM11 Test Results

The spandrel member SM11 was tested under torsional moment only. Figure 82 shows the torque versus angle of twist relation for SM11. The test was carried out until minor cracking was observed on the flange tip near the bottom of end of the member as shown in Figure 83. The maximum torsional moment observed was 4.83 k-in. causing a rotation of 40.39×10^{-3} rad. at the bottom. The cracks were developed at a torsional moment of 4.40 k-in. at an angle of twist equal to 41.77×10^{-3} rad.

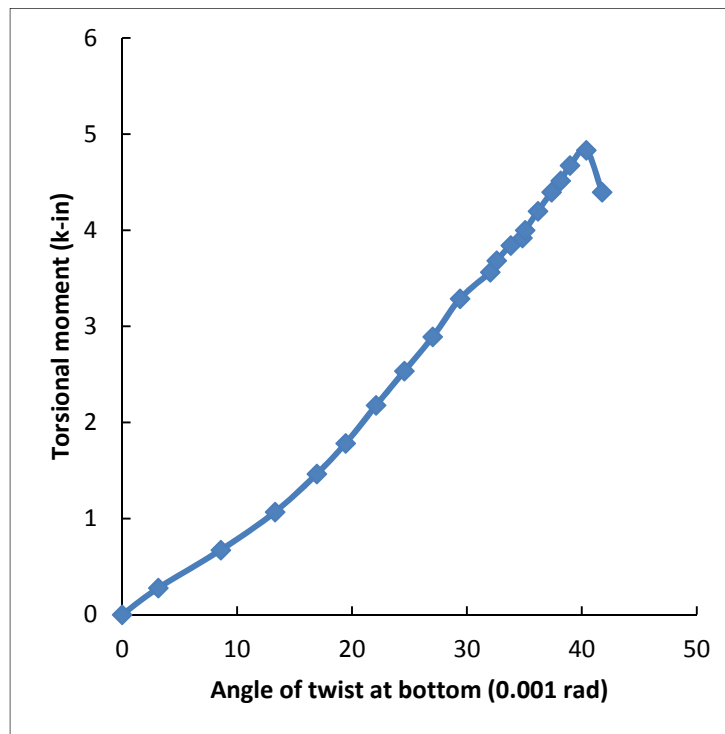


Figure 82. Torque versus angle of twist relation for SM11



Figure 83. Final crack pattern of SM11

2.7.12 Specimen SM12 Test Results

The spandrel member SM12 was tested under the action of combined bending and torsional moments. A moment equal to 54% of the cracking moment of the specimen was first applied and maintained at this level while applying torsion in the next phase. Figure 84 shows the moment-deflection relation for SM12. The maximum applied moment is 2.64 k-in. producing a deflection of 44.3×10^{-3} in. The torque versus angle of twist relation for SM12 is shown in Figure 85. The maximum torsional moment noted was 5.12 k-in. at an angle of rotation of 25.4×10^{-3} rad. The final torsional moment observed was 4.56 k-in. at an angle of twist equal to 29.8×10^{-3} rad. Figure 86 shows the cracking of the specimen at the end of the test. A small crack was developed in the flange near the bottom end followed by a major crack passing through the flange width and depth of the web, as shown in Figure 86.

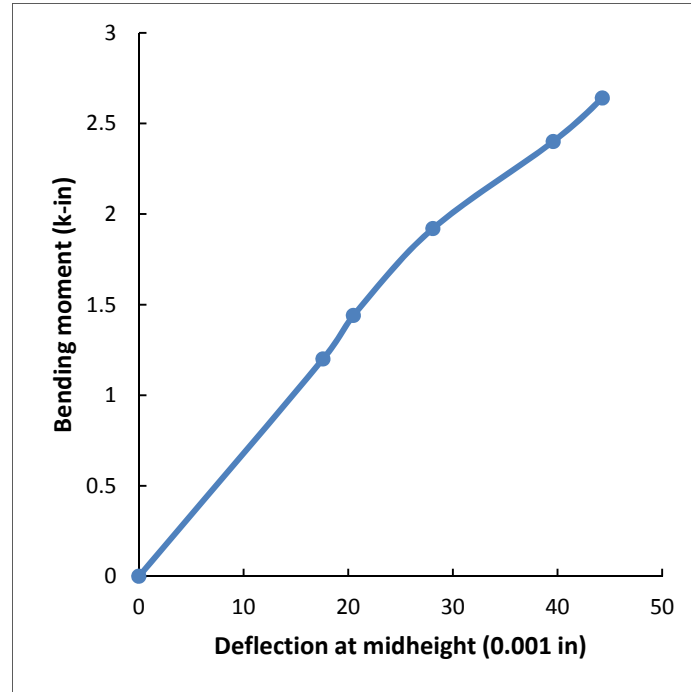


Figure 84. Moment-deflection relation for SM12

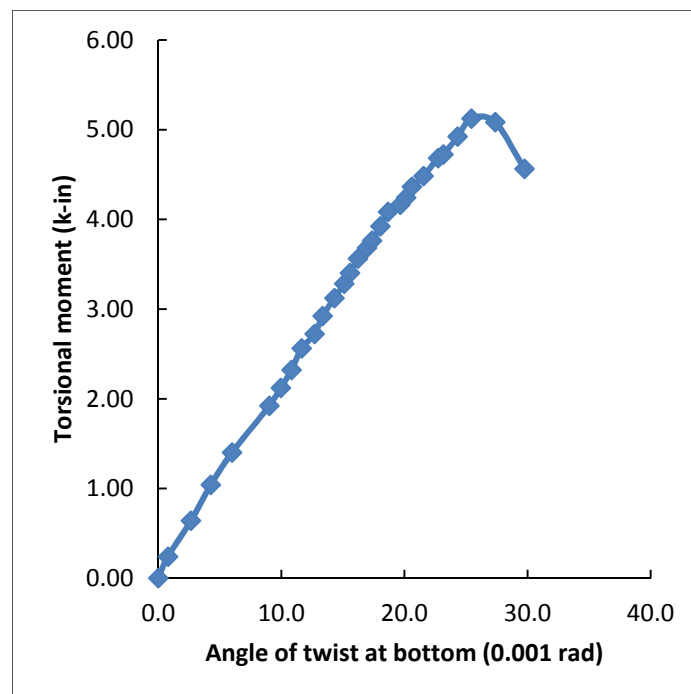


Figure 85. Torque versus angle of twist relation for SM12



Figure 86. Final crack pattern of SM12

2.7.13 Specimen SM13 Test Results

The spandrel member SM13 was tested under the action of combined bending and torsional moments. However torsional moment was applied first in this case. Figure 87 shows the torque versus angle of twist relation for SM13. The torsional moment was applied until minor cracking was observed in the flange near the bottom end as shown in Figure 89. The torque value was 4.40 k-in. at a rotation angle of 43.8×10^{-3} rad. Figure 88 shows the moment-deflection relation for SM13. The failure occurred at a moment equal to 7.2 k-in. producing a deflection of 144.2×10^{-3} in. The failure was caused by cracking of the flange at the top end with widening of the cracks at the bottom, as shown in Figure 88.

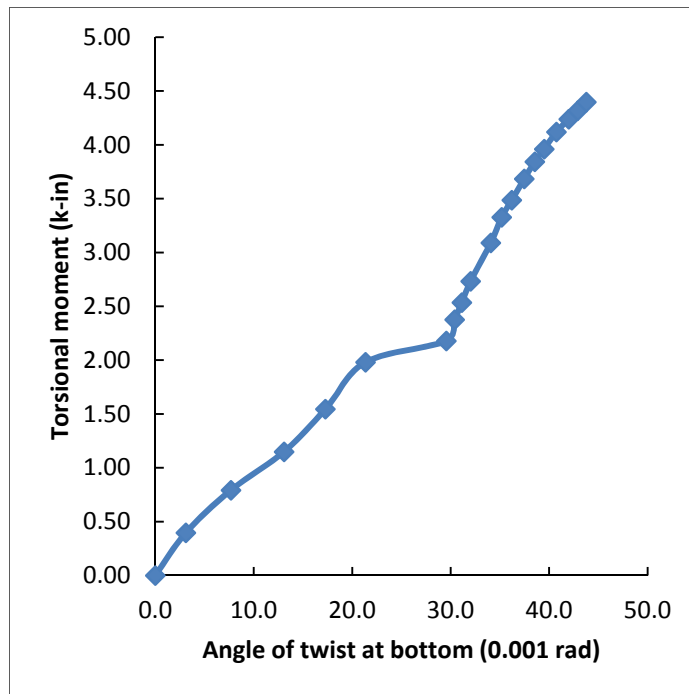


Figure 87. Torque versus angle of twist relation for SM13

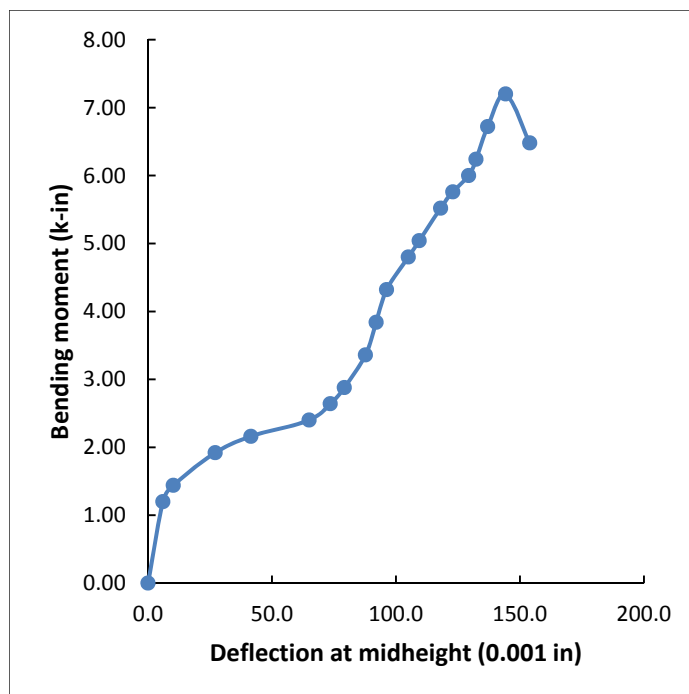


Figure 88. Moment-deflection relation for SM13



Figure 89. Final crack pattern of SM13

2.7.14 Specimen SM14 Test Results

The spandrel member SM14 was tested under torsional moment only. Figure 90 shows the torque versus angle of twist relation for SM14. The maximum torsional moment observed was 5.23 k-in. at a rotation of 45.11×10^{-3} rad. at the bottom. The failure occurred due to inclined cracks on the flange face and along the depth of the web as shown in Figure 91. The torsional moment at this point was 4.91 k-in. at an angle of rotation equal to 48.79×10^{-3} rad.

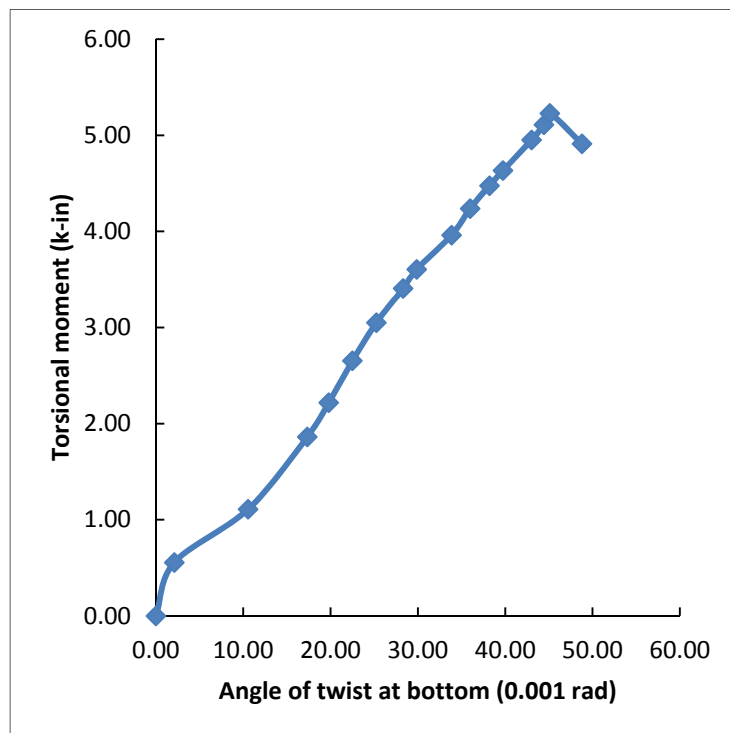


Figure 90. Torque versus angle of twist relation for SM14



Figure 91. Final crack pattern of SM14

2.7.15 Specimen SM15 Test Results

The spandrel member SM15 was tested under the action of combined bending and torsional moments. A moment equal to 74% of the cracking moment of the unretrofitted specimen was first applied and maintained at this level while applying torsion in the next phase. Figure 92 shows the moment-deflection relation for SM15. The maximum applied moment is 3.60 k-in. producing a deflection of 67.1×10^{-3} in. The torque versus angle of twist relation for SM15 is shown in Figure 93. The maximum torsional moment noted was 6.61 k-in. at an angle of rotation of 73.1×10^{-3} rad. The final torsional moment observed was 6.34 k-in. at an angle of twist equal to 79.3×10^{-3} rad. Figure 94 shows the cracking of the specimen at the end of the test. The cracking initiated at the top end in the middle of the flange and extended in an inclined direction towards the tip of the flange marked as 1 in the figure. Upon increasing the load, a similar crack was developed near the midspan marked as 3. Two cracks having similar inclinations were observed on along the depth of the web marked as 5 and 7 in Figure 94. There were no cracks formed in the CFRP elements.

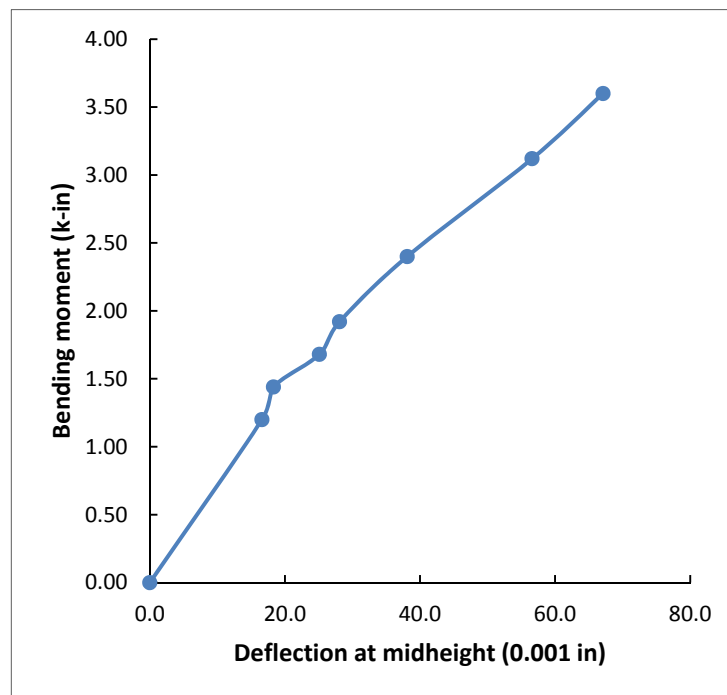


Figure 92. Moment-deflection relation for SM15

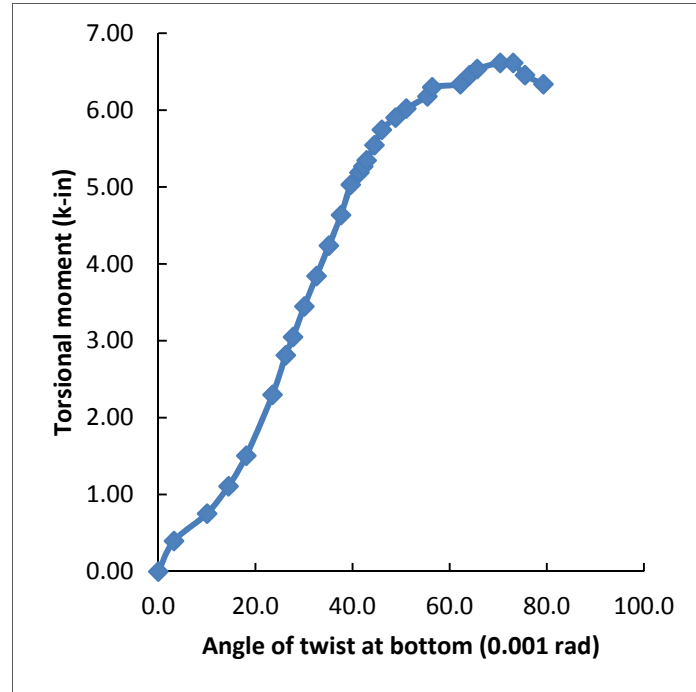


Figure 93. Torque versus angle of twist relation for SM15



Figure 94. Final crack pattern of SM15

2.7.16 Specimen SM16 Test Results

The spandrel member SM16 was tested under the action of combined bending and torsional moments. A moment equal to 74% of the cracking moment of the unretrofitted specimen was first applied and maintained at this level while applying torsion in the next phase. Figure 95 shows the moment-deflection relation for SM16. The maximum applied moment is 3.60 k-in. producing a deflection of 52.5×10^{-3} in. The torque versus angle of twist relation for SM16 is shown in Figure 96. The maximum torsional moment noted was 8.29 k-in. at an angle of rotation of 67.4×10^{-3} rad. The final torsional moment observed was 7.89 k-in. at an angle of twist equal to 72.97×10^{-3} rad. Figure 97 shows the cracking of the specimen at the end of the test. The cracking initiated in the center of the flange near the top end and moved towards the outer edge of the flange in an inclined direction. However the CFRP strip at the edge prevented it from passing through the depth of the flange. At a higher load level, another crack developed across the depth of the flange marked as 3 in Figure 97.

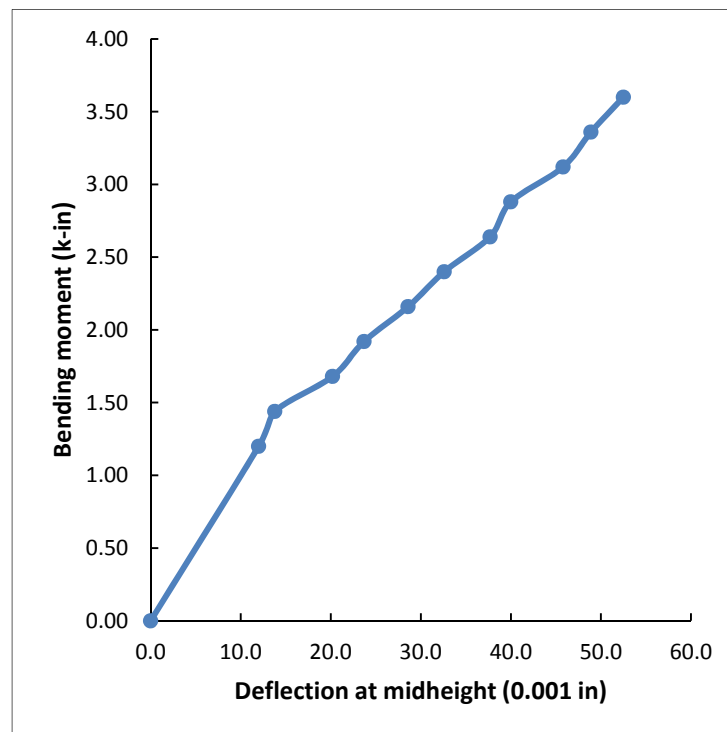


Figure 95. Moment-deflection relation for SM16

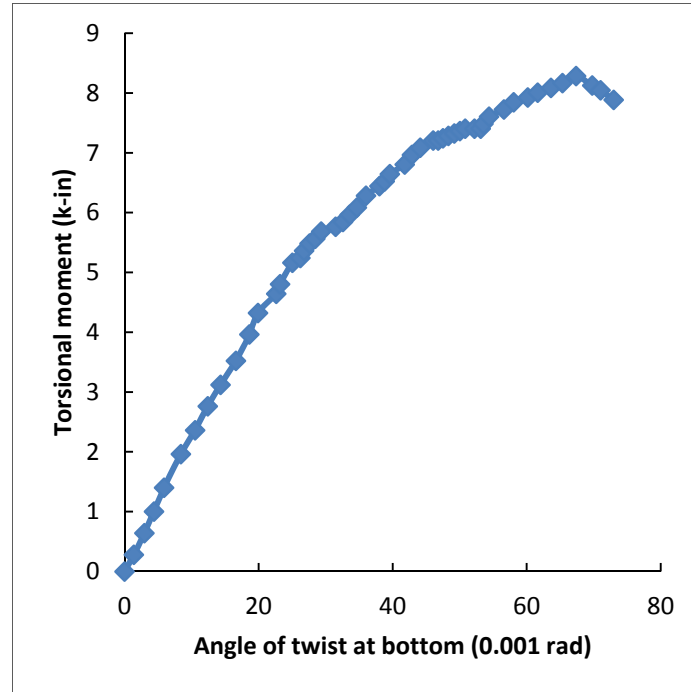


Figure 96. Torque versus angle of twist relation for SM16



Figure 97. Final crack pattern of SM16

2.7.17 Specimen SM17 Test Results

The spandrel member SM17 was tested under torsional moment only. Figure 98 shows the torque versus angle of twist relation for SM17. The maximum torsional moment observed was 4.32 k-in. at a rotation of 51.50×10^{-3} rad. at the bottom. The cracking initiated at the corner of flange and web marked as 1 in Figure 99. It was followed a few more small cracks on the flange outer face and across the depth of the flange. Finally, a big crack developed across the width of the flange marked as 6 in the figure. The torsional moment at this point was 4.24 k-in. at an angle of rotation equal to 55.42×10^{-3} rad.

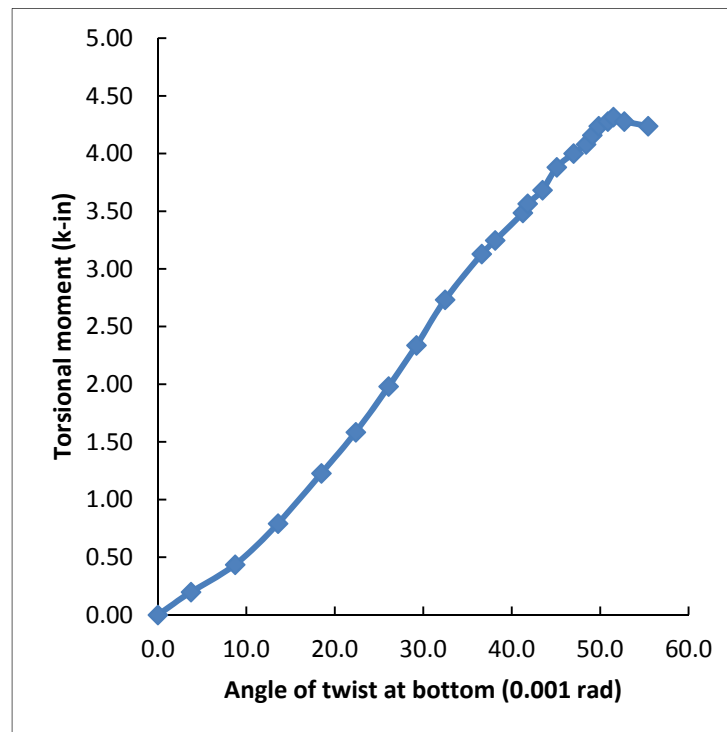


Figure 98. Torque versus angle of twist relation for SM17



Figure 99. Final crack pattern of SM17

2.7.18 Specimen SM18 Test Results

The spandrel member SM18 was tested under bending moment only. Figure 100 shows the moment-deflection relation for SM18. The maximum moment observed was 9.36 k-in. corresponding to a midheight deflection of 230.5×10^{-3} in. The moment at failure was 6.24 k-in. at a midheight deflection of 242.80×10^{-3} in. Figure 101 shows the cracking pattern of SM18 at the end of the test. A few small cracks developed across the width of the web initially as shown in the figure. However, the cracks did not extend across the depth. At a higher load, the top of specimen cracked all across the cross section.

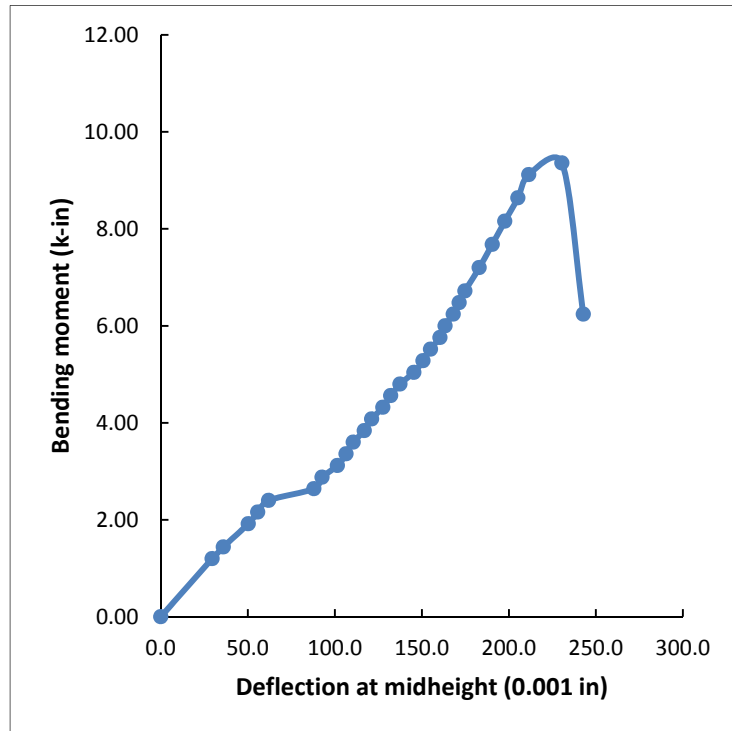


Figure 100. Moment-deflection relation for SM18



Figure 101. Final crack pattern for SM18

2.7.19 Specimen SM19 Test Results

The spandrel member SM19 was tested under both bending and torsional moments. A moment equal to 68% of the cracking moment of the specimen was first applied and maintained at this level while applying torsion in the next phase. Figure 102 shows the moment-deflection relation for SM19. The maximum applied moment is 3.60 k-in. producing a deflection of 112.0×10^{-3} in. The torque versus angle of twist relation for SM19 is shown in Figure 103. The maximum torsional moment noted was 4.67 k-in. at an angle of rotation of 49.8×10^{-3} rad. The final torsional moment observed was 4.44 k-in. at an angle of twist equal to 55.86×10^{-3} rad. Figure 104 shows the cracking of the specimen at the end of the test. Two major cracks were developed at the same load level marked as 1 in the figure. One of the cracks runs in an inclined direction across the width of the flange and extending through the depth of the flange tip. Another crack crossed the depth of the web in a similar inclined fashion.

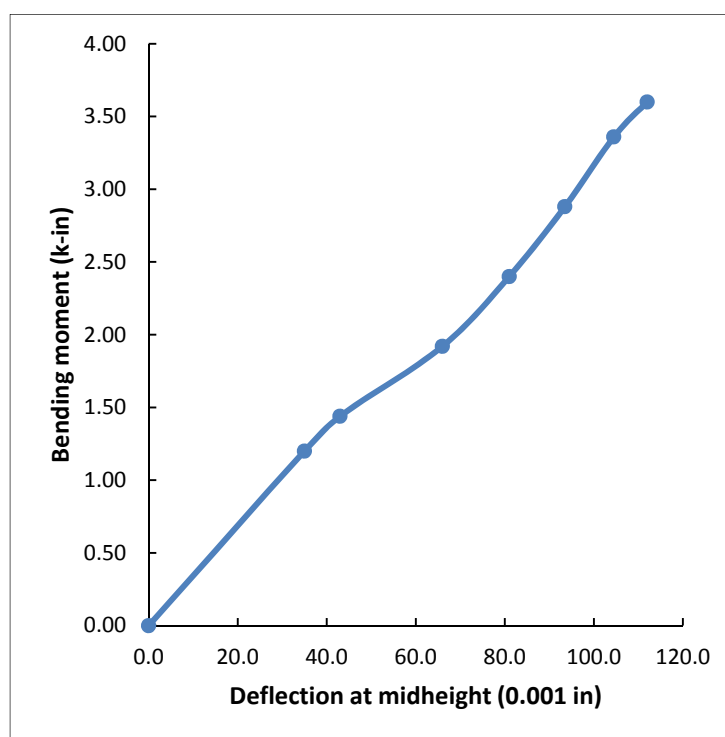


Figure 102. Moment-deflection relation for SM19

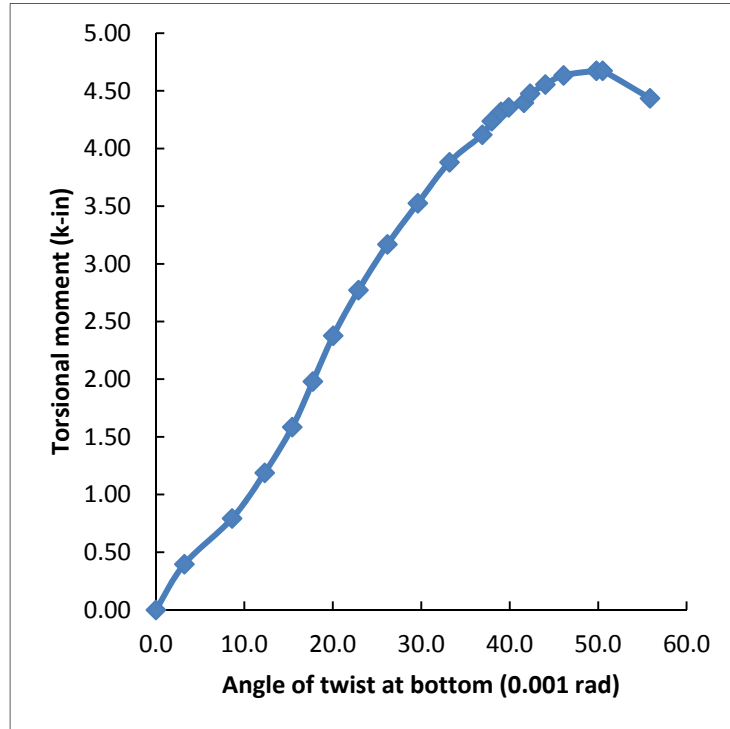


Figure 103. Torque versus angle of twist relation for SM19



Figure 104. Final crack pattern of SM19

2.8 Slab Specimens Test Results

Three slab specimens with spandrel members on all four sides were tested as part of this research study. The following sub sections discuss the test results for these specimens one by one.

2.8.1 Specimen SL01 Test Results

The slab specimen SL01 was tested under a point load applied at the center of the slab as shown in Figure 52. Slab deflection was recorded at the midspan under the point of application of the load. Figure 105 shows load-midspan deflection for the slab. The maximum load was recorded as 27.24 kips. The maximum deflection was recorded as 474×10^{-3} in. corresponding to a load of 24.97 kips.

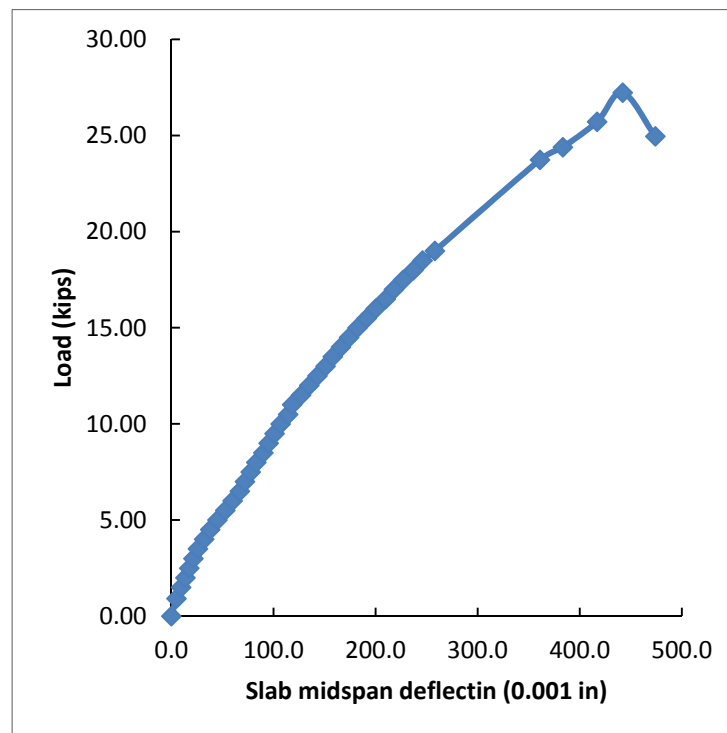


Figure 105. Load-deflection relation for slab of SL01

Deflections of spandrel members were recorded with the help of dial gages and are shown in Figure 106. Spandrel members A and B appear to deflect in a similar fashion while spandrel members C and D have approximately same deflections. The position of these spandrel members in the slab-beam specimen SL01 is shown in Figure 34. The difference in the response of the spandrel members could be due to the difference of the slab moments in two directions caused by the difference in distances from the top to the rebar centers.

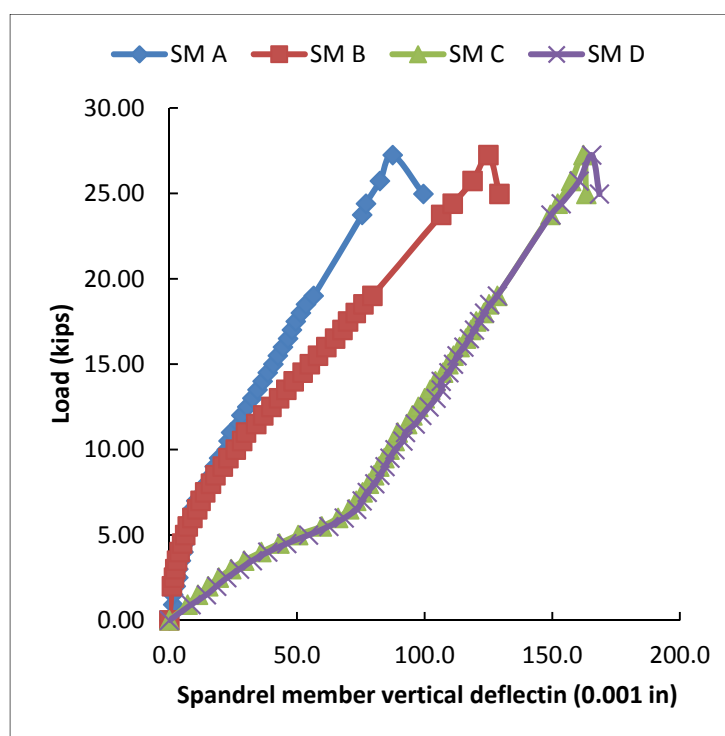


Figure 106. Load-deflection relation for spandrel members of SL01

At load level of 24.5 kips., major cracks were observed at the bottom face of the slab. The cracks appeared to originate at the mid-point, right under the point of application of the load and running diagonally towards the corner of spandrel members A and B in one direction and spandrel members C and D in the opposite direction. These cracks are shown in Figure 107.



Figure 107. Cracks at the bottom surface of slab in SL01

After the formation of initial cracks, the test was conducted in a displacement control fashion. The displacement at the midspan of the slab was used as a reference displacement. At a load level of 25.72 kips., diagonal cracks were observed in spandrel members A and D, marked as 3 in Figure 108.



Figure 108. Cracks in spandrel member of SL01 at a load of 25.72 kip

At a load value of 27.24 kips., major spalling of concrete occurred from the bottom of the slab as shown in Figure 109. The load stopped increasing while the slab mid-span deflection kept increasing. Readings were taken and the test was stopped. The load dropped to a new value of 24.97 kips.



Figure 109. Bottom view of SL01 after test

2.8.2 Specimen SL02 Test Results

The slab specimen SL02 was tested under two point loads applied at one third points along the middle of the slab as shown in Figure 53. The distance between the two concentrated loads was 18 in. Slab deflection was recorded at midpoint by installing a dial gage on the bottom side of the slab. Figure 110 shows load-midspan deflection for the slab. The maximum value of each load was recorded as 17.80 kips, causing a deflection of 254.0×10^{-3} in. The maximum deflection was recorded as 265.2×10^{-3} in. corresponding to a load of 16.85 kips.

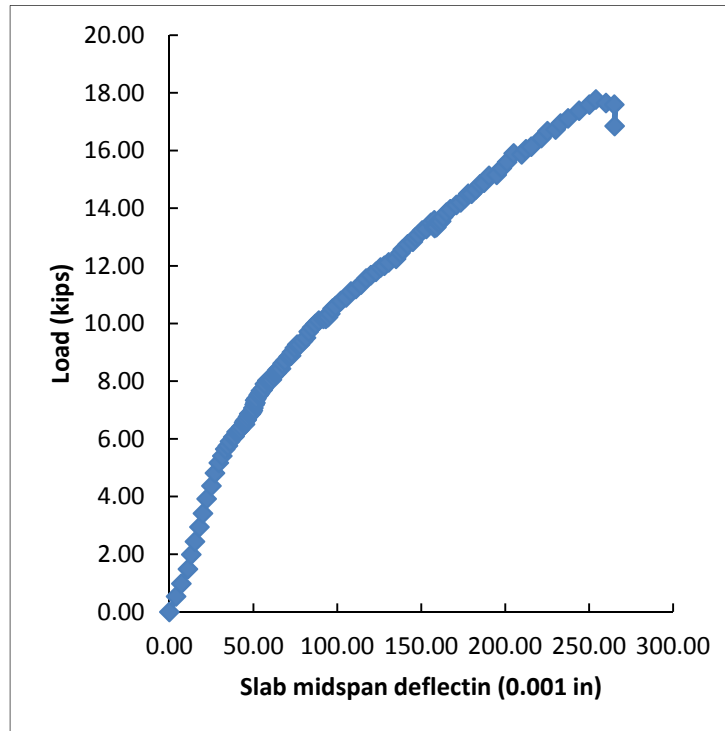


Figure 110. Load-deflection relation for slab of SL02

The vertical deflections of spandrel members were recorded with the help of dial gauges and are shown in Figure 111. Spandrel members B and D were closer to the loads and experienced higher deflections as compared to spandrel members A and C which were located away from the loads as shown in the figure. The positions of the spandrel members in the slab-beam specimen SL02 are shown in Figure 38. The maximum deflection was recorded in spandrel member B as 147.60×10^{-3} in.

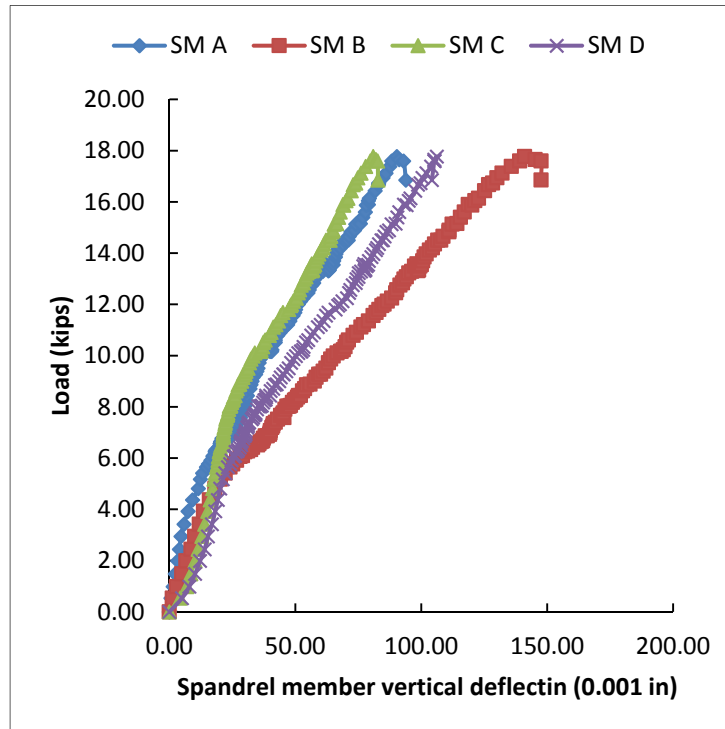


Figure 111. Load-deflection relation for spandrel members of SL02

The cracking pattern of the slab at the end of the test is shown in Figure 112. The cracks run parallel to the edge between the points of application of the loads and then extend towards the corners in an inclined direction.

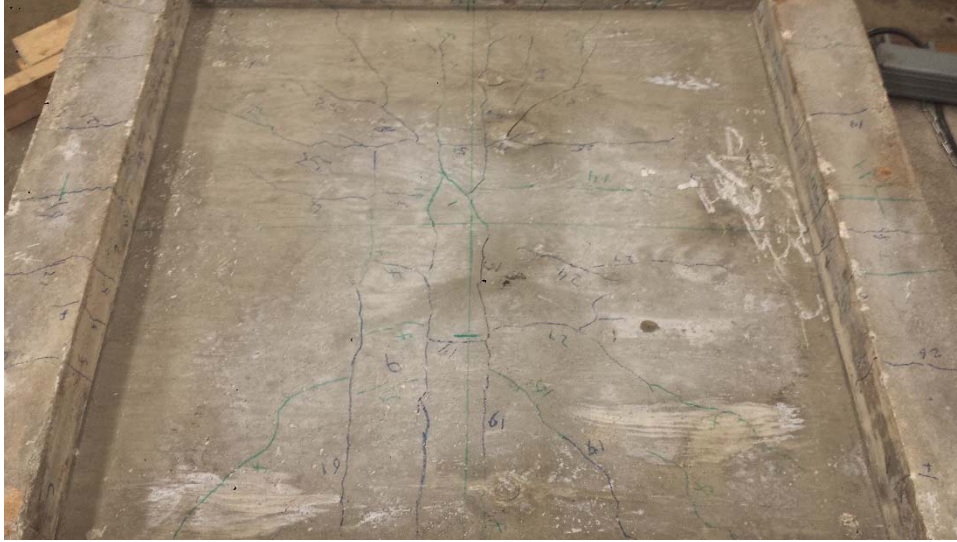


Figure 112. Bottom view of SL02 after test

The cracking pattern of typical spandrel member is shown in Figure 113. The cracks are normal to the axis of the member near the middle and becomes more and more inclined toward the corners.



Figure 113. Final cracking pattern in typical spandrel member of SL02

2.8.3 Specimen SL03 Test Results

The slab specimen SL03 was tested under two point loads applied at 5.5 inches from the outer edges of the slab as shown in Figure 54. The distance between the two point loads was 43 in. Slab deflection was recorded at midpoint by installing a dial gage on the bottom side of the slab. Figure 114 shows load-midspan deflection for the slab. The maximum value of load was recorded as 21.77 kips, causing a deflection of 254.0×10^{-3} in. The maximum deflection was recorded as 233.60×10^{-3} in.

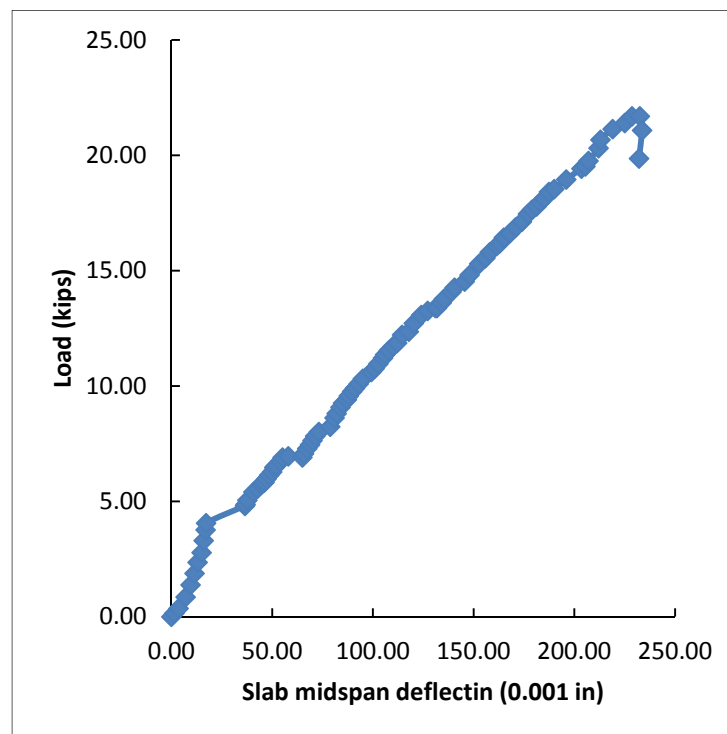


Figure 114. Load-deflection for slab of SL03

The vertical deflections of spandrel members closer to the load points were recorded with the help of dial gauges and are shown in Figure 115 and Figure 116. Spandrel member B (SMB) deflection is plotted against load P1 which was located closer to it. Similarly spandrel member D

(SMD) deflection is plotted against load P2 which was closer to it. The position of these spandrel members in slab-beam specimen SL03 is shown in Figure 38.

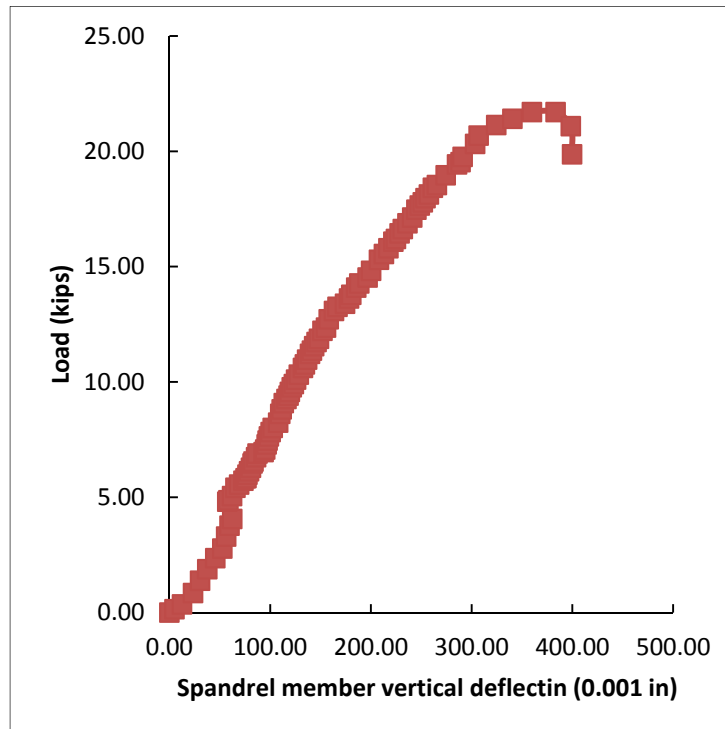


Figure 115. Load-deflection relation of SMB in SL03

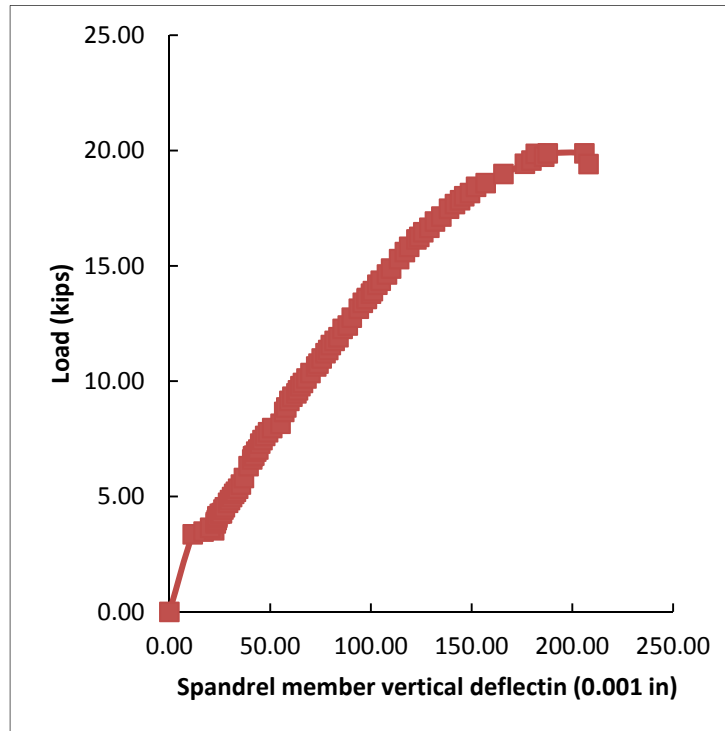


Figure 116. Load-deflection relation of SMD in SL03

The cracking pattern of the slab at the end of the test is shown in Figure 117. The cracks started closer to the spandrel members where loads are applied and extended gradually towards the middle of the slab. The cracks eventually met in the middle and formed continuous lines of cracks from one spandrel member to the opposite spandrel member.



Figure 117. Bottom view of SL03 after test

The cracking pattern of spandrel members closer to the loads is shown in Figure 118 and Figure 119. The cracks are mostly formed in the middle one third of the members and are perpendicular to the axis of the members indicating primarily a bending type failure.



Figure 118. Final crack pattern of SMB in SL03



Figure 119. Final crack pattern of SMD in SL03

2.9 Comparison and Discussion

In SM14, the two strips at the corner prevented the stress concentration and prevented the premature crack at that location. The specimen failed in a brittle fashion once the peak load was reached with a big crack on the front face.

The summary of test results for spandrel members is given in Table 4. In this table, M_{\max} is the maximum applied bending moment, T_{\max} is the maximum applied torsional moment, D_{\max} is the deflection at midheight of the member corresponding to maximum bending moment, and Θ_{\max} is the angle of twist at the bottom of the specimen corresponding to maximum applied torsion.

Table 4. Summary of test results for spandrel members

Specimen	M_{max} (k-in.)	D_{max} (0.001 in.)	T_{max} (k-in.)	Θ_{max} (0.001 rad.)
SS01	4.08	95.9	9.11	63.77
SS02	3.12	83.1	9.90	89.6
SS03	6.00	116.0	13.82	104.3
SM04	-	-	3.32	26.1
SM05	-	-	4.99	30.8
SM06	-	-	-	-
SM07	3.84	31.0	5.15	27.7
SM08	-	-	5.15	40.67
SM09	7.20	293.5	-	-
SM10	2.40	55.8	5.43	39.7
SM11	-	-	4.83	40.4
SM12	2.64	44.3	5.12	25.4
SM13	7.20	144.2	4.40	43.8
SM14	-	-	5.23	45.1
SM15	3.60	67.1	6.61	73.1
SM16	3.60	52.5	7.89	72.9
SM17	-	-	4.32	51.5
SM18	9.36	230.5	-	-
SM19	3.60	112.0	4.67	49.8

3. THEORETICAL ANALYSIS

3.1 Introduction

This chapter presents the theoretical analysis part of the study. Material nonlinear bending and torsional analysis procedures are formulated at the cross-sectional and member levels.

3.2 Bending Strength Analysis

This section describes the cross-sectional bending analysis of all specimens. Both crack initiation and ultimate bending strength analyses are formulated for sections of isolated members.

3.2.1 Uncracked Section Analysis

Transformed area method is utilized for cross-sectional analysis including CFRP retrofitting under unsymmetrical bending in the elastic range. Figure 120 shows a typical cross section along with general non-principal coordinate axes, x and y . Let β be the angle which the neutral axis makes with the horizontal x -axis, as shown in Figure 120.

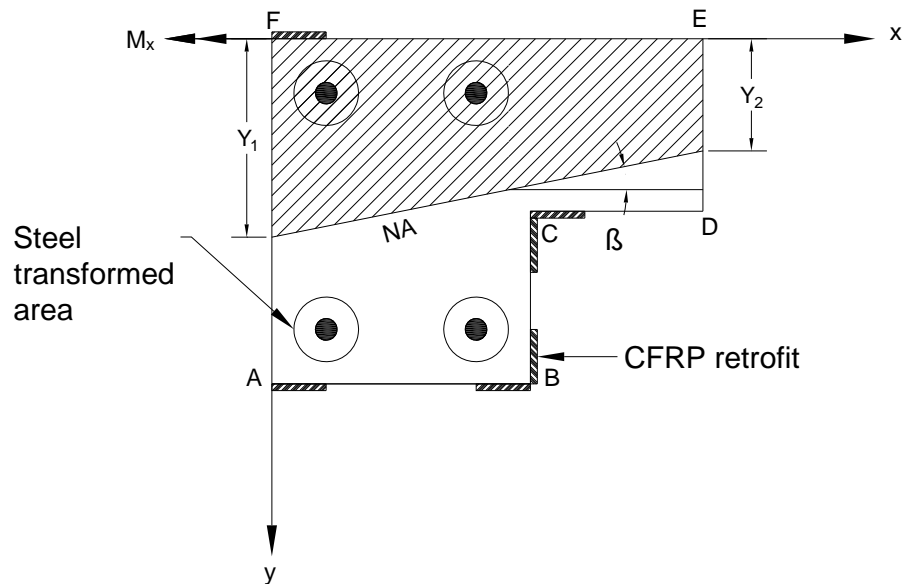


Figure 120. Typical cross section for transformed area method

The axial stress, σ_z , due to a moment having components M_x and M_y about x and y axes, respectively, is given [29]:

$$\sigma_z = - \left[\frac{M_y I_x + M_x I_{xy}}{I_x I_y - I_{xy}^2} \right] x + \left[\frac{M_x I_y + M_y I_{xy}}{I_x I_y - I_{xy}^2} \right] y \quad (6)$$

where I_x is the moment of inertia about x-axis, I_y is the moment of inertia about y-axis, and I_{xy} is the product of inertia about these axes. In this study, the spandrel members are subjected to moments only about the x-axis. Therefore, Equation 7 simplifies to:

$$\sigma_z = - \left[\frac{M_x I_{xy}}{I_x I_y - I_{xy}^2} \right] x + \left[\frac{M_x I_y}{I_x I_y - I_{xy}^2} \right] y \quad (7)$$

Cracking starts on the tension side of cross section when the normal tensile stress in concrete reaches modulus of rupture of concrete. Therefore, the bending moment causing initiation of cracking, M_{xcr} , is given by:

$$M_{xcr} = \frac{f_r (I_x I_y - I_{xy}^2)}{I_y y - I_{xy} x} \quad (8)$$

where f_r is the modulus of rupture of concrete equal to $7.5\sqrt{f'_c}$ according to ACI 318-14 [30]. The angle of inclination of the neutral axis is obtained by setting the normal stress σ_z equal to zero in Equation 7 resulting in:

$$\tan\beta = \frac{I_{xy}}{I_y} \quad (9)$$

Therefore, under the action of unsymmetrical bending, the neutral axis orientation depends only on the geometry of the cross section before cracking. Once the cross section is cracked, the orientation of the neutral axis changes with an increase in M_x . Since I_{xy} for the unsymmetrical cross section is not zero, the neutral axis is inclined.

Table 5 summarizes the results of uncracked section analysis for all square section and L-shaped specimens using the transformed area method. The location of the neutral axis is completely determined by distances Y_1 and Y_2 and angle β as shown in Figure 120. The values given in the table indicate that the neutral axis for L-shaped specimens is inclined.

The crack initiation location and M_{xcr} values are also given in Table 5. It is worth mentioning that cracking starts at the bottom right corner of the L-shaped sections, that is, at location B as shown in Figure 120. The four steel rebars in SS02 and SS03 increase the value of M_{xcr} by 10% as compared to the similar plain concrete section SS01. Similarly, M_{xcr} value of the plain concrete L-shaped section SM04 increases by 15% in specimens SM05 through SM07 having four longitudinal rebars.

The additional rebar in the flange of SM08 through SM10 has negligible impact on the cracking capacity because it is located very close to the neutral axis. The difference in cracking moment of specimens SM08 through SM10 and specimens SM11 through SM13 is caused by the difference in their compressive strengths of concrete since both sets of specimens have similar longitudinal reinforcements. The introduction of two CFRP strips in SM14 at the corner of the flange and web caused only 2.2 percent increase in the cracking moment because of their proximity with the neutral axis. The cracking moment is increased by 30 percent in case of SM15 and SM16 with the application of additional CFRP strips.

Table 5. Results of uncracked section analysis

Specimen	b (deg.)	Y₁ (in.)	Y₂ (in.)	Crack Location	M_{xcr} (k-in.)
SS01	0.00	2.50	2.50	-	11.44
SS02- SS03	0.00	2.50	2.50	-	12.53
SM04	14.46	2.30	1.01	B	4.23
SM05—SM07	14.10	2.29	1.04	B	4.88
SM08—SM10	14.14	2.29	1.03	B	4.92
SM11—SM13	14.18	2.29	1.03	B	5.05
SM14	13.57	2.29	1.08	B	4.99
SM15	11.70	2.30	1.27	B	6.34
SM16	12.07	2.27	1.21	B	6.36
SM17—SM19	13.12	2.31	1.15	B	5.25

3.2.2 Ultimate Strength Analysis

In the materially nonlinear range, the orientation of the neutral axis depends not only on the magnitude of M_x , geometric properties of the cross section, and the amount of reinforcement but also on the mechanical properties of concrete, steel, and CFRP. For any combination of these characteristics, a total of eleven ultimate stress patterns is possible based on the orientation and location of the neutral axis [31]. However, based on the size and geometry of the cross sections used in this dissertation, only two of the eleven ultimate stress patterns were found to be applicable. These two patterns are shown in Figure 121 and Figure 122.

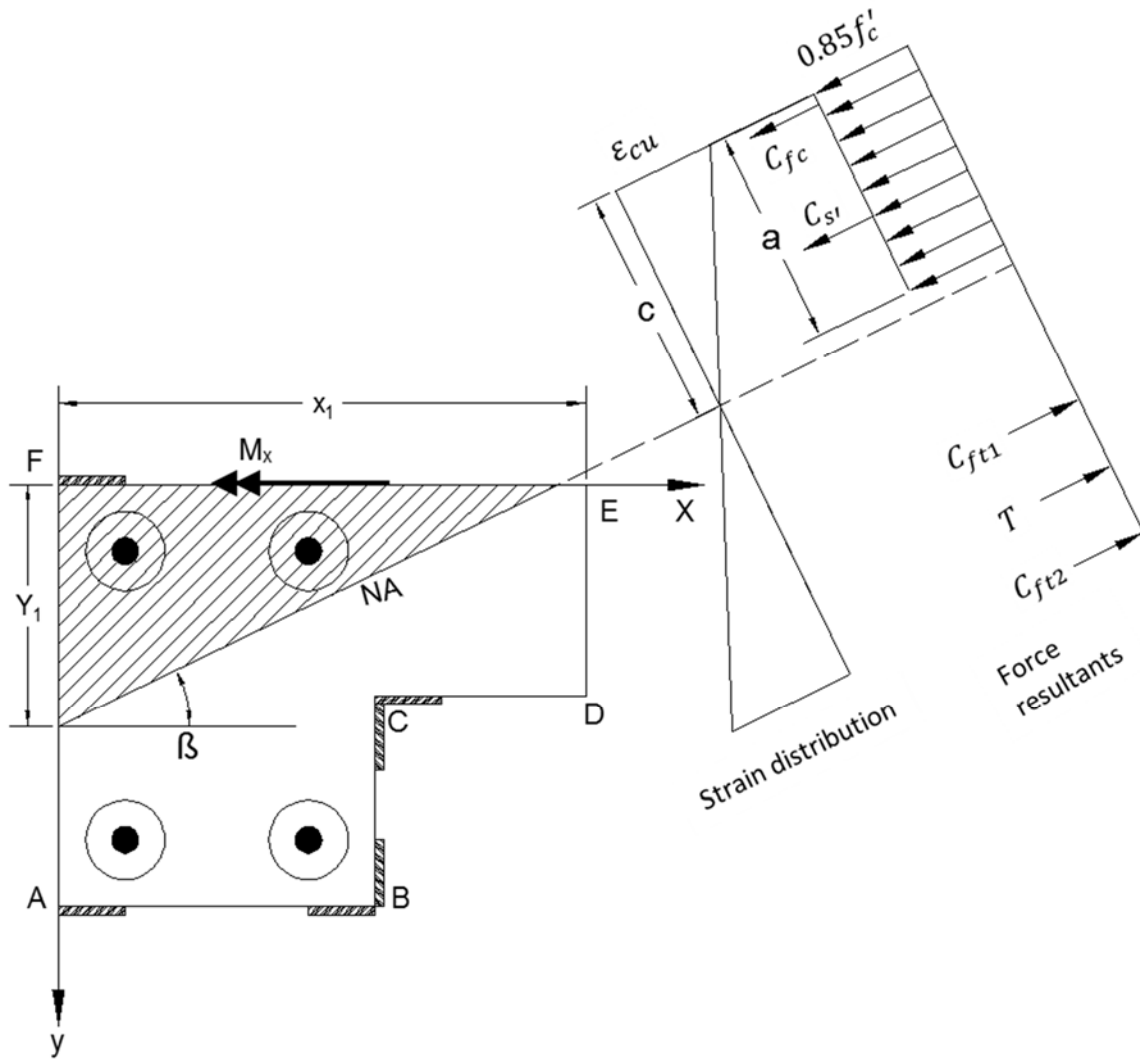


Figure 121. Pattern 1 for ultimate strength analysis

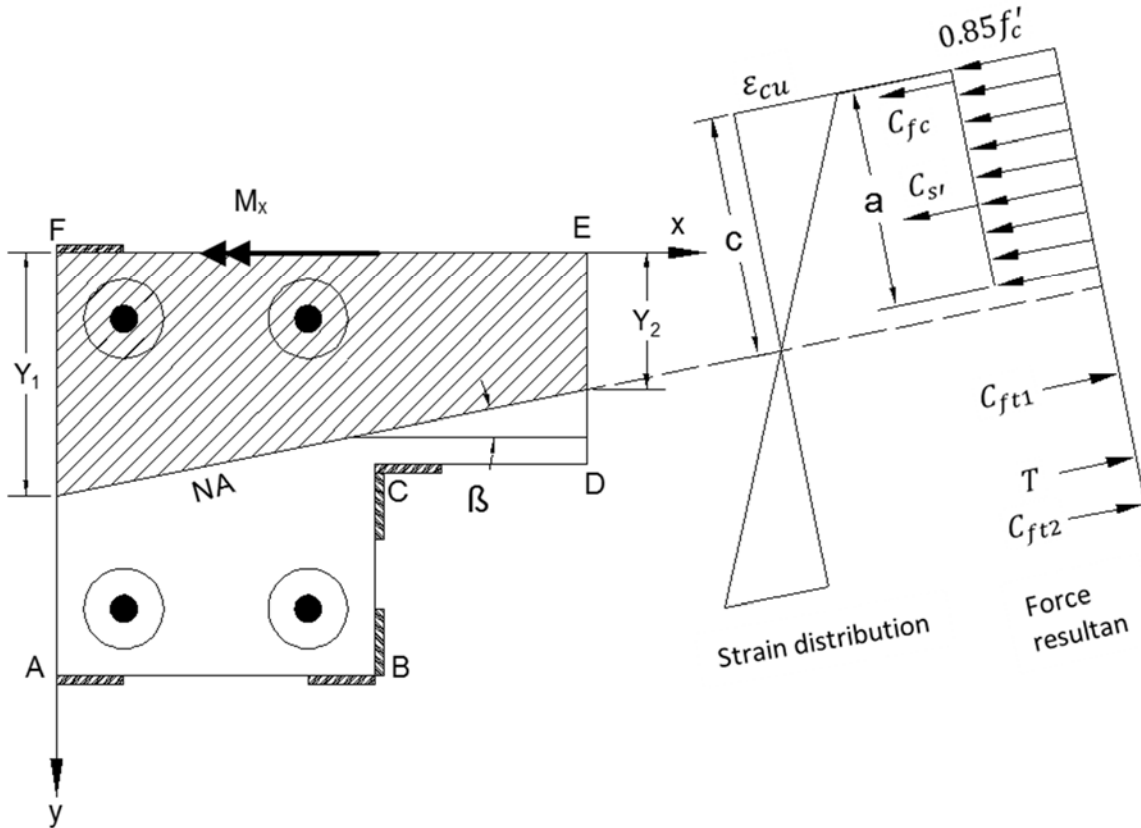


Figure 122. Pattern 2 for ultimate strength analysis

The ultimate strain of concrete ϵ_{cu} occur at point F in Figure 121 and Figure 122, therefore the strain in each reinforcing element is given as:

$$\epsilon_i = \epsilon_{cu} \left[1 - \frac{x_i}{x_1} - \frac{y_i}{y_1} \right] \quad (10)$$

where (x_i, y_i) are coordinates of the i^{th} element, x_1 is the x intercept of neutral axis, and y_1 is the y intercept of neutral axis. This equation can be used for both steel rebars and CFRP elements. Once the strain in an element is known, the stress is determined using stress strain relationship of the corresponding material. Knowing the concrete compression block and forces in each reinforcing element, total axial force and bending moments can be determined readily by satisfying equilibrium conditions. The axial force equilibrium for pattern 1 shown in Figure 121 can be expressed as:

$$P = 0.85f'_c \left[\frac{1}{2} \beta_1^2 x_1 y_1 \right] + \sum_{i=1}^n f_{si} A_{bi} + \sum_{i=1}^m f_{fi} A_{fi} \quad (11)$$

where β_1 is the ACI coefficient which depends on compressive strength of concrete. The first term on the right hand side is the total compressive force in concrete. The second term is the summation of forces in steel rebars where A_{bi} is the area and f_{si} is the stress in i^{th} steel rebar. The last term on the right hand side is the summation of forces in CFRP elements where A_{fi} is the area and f_{fi} is the stress in i^{th} CFRP element. The bending moment equilibrium about x axis in Figure 121 results in:

$$M_x = 0.85f'_c \left[\frac{1}{2} \beta_1^2 x_1 y_1 \right] \bar{y} + \sum_{i=1}^n f_{si} A_{si} y_{si} + \sum_{i=1}^m f_{fi} A_{fi} y_{fi} \quad (12)$$

where \bar{y} is the y centroidal coordinate of the concrete compression area, y_{si} is the distance of i^{th} steel rebar along y axis from origin, and y_{fi} is the distance of the i^{th} CFRP element along y axis from origin. Finally, the bending moment equilibrium about y axis in Figure 121 gives:

$$M_y = 0.85f'_c \left[\frac{1}{2} \beta_1^2 x_1 y_1 \right] \bar{x} + \sum_{i=1}^n f_{si} A_{si} x_{si} + \sum_{i=1}^m f_{fi} A_{fi} x_{fi} \quad (13)$$

where \bar{x} is the x centroidal coordinate of the concrete compression area, x_{si} is the distance of i^{th} steel rebar along x axis from origin, and x_{fi} is the distance of the i^{th} CFRP element along x axis from origin. Similarly, the P , M_x , and M_y equilibrium equations for the pattern 2 shown in Figure 122 are:

$$P = 0.85f'_c \left[\beta_1 b_f y_2 + \frac{1}{2} \beta_1 b_f (y_1 - y_2) \right] + \sum_{i=1}^n f_{si} A_{bi} + \sum_{i=1}^m f_{fi} A_{fi} \quad (14)$$

$$M_x = 0.85f'_c \left[\beta_1 b_f y_2 + \frac{1}{2} \beta_1 b_f (y_1 - y_2) \right] \bar{y} + \sum_{i=1}^n f_{si} A_{si} y_{si} + \sum_{i=1}^m f_{fi} A_{fi} y_{fi} \quad (15)$$

$$M_y = 0.85f'_c \left[\beta_1 b_f y_2 + \frac{1}{2} \beta_1 b_f (y_1 - y_2) \right] \bar{x} + \sum_{i=1}^n f_{si} A_{si} x_{si} + \sum_{i=1}^m f_{fi} A_{fi} x_{fi} \quad (16)$$

An iterative procedure is used to determine the correct location and orientation of neutral axis by satisfying equilibrium conditions. An initial value of y_1 is assumed as 0.001, which is then incremented with 0.001 in each cycle. Similarly, the value of angle β starts with a value of 0.01° and incremented by 0.01° in each cycle. This process is continued until equilibrium conditions are satisfied. A MATLAB program is compiled to determine ultimate strength of each specimen using this process and is given in Appendix B.

Table 6 shows results of ultimate strength analysis. The method is not applicable to plain concrete specimens, namely SS01 and SM04. It was also found that the neutral axis for SM14 with two CFRP strips is horizontal so this method cannot be used. Pattern 2 governs the rest of the specimens as indicated by the nonzero values of y_2 . A comparison with the uncracked section analysis shows that the neutral axis tend towards horizontal at higher loads. The additional rebar in the flange caused about 15% increase in the ultimate bending capacity. The bending capacity is increased six times with the introduction of CFRP strips in case of specimens SM15 and SM16. The increase is almost identical even though SM15 has only six CFRP elements as compared to the nine elements of SM16. The CFRP elements in SM15 are stressed to higher values so they contribute more to the bending capacity. A significant increase is also noted in the case of specimens SM17-SM19 having four CFRP strips.

Table 6. Results of ultimate bending strength analysis

Specimen	b (deg.)	Y₁ (in.)	Y₂ (in.)	Φ_{xu} (rad./in.)	M_{xu} (k-in.)
SS01	NA	NA	NA	NA	NA
SS02-SS03	0	0.46	0.46	0.0087	23.75
SM04	NA	NA	NA	NA	NA
SM05—SM07	6.14	0.69	0.15	0.0058	17.42
SM08—SM10	2.38	0.60	0.39	0.0059	20.06
SM11—SM13	2.57	0.59	0.37	0.0069	20.34
SM14	NA	NA	NA	NA	NA
SM15	0.70	1.31	1.25	0.0030	105.38
SM16	4.26	1.44	1.07	0.0028	105.60
SM17—SM19	7.50	1.27	0.61	0.0026	56.76

3.3 Nonlinear Moment-Curvature Relations

The numerical procedure of tangent stiffness method [32] is adopted to determine the complete moment-curvature relations for the specimens. The method is an iterative procedure which can be used for any geometric cross section and any distribution of reinforcing elements. Although, in the laboratory tests of specimens, the spandrel members are only subjected to moment about x-axis, the numerical analysis also considers axial load and moment about y-axis, as shown in Figure 123, for broader application and to satisfy all three equilibrium conditions.

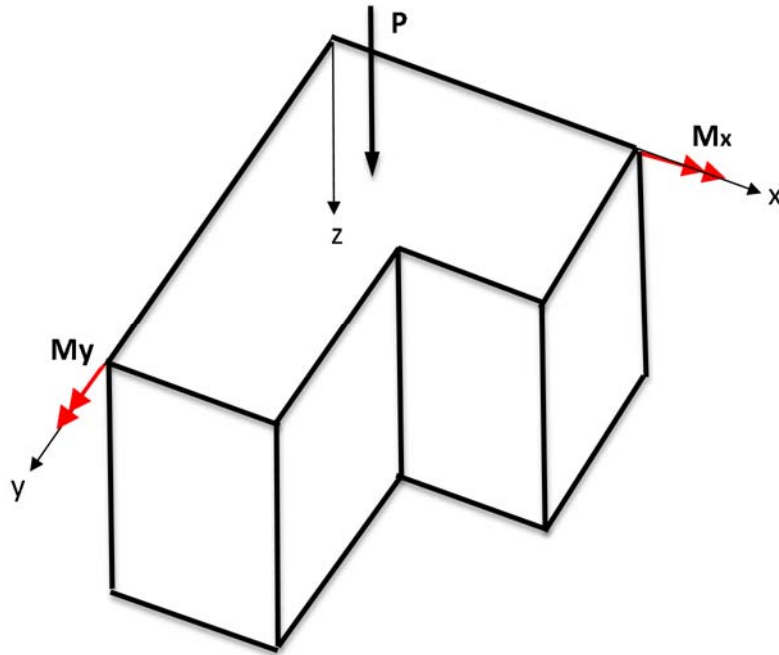


Figure 123. Member segment schematic under biaxial bending

3.3.1 Formulation of Equations

The normal strain ε at any point (x, y) of the cross section subjected to bending moments M_x and M_y about x and y axes is expressed as:

$$\varepsilon = \varepsilon_o + y\varphi_x - x\varphi_y \quad (17)$$

in which ε_o is the axial strain at origin whereas φ_x and φ_y are the bending curvatures about x and y axes. The cross sectional equilibrium equations for axial force and bending moments about x and y axes can be represented as:

$$P = \int \sigma dA \quad (18)$$

$$M_x = \int \sigma y dA \quad (19)$$

$$M_y = - \int \sigma x dA \quad (20)$$

In order to numerically evaluate the integrals, the concrete area is divided into small rectangular area elements by passing horizontal and vertical grid lines, as shown in Figure 124. Each steel rebar and CFRP strip is considered a separate element.

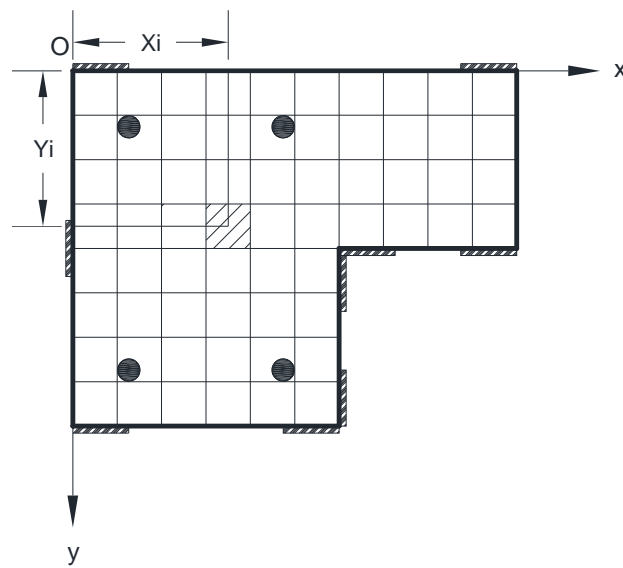


Figure 124. Partitioning of the cross section

For the cross section of a retrofitted reinforced concrete spandrel member, the integrals are calculated by taking summation over the areas of the constituent materials, namely concrete, steel rebars, and CFRP strips. Therefore Equations 18 through 20 take the following forms:

$$P = \sum_{i=1}^{N_c} \sigma_{ci} dA_c + \sum_{j=1}^{N_s} \sigma_{sj} dA_s + \sum_{k=1}^{N_f} \sigma_{fk} dA_f \quad (21)$$

$$M_x = \sum_{i=1}^{N_c} \sigma_{ci} y_i dA_c + \sum_{j=1}^{N_s} \sigma_{sj} y_j dA_s + \sum_{k=1}^{N_f} \sigma_{fk} y_k dA_f \quad (22)$$

$$M_y = - \sum_{i=1}^{N_c} \sigma_{ci} x_i dA_c - \sum_{j=1}^{N_s} \sigma_{sj} x_j dA_s - \sum_{k=1}^{N_f} \sigma_{fk} x_k dA_f \quad (23)$$

where N_c is the total number of concrete elements, N_s is the number of rebars, and N_f is the number of CFRP strips. The inelastic behavior is path dependent and requires step-by-step calculations following the load history. Therefore, the applied moments are increased in the form of small increments so that the relationship between load vector and displacement vector can be considered as linear. Therefore, the incremental forms of the equilibrium equations are given as:

$$\dot{P} = \sum_{i=1}^{N_c} \dot{\sigma}_{ci} dA_c + \sum_{j=1}^{N_s} \dot{\sigma}_{sj} dA_s + \sum_{k=1}^{N_f} \dot{\sigma}_{fk} dA_f \quad (24)$$

$$\dot{M}_x = \sum_{i=1}^{N_c} \dot{\sigma}_{ci} y_i dA_c + \sum_{j=1}^{N_s} \dot{\sigma}_{sj} y_j dA_s + \sum_{k=1}^{N_f} \dot{\sigma}_{fk} y_k dA_f \quad (25)$$

$$\dot{M}_y = - \sum_{i=1}^{N_c} \dot{\sigma}_{ci} x_i dA_c - \sum_{j=1}^{N_s} \dot{\sigma}_{sj} x_j dA_s - \sum_{k=1}^{N_f} \dot{\sigma}_{fk} x_k dA_f \quad (26)$$

where the dot on top of an action represents a small change. The change in stress is equal to the tangent modulus multiplied by change in strain. Therefore Equations 24 through 26 can be written as:

$$\dot{P} = \sum_{i=1}^{N_c} E_{ct} \dot{\epsilon}_{ci} dA_c + \sum_{j=1}^{N_s} E_{st} \dot{\epsilon}_{sj} dA_s + \sum_{k=1}^{N_f} E_{ft} \dot{\epsilon}_{fk} dA_f \quad (27)$$

$$\dot{M}_x = \sum_{i=1}^{N_c} E_{ct} \dot{\epsilon}_{ci} y_i dA_c + \sum_{j=1}^{N_s} E_{st} \dot{\epsilon}_{sj} y_j dA_s + \sum_{k=1}^{N_f} E_{ft} \dot{\epsilon}_{fk} y_k dA_f \quad (28)$$

$$\dot{M}_y = - \sum_{i=1}^{N_c} E_{ct} \dot{\epsilon}_{ci} x_i dA_c - \sum_{j=1}^{N_s} E_{st} \dot{\epsilon}_{sj} x_j dA_s - \sum_{k=1}^{N_f} E_{ft} \dot{\epsilon}_{fk} x_k dA_f \quad (29)$$

Tangent modulus for each material is calculated using Equations 1-5. The increment in strain can be determined by writing Equation 17 in the following form:

$$\dot{\varepsilon} = \dot{\varepsilon}_o + y\dot{\varphi}_x - x\dot{\varphi}_y \quad (30)$$

Substituting Equation 30 into Equations 27 through 29:

$$\begin{aligned} \dot{P} = & \sum_{i=1}^{N_c} E_{ct} [\dot{\varepsilon}_o + y\dot{\varphi}_x - x\dot{\varphi}_y] dA_c + \sum_{j=1}^{N_s} E_{st} [\dot{\varepsilon}_o + y\dot{\varphi}_x - x\dot{\varphi}_y] dA_s \\ & + \sum_{k=1}^{N_f} E_{ft} [\dot{\varepsilon}_o + y\dot{\varphi}_x - x\dot{\varphi}_y] dA_f \end{aligned} \quad (31)$$

$$\begin{aligned} \dot{M}_x = & \sum_{i=1}^{N_c} E_{ct} [\dot{\varepsilon}_o + y\dot{\varphi}_x - x\dot{\varphi}_y] y_i dA_c + \sum_{j=1}^{N_s} E_{st} [\dot{\varepsilon}_o + y\dot{\varphi}_x - x\dot{\varphi}_y] y_j dA_s \\ & + \sum_{k=1}^{N_f} E_{ft} [\dot{\varepsilon}_o + y\dot{\varphi}_x - x\dot{\varphi}_y] y_k dA_f \end{aligned} \quad (32)$$

$$\begin{aligned} \dot{M}_y = & - \sum_{i=1}^{N_c} E_{ct} [\dot{\varepsilon}_o + y\dot{\varphi}_x - x\dot{\varphi}_y] x_i dA_c - \sum_{j=1}^{N_s} E_{st} [\dot{\varepsilon}_o + y\dot{\varphi}_x - x\dot{\varphi}_y] x_j dA_s \\ & - \sum_{k=1}^{N_f} E_{ft} [\dot{\varepsilon}_o + y\dot{\varphi}_x - x\dot{\varphi}_y] x_k dA_f \end{aligned} \quad (33)$$

Rearranging the terms, these three equations can be written as:

$$\begin{aligned}
\dot{P} = & \left[\sum_{i=1}^{N_c} E_{ct} dA_c + \sum_{j=1}^{N_s} E_{st} dA_s + \sum_{k=1}^{N_f} E_{ft} dA_f \right] \dot{\epsilon}_o \\
& + \left[\sum_{i=1}^{N_c} E_{ct} y_i dA_c + \sum_{j=1}^{N_s} E_{st} y_j dA_s + \sum_{k=1}^{N_f} E_{ft} y_k dA_f \right] \dot{\phi}_x \\
& - \left[\sum_{i=1}^{N_c} E_{ct} x_i dA_c + \sum_{j=1}^{N_s} E_{st} x_j dA_s + \sum_{k=1}^{N_f} E_{ft} x_k dA_f \right] \dot{\phi}_y
\end{aligned} \tag{34}$$

$$\begin{aligned}
\dot{M}_x = & \left[\sum_{i=1}^{N_c} E_{ct} y_i dA_c + \sum_{j=1}^{N_s} E_{st} y_j dA_s + \sum_{k=1}^{N_f} E_{ft} y_k dA_f \right] \dot{\epsilon}_o \\
& + \left[\sum_{i=1}^{N_c} E_{ct} y_i^2 dA_c + \sum_{j=1}^{N_s} E_{st} y_j^2 dA_s + \sum_{k=1}^{N_f} E_{ft} y_k^2 dA_f \right] \dot{\phi}_x \\
& - \left[\sum_{i=1}^{N_c} E_{ct} x_i y_i dA_c + \sum_{j=1}^{N_s} E_{st} x_j y_j dA_s + \sum_{k=1}^{N_f} E_{ft} x_k y_k dA_f \right] \dot{\phi}_y
\end{aligned} \tag{35}$$

$$\begin{aligned}
\dot{M}_y = & - \left[\sum_{i=1}^{N_c} E_{ct} x_i dA_c + \sum_{j=1}^{N_s} E_{st} x_j dA_s + \sum_{k=1}^{N_f} E_{ft} x_k dA_f \right] \dot{\epsilon}_o \\
& - \left[\sum_{i=1}^{N_c} E_{ct} x_i y_i dA_c + \sum_{j=1}^{N_s} E_{st} x_j y_j dA_s + \sum_{k=1}^{N_f} E_{ft} x_k y_k dA_f \right] \dot{\phi}_x \\
& + \left[\sum_{i=1}^{N_c} E_{ct} x_i^2 dA_c + \sum_{j=1}^{N_s} E_{st} x_j^2 dA_s + \sum_{k=1}^{N_f} E_{ft} x_k^2 dA_f \right] \dot{\phi}_y
\end{aligned} \tag{36}$$

These equations can be expressed in matrix form as:

$$\begin{Bmatrix} \dot{P} \\ \dot{M}_x \\ \dot{M}_y \end{Bmatrix} = \begin{bmatrix} k_{11} & k_{12} & k_{13} \\ k_{21} & k_{22} & k_{23} \\ k_{31} & k_{32} & k_{33} \end{bmatrix} \begin{Bmatrix} \dot{P} \\ \dot{\phi}_x \\ \dot{\phi}_y \end{Bmatrix} \tag{37}$$

where the coefficients of the tangent stiffness matrix are given as:

$$k_{11} = \left[\sum_{i=1}^{N_c} E_{ct} dA_c + \sum_{j=1}^{N_s} E_{st} dA_s + \sum_{k=1}^{N_f} E_{ft} dA_f \right] \quad (38)$$

$$k_{12} = k_{21} = \left[\sum_{i=1}^{N_c} E_{ct} y_i dA_c + \sum_{j=1}^{N_s} E_{st} y_j dA_s + \sum_{k=1}^{N_f} E_{ft} y_k dA_f \right] \quad (39)$$

$$k_{13} = k_{31} = - \left[\sum_{i=1}^{N_c} E_{ct} x_i dA_c + \sum_{j=1}^{N_s} E_{st} x_j dA_s + \sum_{k=1}^{N_f} E_{ft} x_k dA_f \right] \quad (40)$$

$$k_{22} = \left[\sum_{i=1}^{N_c} E_{ct} y_i^2 dA_c + \sum_{j=1}^{N_s} E_{st} y_j^2 dA_s + \sum_{k=1}^{N_f} E_{ft} y_k^2 dA_f \right] \quad (41)$$

$$k_{23} = k_{32} = - \left[\sum_{i=1}^{N_c} E_{ct} x_i y_i dA_c + \sum_{j=1}^{N_s} E_{st} x_j y_j dA_s + \sum_{k=1}^{N_f} E_{ft} x_k y_k dA_f \right] \quad (42)$$

$$k_{33} = \left[\sum_{i=1}^{N_c} E_{ct} x_i^2 dA_c + \sum_{j=1}^{N_s} E_{st} x_j^2 dA_s + \sum_{k=1}^{N_f} E_{ft} x_k^2 dA_f \right] \quad (43)$$

The equations developed in this section are utilized in the tangent stiffness procedure given in the next section to develop moment-curvature relations for the cross sections studied in this research.

3.3.2 Tangent Stiffness Procedure

If the tangent stiffness matrix is known at any stage of loading, displacement vector corresponding to a load vector can be calculated by using Equation 37 and vice versa. The steps involved in computing moment-curvature relations using tangent stiffness method are summarized below [32]:

1. Calculate initial values for the tangent stiffness coefficients using Equations 38 through 43, assuming a small deflection vector so that the whole cross section is in elastic state.

2. Assume an increment in external load vector, in this case a small change in the bending moment M_x .
3. Compute the change in displacements caused by the assumed increment in the load using Equation 37.
4. Based on calculated displacements, find the strains in each element using Equation 17.
5. Find stresses in each element using stress strain relationship of each material given in Equations 1 through 5.
6. Find the corresponding total internal actions by adding the contribution from all elements using Equations 21 through 23.
7. Check the equilibrium of the external and internal actions. If equilibrium is satisfied, another increment of the load vector is considered and steps 2 to 7 are repeated. If equilibrium is not satisfied, find the unbalanced load vector.
8. Find the unbalanced displacement vector using Equation 37. Add the unbalanced displacements to the computed displacements and recalculate the internal actions following steps 4 through 7 until equilibrium is satisfied.
9. Repeat steps 2 through 8 until the maximum concrete strain reaches a predetermined ultimate strain value.

A MATLAB program is developed based on the above procedure to plot moment-curvature relationships and is given in Appendix C. Although, there is no significant applied axial load in the laboratory tests, it is considered in the program to make sure summation of internal compressive and tensile forces due to applied bending moment is equal to zero.

3.3.3 Moment-Curvature Relations

Moment-curvature relations of all specimens subjected to unsymmetrical bending are obtained using tangent stiffness procedure described in the previous section. The relations are shown in Figure 125 through Figure 134. Bending moment is increased until maximum compressive strain in concrete reached ultimate strain value given in Table 1. However, for the plain concrete sections (SS01 and SM04) bending moment is applied until tensile stress in concrete reached modulus of rupture of concrete which is given as $7.5\sqrt{f'_c}$.

The moment-curvature relations of plain concrete sections are a single straight line as shown in Figure 125 and Figure 127. The sections fail in a brittle manner once the maximum tensile stress reaches modulus of rupture of concrete. The relations of specimens SS02, SS03, and SM05 through SM07 have four distinct regions as shown in Figure 126 and Figure 128. The initial straight part is followed by a small horizontal region representing cracking of concrete in tension. This is followed by another upward straight line which ends with yielding of steel tension rebars. The stiffness of the section represented by the slope of the relation in this part is less than the stiffness in the initial uncracked straight part. The section fails in a ductile manner as demonstrated by the horizontal branch of the relation.

The relations of specimens SM08 through SM10 and SM11 through SM13 have five distinct regions as shown in Figure 129 and Figure 130. The initial straight part is followed by a small horizontal region representing cracking of concrete in tension. This is followed by another upward straight line which ends with yielding of steel tension rebars in the web part of the section. The stiffness of the section represented by the slope of the relation in this part is less than the stiffness in the initial uncracked straight part. This is followed by another upward line which ends with yielding of the longitudinal rebar provided in the flange part of the section. Finally, the section fails in a ductile manner as demonstrated by the horizontal branch of the relation.

The relations of specimens SM14 through SM19 with CFRP strips do not have a horizontal final branch but an upward straight line as shown in Figure 131 through Figure 134. After yielding of steel rebars, the stiffness of the section reduces further as demonstrated by the smaller slope of the last branch. The members fail in a brittle fashion once the maximum compressive strain in concrete reaches a predetermined ultimate value.

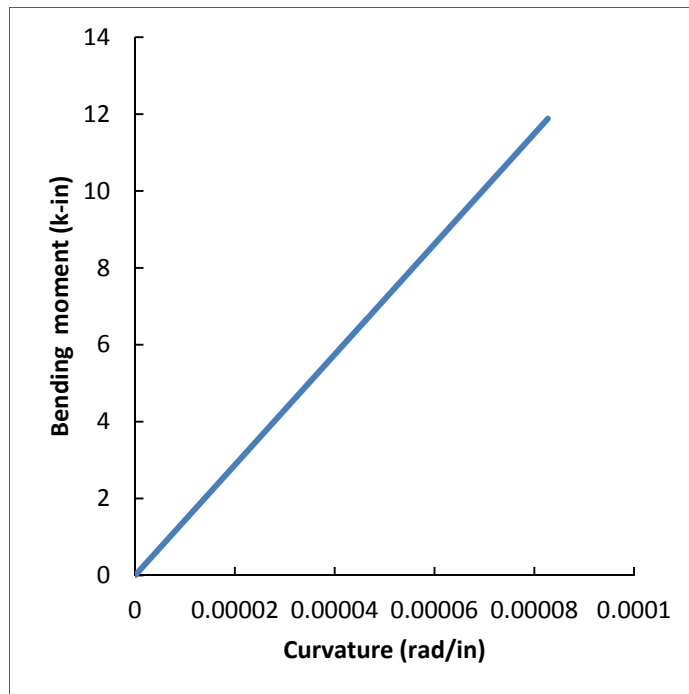


Figure 125. Moment-curvature relation of SS01

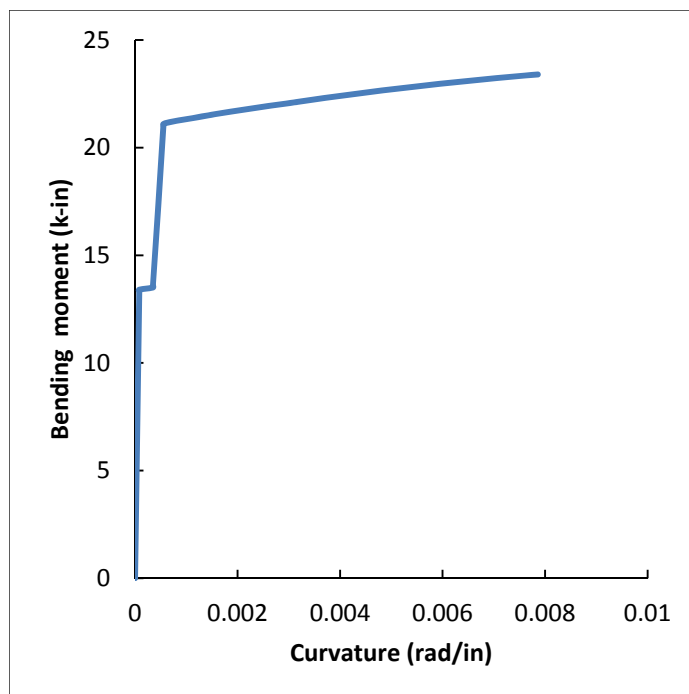


Figure 126. Moment-curvature relation of SS02 and SS03

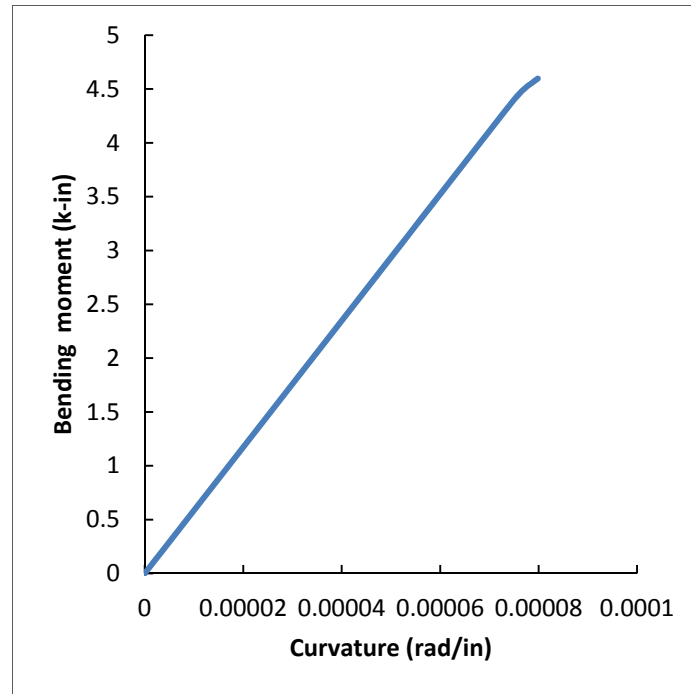


Figure 127. Moment-curvature relation of SM04

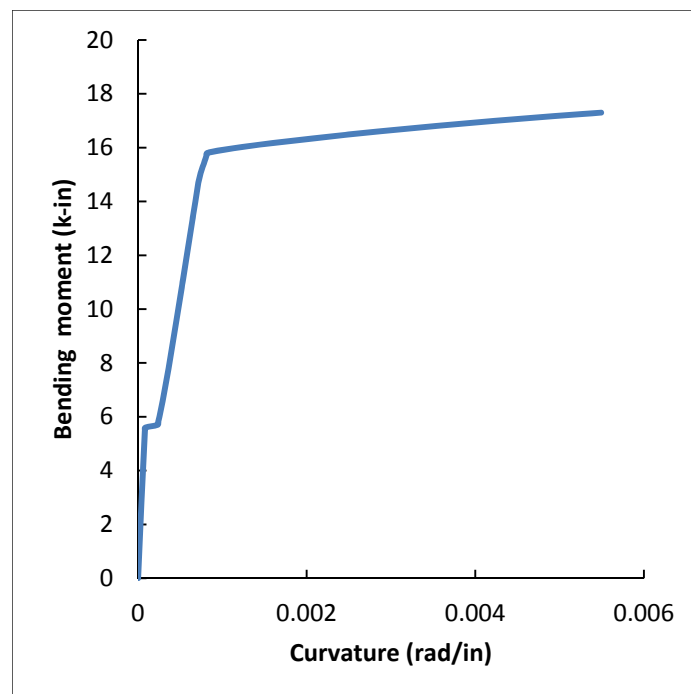


Figure 128. Moment-curvature relation of SM05-SM07

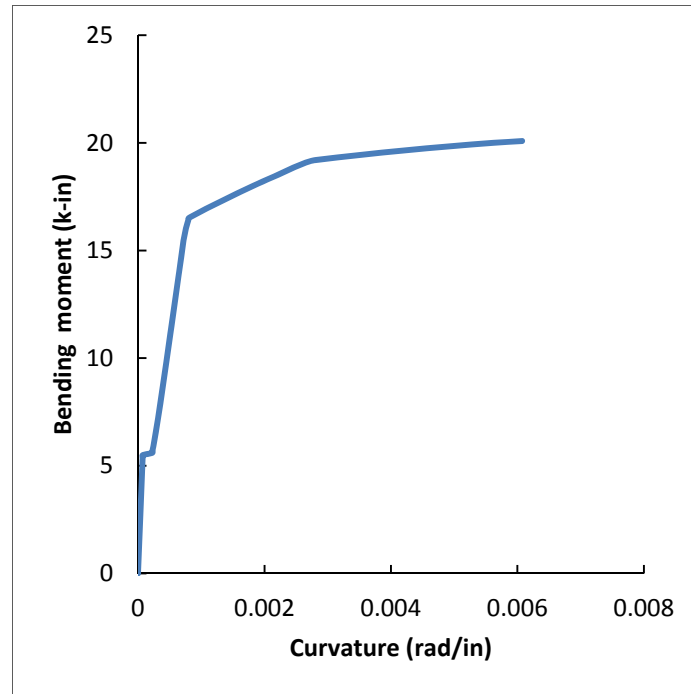


Figure 129. Moment-curvature relation of SM08-SM10

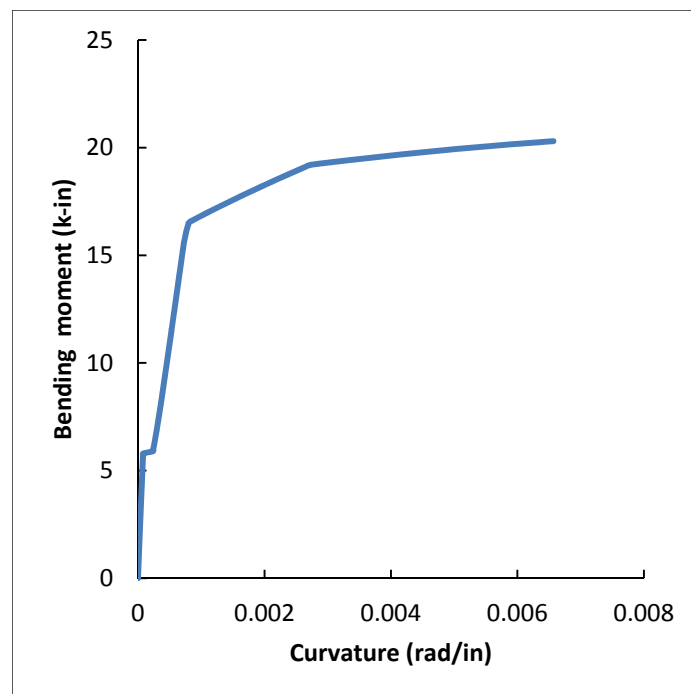


Figure 130. Moment-curvature relation of SM11-SM13

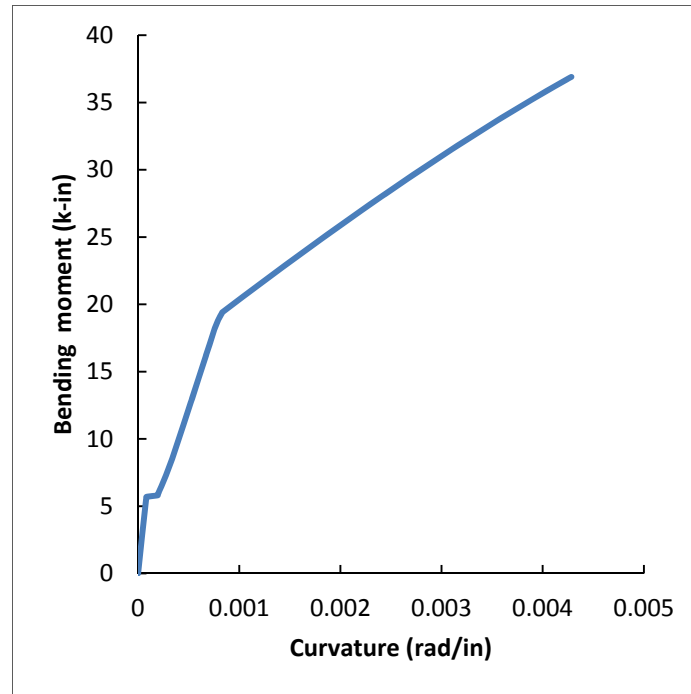


Figure 131. Moment-curvature relation of SM14

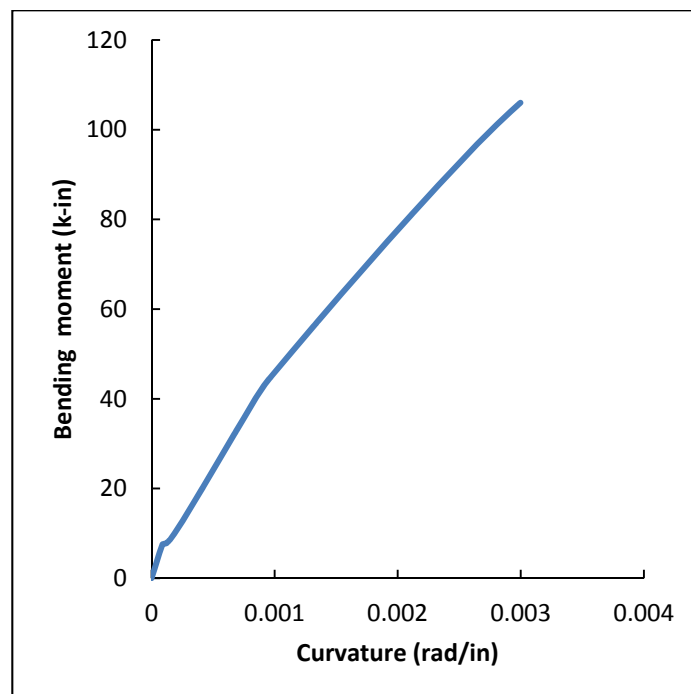


Figure 132. Moment-curvature relation of SM15

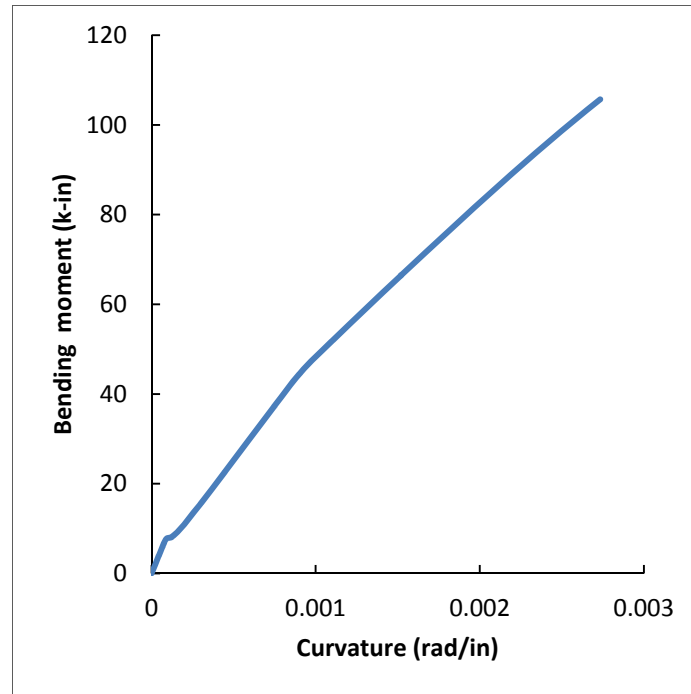


Figure 133. Moment-curvature relation of SM16

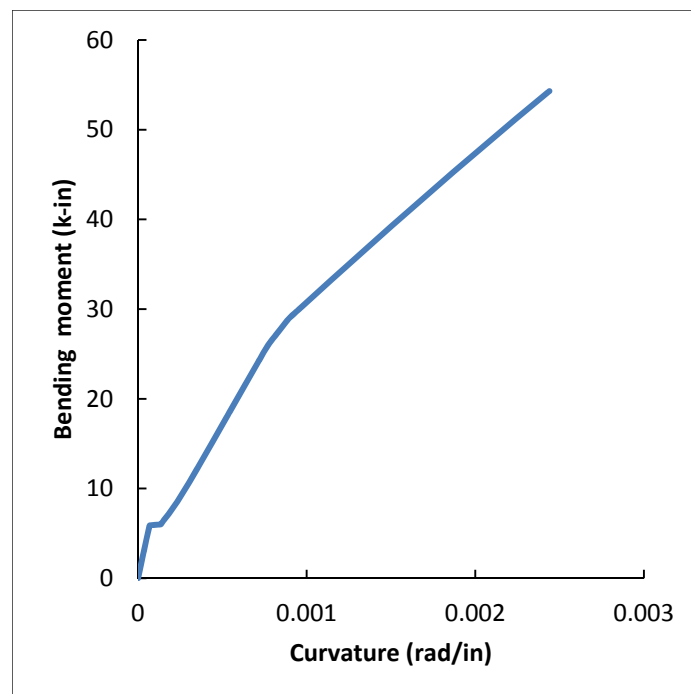


Figure 134. Moment-curvature relation of SM17-SM19

Table 7 shows a summary of the results obtained by moment-curvature analysis. A comparison of these values with the ones obtained by ultimate strength analysis show close agreement.

Table 7. Summary of results of moment-curvature analysis

Specimen	b (deg.)	Y₁ (in.)	Y₂ (in.)	Φ_{xu} (rad./in.)	M_{xu} (k-in.)
SS01	0.00	2.50	2.50	0.00008	11.88
SS02-SS03	0.00	0.48	0.48	0.00790	23.40
SM04	14.68	2.31	1.00	0.00008	4.60
SM05—SM07	5.94	0.69	0.17	0.00550	17.30
SM08—SM10	2.18	0.60	0.41	0.00610	20.08
SM11—SM13	2.29	0.59	0.39	0.00660	20.30
SM14	0.00	0.93	0.93	0.00430	36.90
SM15	1.14	1.33	1.23	0.00300	105.36
SM16	4.23	1.45	1.08	0.00270	105.12
SM17—SM19	7.07	1.27	0.65	0.00260	56.70

3.4 Retrofitting Schemes for L-shaped section under Unsymmetrical Bending

The program developed for tangent stiffness method was used to investigate many retrofitting schemes for L-shaped section by calculating the ultimate capacity under unsymmetrical bending. The purpose of this exercise is to determine the locations of a given number of CFRP strips that will maximize the bending capacity of a given section. The specimen SM05 is used as a control section for this purpose. Table 8 through Table 10 show the location of a given number of CFRP

strips to maximize bending capacity, the value of the maximum bending moment achieved, and an enhancement factor showing increase in bending capacity with respect to the control section. The capacity is increased over three times with the application of a single high strength CFRP strip as shown in Table 8. The capacity can be increased over nine times with the application of nine CFRP strips applied at appropriate locations as shown in Table 10.

Table 8. Maximum bending capacity for a given number of CFRP strips

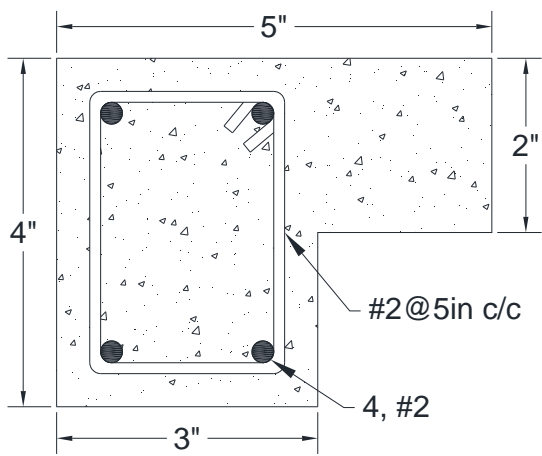
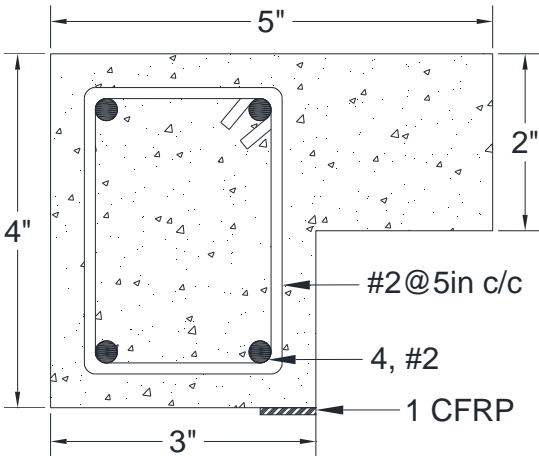
Control Section		Retrofitting Scheme 1	
			
M_{ux} (k-in)	17.30	M_{ux} (k-in)	62.16
Enhancement Factor, η	-	Enhancement Factor, η	3.59

Table 9. Maximum bending capacity for a given number of CFRP strips

Retrofitting Scheme 2		Retrofitting Scheme 3	
M_{ux} (k-in)	84.24	M_{ux} (k-in)	98.00
Enhancement Factor, η	4.87	Enhancement Factor, η	5.66
Retrofitting Scheme 4		Retrofitting Scheme 5	
M_{ux} (k-in)	106.80	M_{ux} (k-in)	118.80
Enhancement Factor, η	6.17	Enhancement Factor, η	6.87

Table 10. Maximum bending capacity for a given number of CFRP strips

Retrofitting Scheme 6		Retrofitting Scheme 7	
M_{ux} (k-in)	129.20	M_{ux} (k-in)	135.00
Enhancement Factor, η	7.47	Enhancement Factor, η	7.80
Retrofitting Scheme 8		Retrofitting Scheme 9	
M_{ux} (k-in)	147.00	M_{ux} (k-in)	158.20
Enhancement Factor, η	8.49	Enhancement Factor, η	9.14

The increase in bending capacity follows a straight line with increase in the area of CFRP strips provided, as shown in Figure 135.

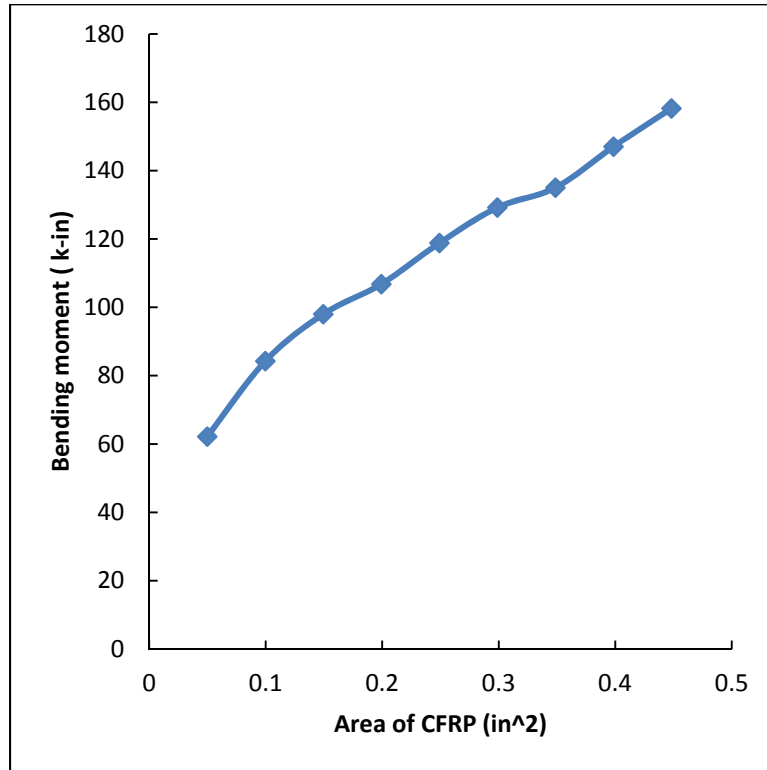


Figure 135. Ultimate bending moment with given CFRP area for SM05

3.5 Member Analysis under Unsymmetrical Bending

The member load-deflection relations under unsymmetrical bending are obtained using a piecewise linear finite difference algorithm (PLFD method). The deflected shape and bending moment diagram due to an applied bending moment at the top end is shown in Figure 136.

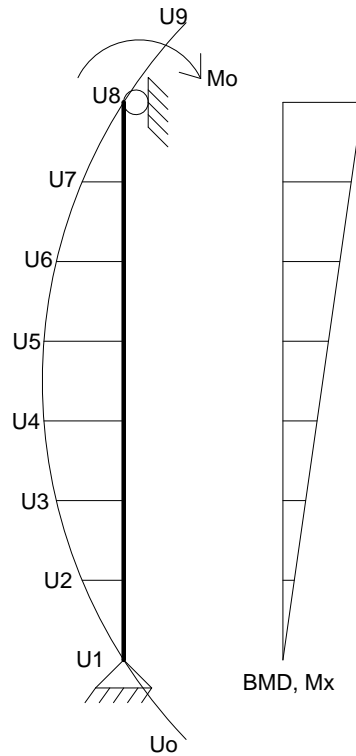


Figure 136. Bending moment about x-axis and corresponding deflections

The curvature at each section can be determined from the moment-curvature relation developed through tangent stiffness method. Using central finite difference approach, these curvatures are related to the deflections of the member at various sections as:

$$\phi_i = \left(\frac{d^2 u}{dz^2} \right)_i = \left[\frac{u_{i-1} - 2u_i + u_{i+1}}{(h)^2} \right] \quad (44)$$

in which ϕ_i and u_i represent curvature and deflection at a given section of the member, respectively. Substituting $i = 0$ to 8 in Equation 44 and writing the equations obtained in a matrix form gives:

$$h^2 \begin{Bmatrix} \varphi_{x1} \\ \varphi_{x2} \\ \varphi_{x3} \\ \varphi_{x4} \\ \varphi_{x5} \\ \varphi_{x6} \\ \varphi_{x7} \\ \varphi_{x8} \end{Bmatrix} = \begin{bmatrix} 1 & 1 & 0 & 0 & 0 & 0 & 0 & 0 \\ 0 & -2 & 1 & 0 & 0 & 0 & 0 & 0 \\ 0 & 1 & -2 & 1 & 0 & 0 & 0 & 0 \\ 0 & 0 & 1 & -2 & 1 & 0 & 0 & 0 \\ 0 & 0 & 0 & 1 & -2 & 1 & 0 & 0 \\ 0 & 0 & 0 & 0 & 1 & -2 & 1 & 0 \\ 0 & 0 & 0 & 0 & 0 & 1 & -2 & 0 \\ 0 & 0 & 0 & 0 & 0 & 0 & 1 & 1 \end{bmatrix} x \begin{Bmatrix} u_0 \\ u_2 \\ u_3 \\ u_4 \\ u_5 \\ u_6 \\ u_7 \\ u_9 \end{Bmatrix} \quad (45)$$

The moment-curvature relation is thus utilized in piecewise linear finite difference algorithm to obtain deflections at various locations along the length of the member. The step by step procedure for this technique is summarized below with reference to Figure 136.

1. The member is divided into n sections, each having a height of h .
2. Find the bending moment M_i at each section corresponding to the applied moment at the end of the member.
3. For the moments computed at each section, calculate the corresponding curvatures ϕ_i using tangent stiffness procedure outlined in section 3.3.
4. Substitute the values of curvatures at various sections in Equation 45 to obtain corresponding deflections.
5. Repeat the process to obtain moment-deflection relation at any required location along the length of the member.

A MATLAB program was written in accordance to the above procedure to predict the deflection at the center of the isolated members and is included in Appendix D. The moment-deflection relations obtained are given in Figure 145 and Figure 156 along with the corresponding experimental relations.

3.6 Cracking Torsional Strength

The cracking torque of members was determined using elastic theory and transformed area principal. The results are obtained using actual factors of St. Venant theory rather than the approximated factors for thin walled section. The L-shaped sections are considered as a

combination of two rectangles and the transformed areas of steel reinforcement and CFRP strips are added to the faces of the section where they are located.

3.6.1 Cracking Torque under Pure Torsion

The applied torque causing a maximum shear stress, τ_{max} , in the middle of the wider side of a rectangular section is given by [33].

$$T = \frac{\tau_{max} k_1}{k_2 x} \quad (46)$$

where x is the smaller side of the rectangle. The coefficients k_1 and k_2 in Equation 46 depends on the cross-sectional dimensions and are given by:

$$k_1 = f_2 \frac{x^3 y}{3} \quad (47)$$

$$k_2 = 1 - \frac{8}{\pi^2} \sum \frac{1}{(2n+1)^2} \frac{1}{\cosh f_1} \quad n = 0,1,2 \dots \quad (48)$$

where y is the longer side of the rectangle. The coefficients f_1 and f_2 depends on the cross-sectional dimensions and are given by:

$$f_1 = \frac{2n+1}{2} \pi \left(\frac{y}{x} \right) \quad n = 0,1,2 \dots \quad (49)$$

$$f_2 = 1 - \frac{192}{\pi^5} \left(\frac{x}{y} \right) \sum \frac{1}{(2n+1)^5} \tanh f_1 \quad n = 0,1,2 \dots \quad (50)$$

In members under pure torsion, maximum shear stress is equal to the principal tensile stress. Therefore, cracking torque of a member is determined if the maximum shear stress is equated to the tensile strength of concrete in Equation 46 resulting in:

$$T_{cr} = \sum \frac{f_{ct} k_1}{k_2 x} \quad (51)$$

The results obtained using Equation 51 are given in Table 11 along with the values obtained from laboratory tests.

3.6.2 Cracking Torque under combined Bending and Torsion

The principal normal stress under plane stresses is given by [3]:

$$\sigma_{1,2} = \frac{\sigma_x + \sigma_y}{2} \pm \sqrt{\left(\frac{\sigma_x - \sigma_y}{2}\right)^2 + \tau_{xy}^2} \quad (52)$$

The normal stress due to a bending moment about x axis in Figure 120 is given by Equation 7 as mentioned in Section 3.2. Similarly, the maximum shear stress due to torsion is given by:

$$\tau_{T,max} = \sum \frac{T k_2 x}{k_1} \quad (53)$$

Substituting Equations 7 and 53 in Equation 52 and rearranging the terms results in:

$$T_{cr} = \sqrt{\left(f_{ct} - \left[\frac{I_{xy}x - I_y y}{2(I_x I_y - I_{xy}^2)}\right] M\right)^2 - \left(\left[\frac{I_{xy}x - I_y y}{2(I_x I_y - I_{xy}^2)}\right] M\right)^2} \sum \frac{k_1}{k_2 x} \quad (54)$$

This equation gives the value of the cracking torque under the action of combined unsymmetrical bending and torsion. The results obtained for cracking torque for the specimens tested under combined bending and torsion are given in Table 12. The experimental values of cracking torque are also given in this table for comparison.

3.7 Ultimate Torsional Strength

The torsional strength of a reinforced concrete section can be calculated by Equation 55 derived by Elfren et al. [34] based on principals of skew bending theory.

$$T_n = \frac{2A_o A_t f_{yt}}{s} \cot \theta \quad (55)$$

In this equation, A_o is the concrete area enclosed by the transverse stirrups, A_t is the area of one leg of the stirrup, f_{yt} is the yield strength of stirrup reinforcement, s is the spacing of the stirrups, and θ is the angle of the concrete compression diagonal with the axis of the member. In order to account for steel and CFRP reinforcement outside the stirrups, the term A_o is modified to include the transformed area of these elements. The new term denoted as A_{om} results in:

$$T_n = \frac{2A_{om}A_t f_{yt}}{s} \cot \theta \quad (56)$$

The comparison of the results obtained from Equations 55 and 56 with the test values is given in Table 13.

3.8 Flexural-Torsional Interaction Relations

The flexural-torsional interaction for reinforced concrete sections has been modelled as linear, trilinear, circular, and parabolic in the past. The ACI interaction relations are based on skew bending theory as proposed by Elfren et al. [34]. However, to account for unsymmetrical arrangement of longitudinal reinforcement, a new parameter r is defined in the code which is the ratio of the force in the top reinforcement rebars at yielding to the force in the bottom rebars at yielding. As a result, the interaction surface is enclosed by

$$r \left(\frac{T}{\frac{2A_o A_t f_{yt}}{s} \cot \theta} \right)^2 + \frac{M}{A_s f_y \left(d - 0.59 \frac{A_s f_y}{b f'_c} \right)} = 1 \quad (57)$$

$$\left(\frac{T}{\frac{2A_o A_t f_{yt}}{s} \cot \theta} \right)^2 - \frac{1}{r} \frac{M}{A_s f_y \left(d - 0.59 \frac{A_s f_y}{b f'_c} \right)} = 1 \quad (58)$$

where b is the width of the web of the section and d is the distance of tension reinforcement from the compression face. The interaction Equations 57 and 58 are modified to account for the CFRP retrofitting and the effect of L-shaped cross section on the neutral axis. Therefore, using Equations 12 and 56 for the maximum bending and torsion capacity of the section gives the modified interaction equations as follows:

$$r \left(\frac{T}{\frac{2A_{om}A_t f_{yt}}{s} \cot \theta} \right)^2 + \frac{M}{0.85f'_c \left[\frac{1}{2} \beta_1^2 x_1 y_1 \right] \bar{y} + \sum_{i=1}^n f_{si} A_{si} y_{si} + \sum_{i=1}^m f_{fi} A_{fi} y_{fi}} = 1 \quad (59)$$

$$\left(\frac{T}{\frac{2A_o A_t f_{yt}}{s} \cot \theta} \right)^2 - \frac{1}{r} \frac{M}{0.85f'_c \left[\frac{1}{2} \beta_1^2 x_1 y_1 \right] \bar{y} + \sum_{i=1}^n f_{si} A_{si} y_{si} + \sum_{i=1}^m f_{fi} A_{fi} y_{fi}} = 1 \quad (60)$$

The interaction relations are given in Figure 157 and Figure 166 along with the results obtained from the laboratory experiments. A summary of the results is given in Table 14.

3.9 Torque versus Angle of Twist Relations

Mitchell and Collins [35] proposed the Compression Field Theory (CFT) for torsion of reinforced concrete members by combining the equilibrium, compatibility, and constitutive relationships. Figure 137 shows a prismatic reinforced concrete member subjected to an applied torque T . The applied torque is resisted by diagonal compression in concrete elements which spiral around member at an angle α_r . The tangential component of these compressive stresses form the circulatory shear flow q which occupies the shear flow zone having thickness t_d . This thickness is a variable determined from equilibrium and compatibility conditions.

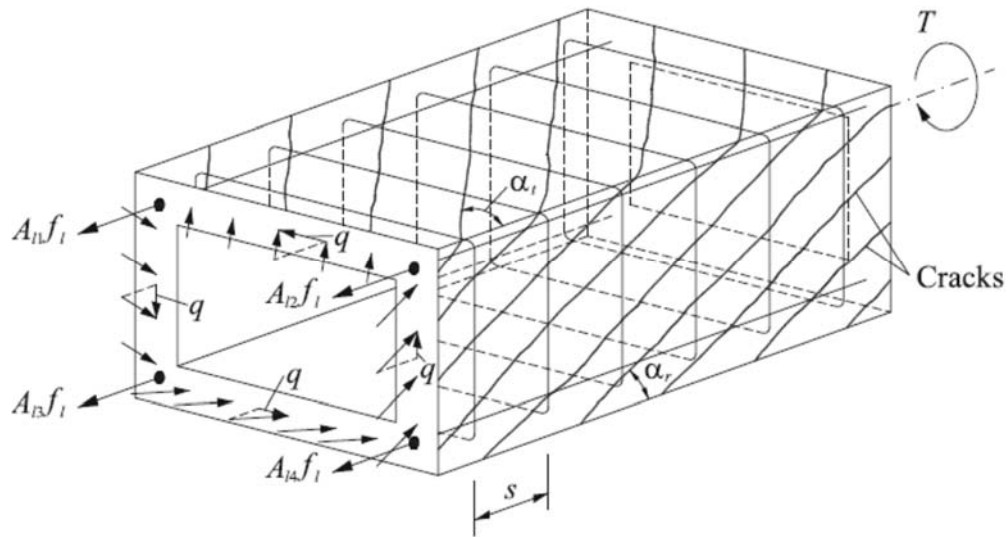


Figure 137. Equilibrium of cracked model [36]

An element in the shear flow zone is shown in Figure 138. Considering the in-plane equilibrium of this elements, Nielsen [38], Lampert and Thurlimann [39] and Mitchell and Collins [35] derived three equilibrium equations. Equations 61 through 63 are the general form of these equations [37].

$$\sigma_l = \sigma_d \cos^2 \alpha_r + \sigma_r \sin^2 \alpha_r + \rho_l f_l \quad (61)$$

$$\sigma_t = \sigma_d \sin^2 \alpha_r + \sigma_r \cos^2 \alpha_r + \rho_t f_t \quad (62)$$

$$\tau_{lt} = (-\sigma_d + \sigma_r) \sin \alpha_r \cos \alpha_r \quad (63)$$

where the reinforcement ratios ρ_l and ρ_t should be taken with respect to the shear flow zone thickness t_d .

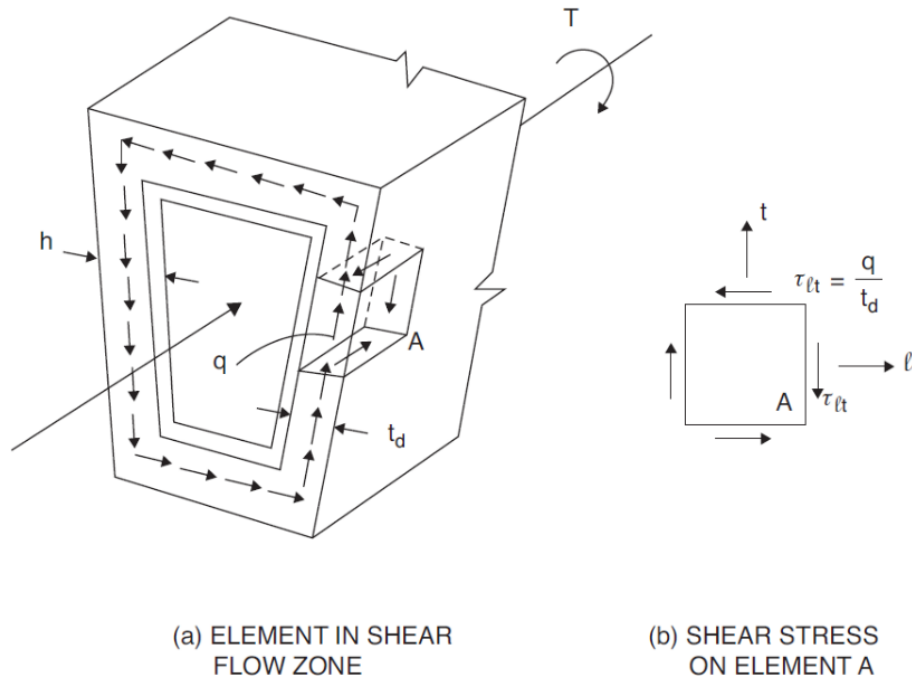


Figure 138. An element in the shear flow zone [37]

Apart from equilibrium of small elements, the overall equilibrium of the cross section must also be satisfied. Bredt [40] derived this fourth equilibrium equation given as:

$$\tau_{lt} = \frac{T}{2A_0 t_d} \quad (64)$$

The compatibility equations were originally derived by Baumann [41] and Mitchell and Collins [35]. The in-plane deformation of Element A in Figure 138 should satisfy the following three compatibility equations:

$$\epsilon_l = \epsilon_d \sin^2 \alpha_r + \epsilon_r \cos^2 \alpha_r \quad (65)$$

$$\epsilon_t = \epsilon_d \cos^2 \alpha_r + \epsilon_r \sin^2 \alpha_r \quad (66)$$

$$\frac{\gamma_{lt}}{2} = (-\epsilon_d + \epsilon_r) \sin \alpha_r \cos \alpha_r \quad (67)$$

A fourth compatibility equation was derived by Bredt [42] relating member angle of twist and shear strain in the shear flow zone.

$$\theta = \frac{p_o}{2A_o} \gamma_{lt} \quad (68)$$

The curvature of concrete struts is related to the angle of twist:

$$\Psi = \theta \sin 2\alpha_r \quad (69)$$

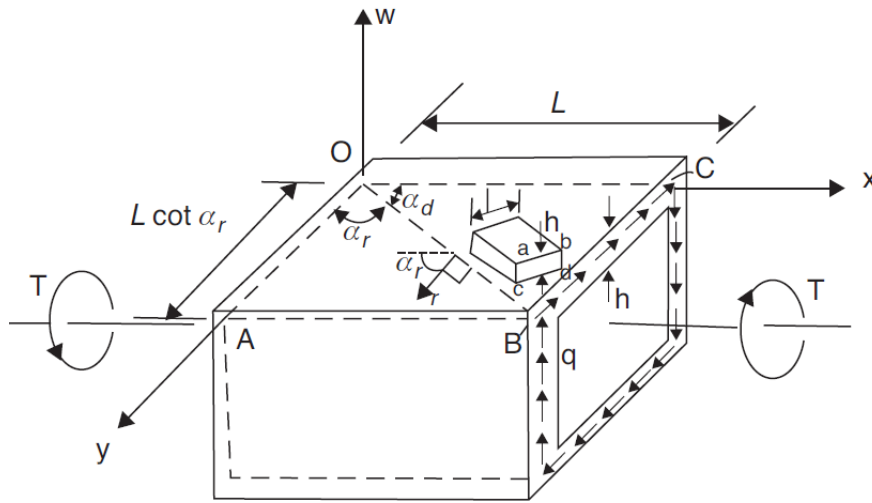


Figure 139. Section subjected to torsion [37]

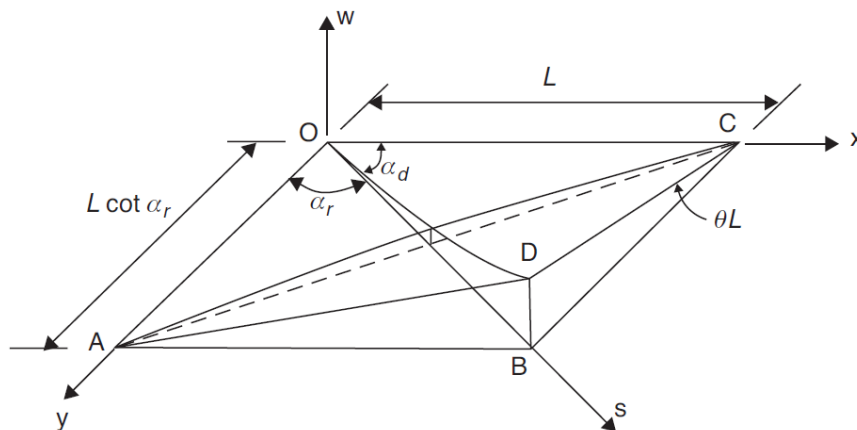


Figure 140. Deformation of top wall [37]

The curvature of concrete struts produces a non-uniform strain distribution in concrete struts as shown in Figure 140. From the geometry of Figure 141, we can derive:

$$t_d = \frac{\epsilon_{ds}}{\psi} \tag{70}$$

$$\epsilon_d = \frac{\epsilon_{ds}}{2} \tag{71}$$

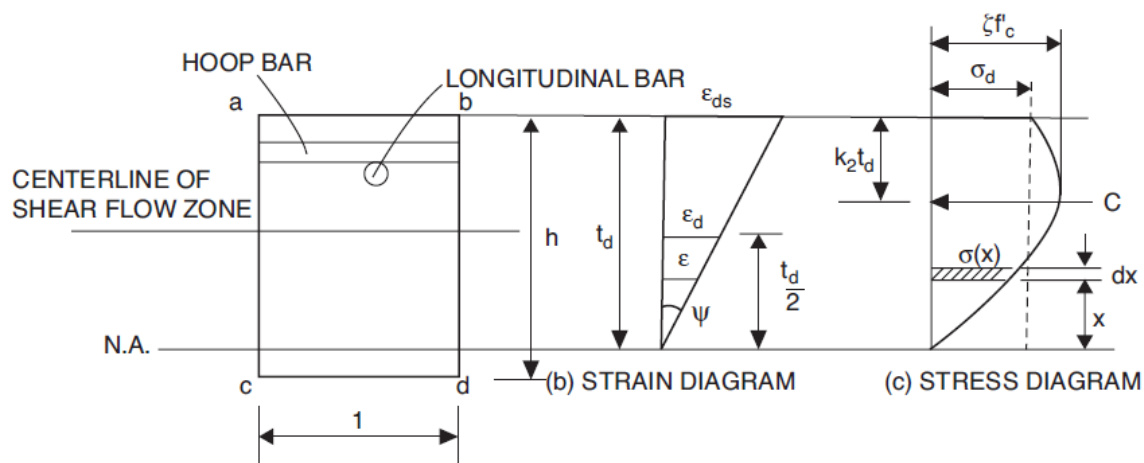


Figure 141. Strain and stress distribution in concrete struts

Using the relations given above, the equation required for the solution algorithm given as a flowchart in Figure 142 are derived and given below.

$$a = \frac{A_l f_l}{\alpha' f_c' p_o} + \frac{A_h f_h}{\alpha' f_c' s} \quad (72)$$

$$\varepsilon_l = \frac{\varepsilon_{ds} \alpha' \beta f_c' A_o}{2 A_l f_l} - \varepsilon_{ds} \left(1 - \frac{\beta}{2}\right) \quad (73)$$

$$\varepsilon_t = \frac{\varepsilon_{ds} \alpha' \beta f_c' A_o s}{2 A_h f_h p_h} - \varepsilon_{ds} \left(1 - \frac{\beta}{2}\right) \frac{p_o}{p_h} \quad (74)$$

$$T = 2A_o q \quad (75)$$

$$q = \sqrt{\left(\frac{A_l f_l}{p_o}\right) \left(\frac{A_h f_h}{s}\right)} \quad (76)$$

$$\theta = \frac{\varepsilon_{ds} \alpha' \beta f_c'}{2 q} \quad (77)$$

These equations are utilized in an iterative algorithm to predict the complete torque versus angle of twist relations for the specimens tested. The solution algorithm is presented in the form of a flowchart in Figure 142.

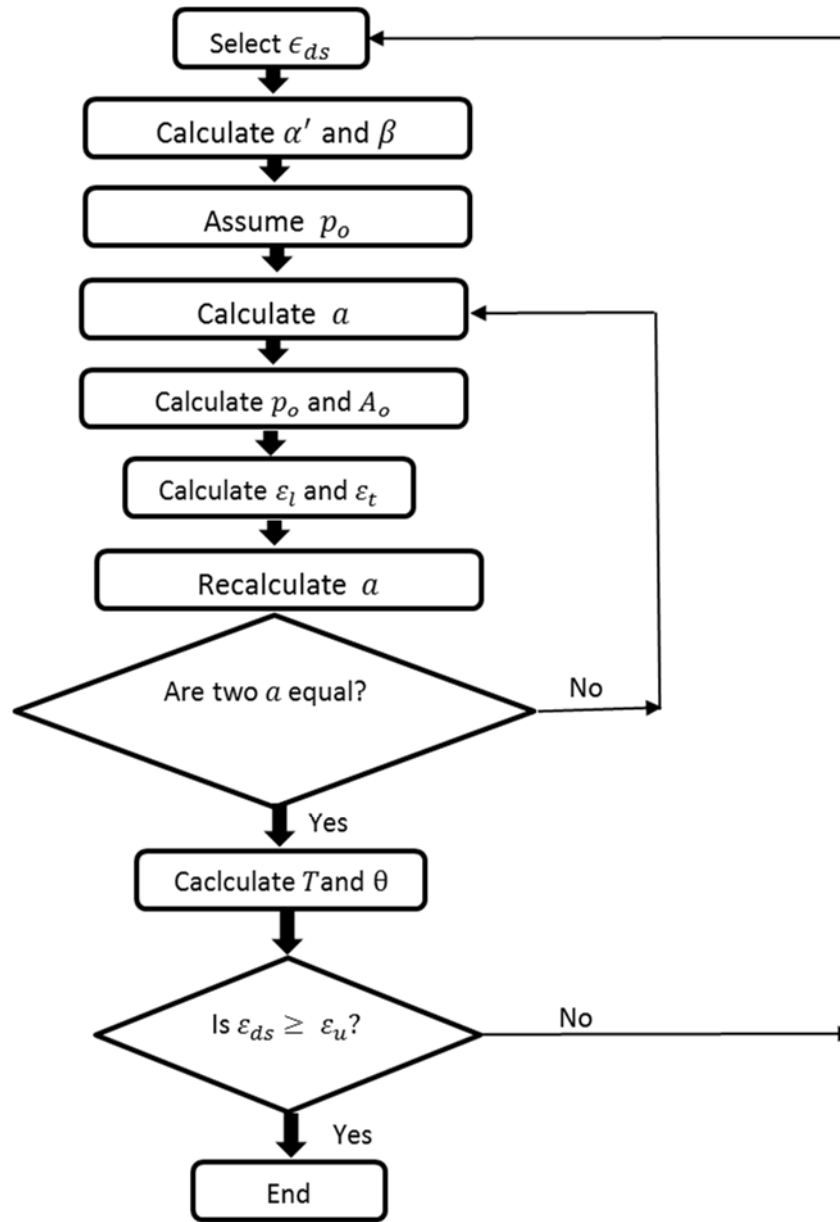


Figure 142. Solution algorithm flowchart for torsional analysis using CFT

The relations obtained using MCFT are shown in Figure 167 through Figure 172 along with the experimentally obtained relations.

3.10 Ultimate Load of Slab-beam Systems

The ultimate load(s) capacity of the slab-beam system depends on governing failure pattern which in turn depends on the location(s) of the applied load(s). If the load(s) are applied closer to the midspan of the slab, the slab cracks before the spandrel members experience any cracking. However, if the load(s) are applied closer to the spandrel members, the cracking starts in the spandrel members first. Therefore, the ultimate load capacity of the slab-beam system is the minimum of the yield line load(s) of the slab and the load(s) determined based on the interaction relation for the spandrel members.

The yield line pattern of a rectangular slab subjected to a concentrated load at midspan is shown in Figure 143. If the slab is isotropically reinforced with only positive rebars, the ultimate load supported by the slab is given by [38].

$$P_u = 8A_s f_y \left(d - 0.59A_s \frac{f_y}{f_c'} \right) \quad (78)$$

where A_s is the steel area per unit width, f_y is the yield strength of rebars, and d is the distance from the center of steel rebars to the top of the slab. This equation can be used to calculate the ultimate load for the slab-beam specimen SL01.

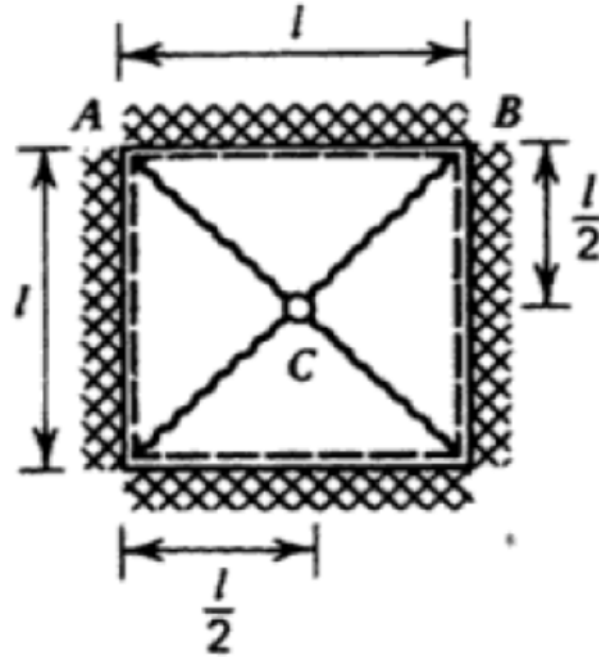


Figure 143. Yield line pattern for rectangular slab with one point load [38]

A rectangular slab subjected to two point loads develops the yield line pattern shown in Figure 144. If the slab has only isotropic positive steel reinforcement, Equation 79 can be used to calculate the ultimate load resisted by the slab [38].

$$P_u = m_u \left(\frac{l_y}{l_1} + 2 \frac{l_x}{l_y} \right) \quad (79)$$

where the geometrical terms are defined as shown in Figure 144. The ultimate positive moment capacity per unit width denoted by m_u is given by:

$$m_u = A_s f_y \left(d - 0.59 A_s \frac{f_y}{f'_c} \right) \quad (80)$$

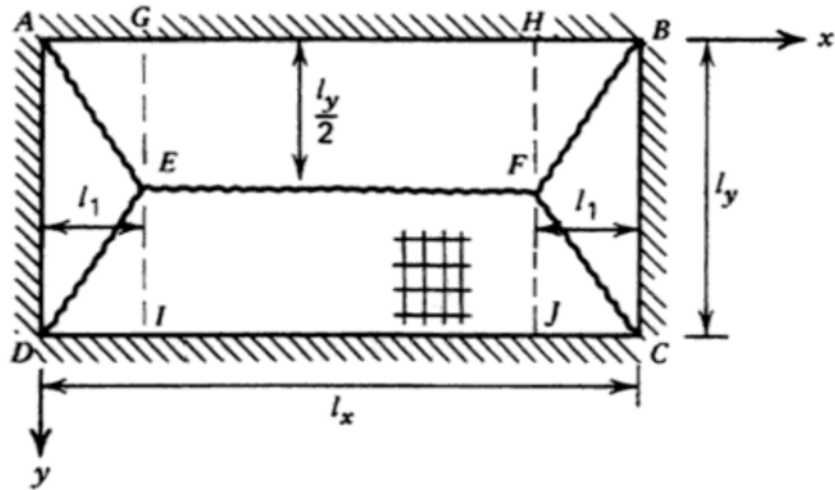


Figure 144. Yield line pattern for rectangular slab with two point loads [38]

The results of yield line analysis are given in Table 15 along with the values calculated in the laboratory tests.

The spandrel members in slab-beam systems are subjected to combined bending and torsional moments transferred from the slab. Substituting the values of torsional moment and bending moment of a point load in the interaction equation results in Equation 81.

$$\left(\frac{Pl_1}{2T_0}\right)^2 - \frac{1}{r} \frac{Pl}{4M_0} = 1 \quad (81)$$

where l_1 is the distance of the point load from the center of the spandrel member as shown in Figure 144 and l is the length of the slab. Equation 81 is used to determine the ultimate load resisted by SL03 where the spandrel members experienced major cracking before failure of the slab. The results are given in Table 15.

4. EXPERIMENTS VERSUS THEORY

4.1 Introduction

This chapter presents the comparison of experimental versus theoretical results. The procedures outlined in Chapter 3 are used for theoretical prediction. The moment-deflection relations are developed using nonlinear piecewise finite difference procedures. A comparison of cracking and ultimate torsional strengths found in the laboratory is given with those predicted by theory. Finally, ultimate strength bending-torsion interaction relations are given along with laboratory results.

4.2 Moment-deflection Relations

Figure 145 through Figure 156 presents the comparison of experimental and theoretical moment-deflection relations. The theoretical relations are obtained using the process outlined in Section 3.5. All the specimens were subjected to a fraction of the cracking bending moment capacity before applying torsional moment to ultimate capacity except for SM13 and SM18. Therefore, the moment-deflection relations are straight lines for these specimens and represent an elastic behavior. However, SM13 was subjected to torsional moment first before applying a bending moment to failure whereas SM18 was subjected to only a bending moment until local cracking occurred at the top end.

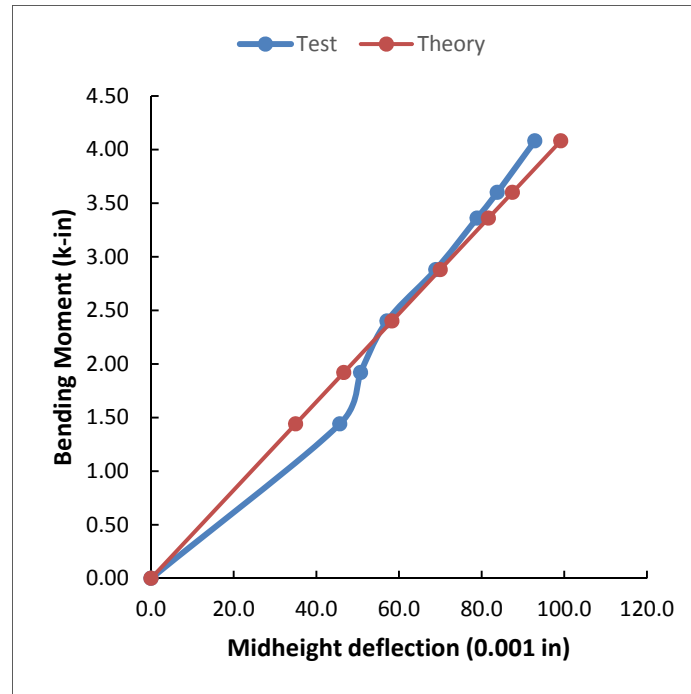


Figure 145. Moment-deflection relation of SS01

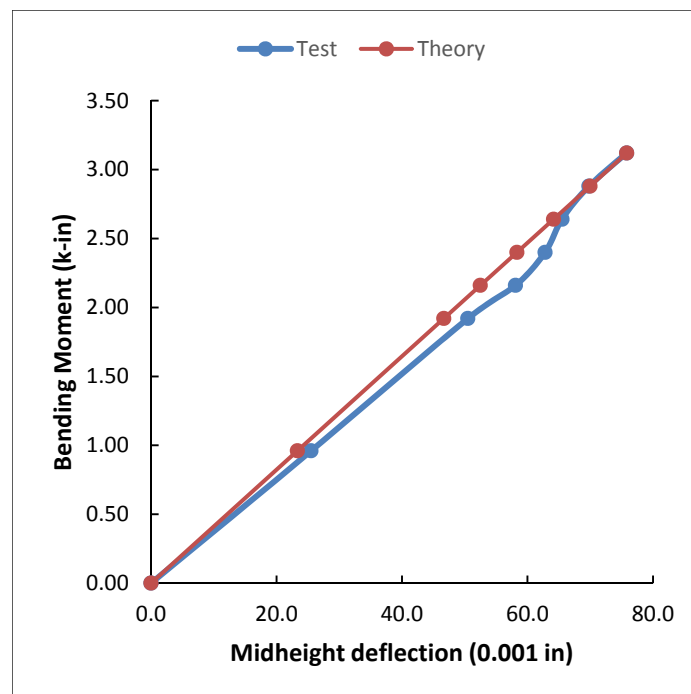


Figure 146. Moment-deflection relation of SS02

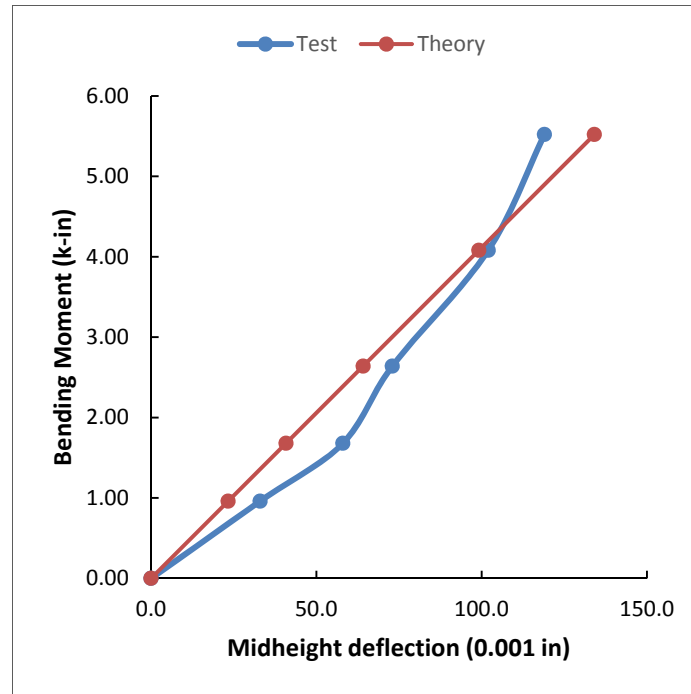


Figure 147. Moment-deflection relation of SS03

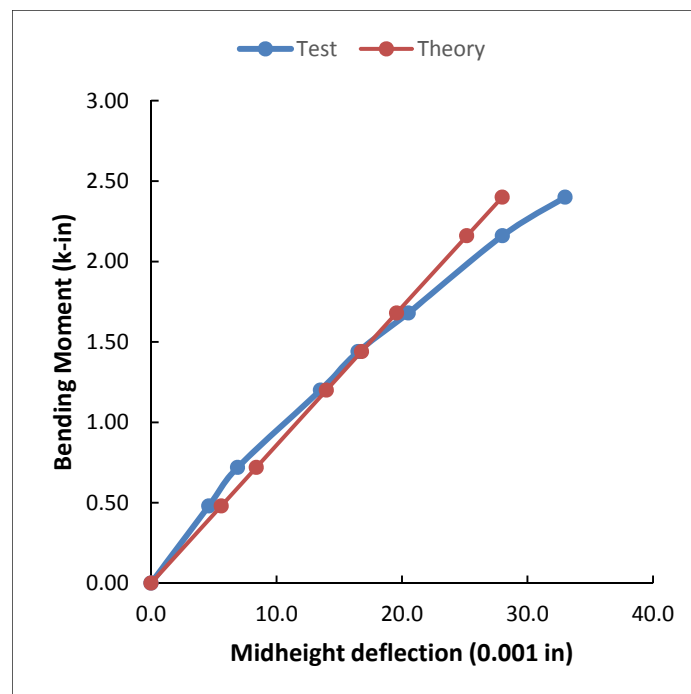


Figure 148. Moment-deflection relation of SM07

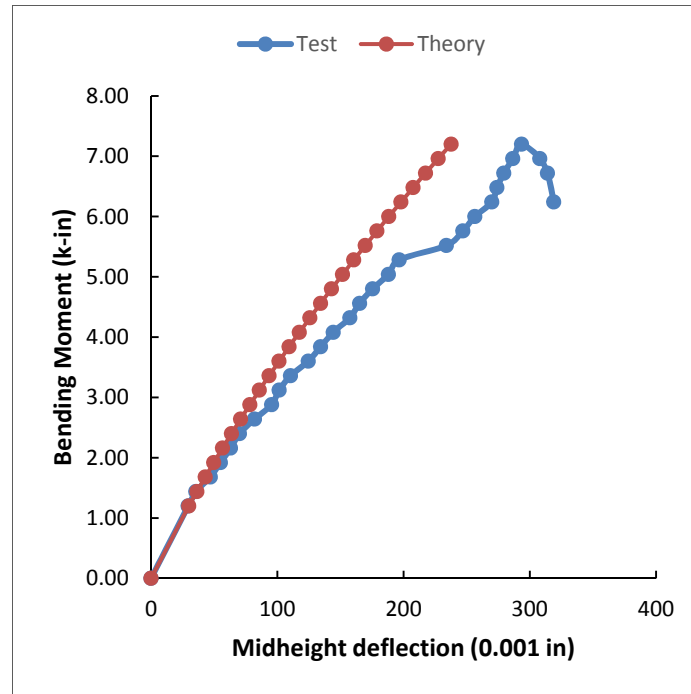


Figure 149. Moment-deflection relation of SM09

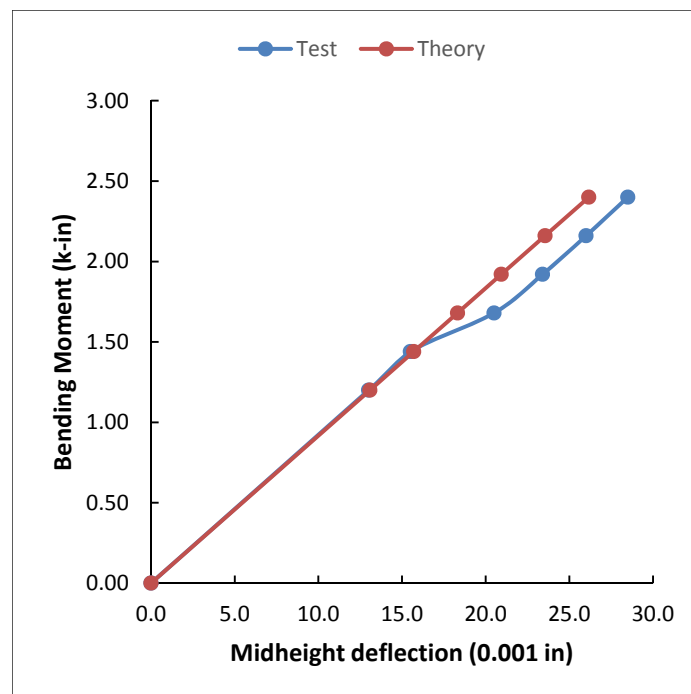


Figure 150. Moment-deflection relation of SM10

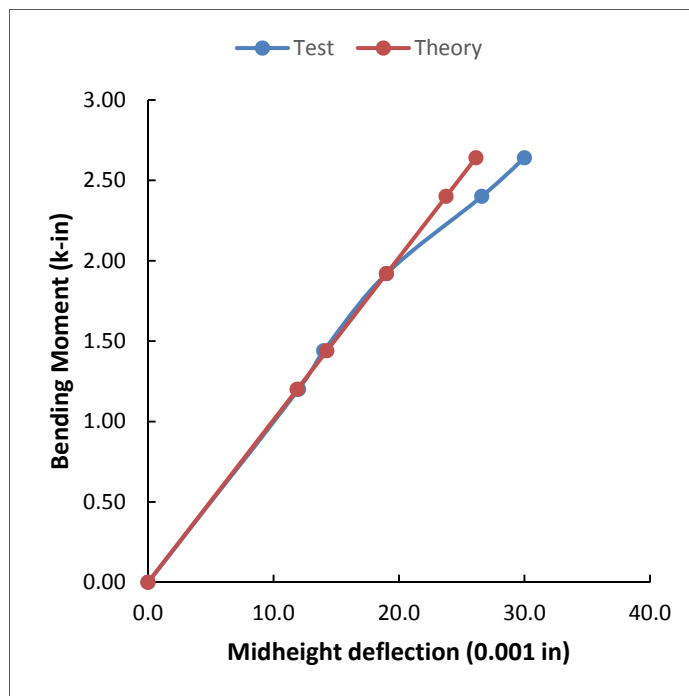


Figure 151. Moment-deflection relation of SM12

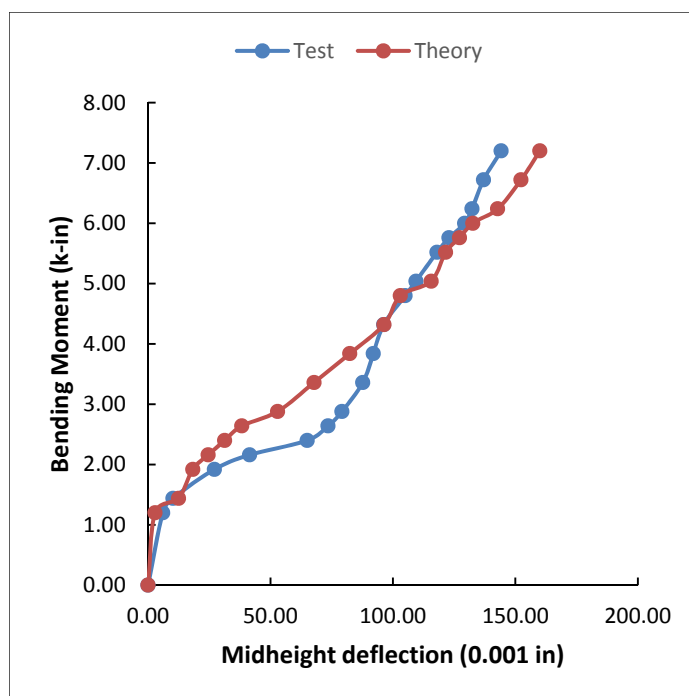


Figure 152. Moment-deflection relation of SM13

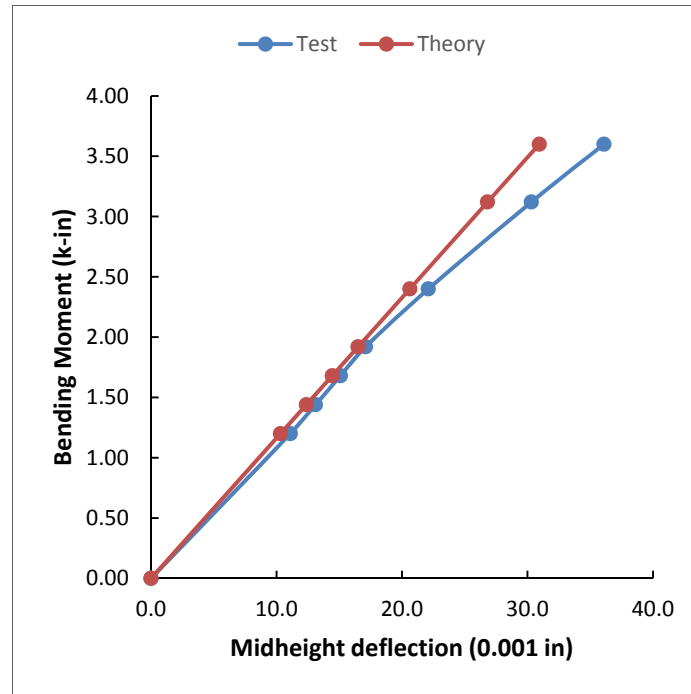


Figure 153. Moment-deflection relation of SM15

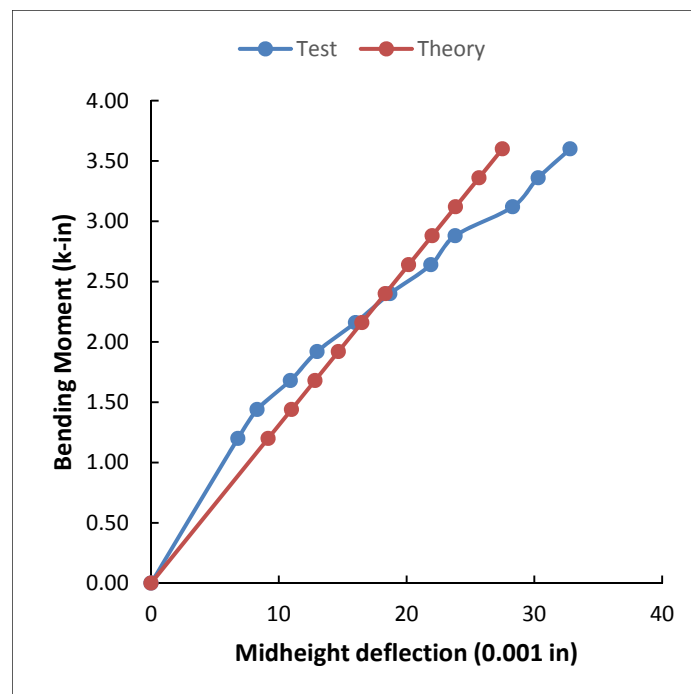


Figure 154. Moment-deflection relation of SM16

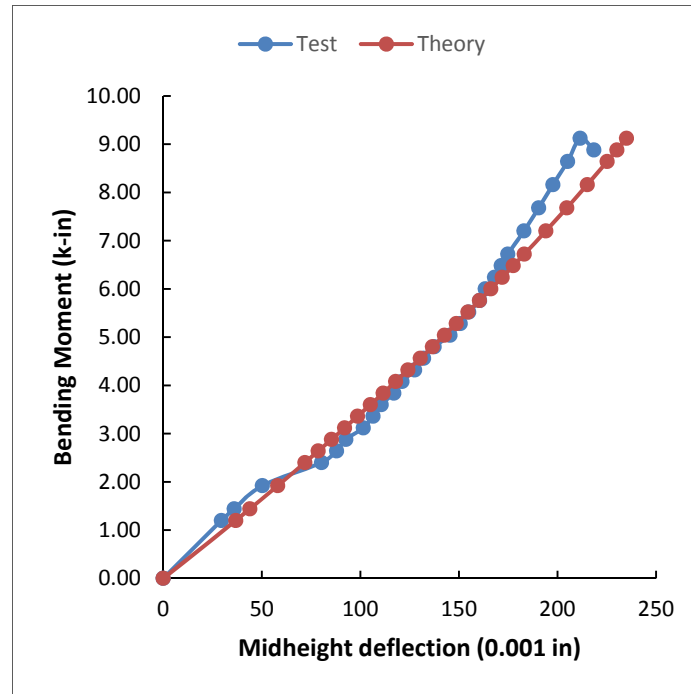


Figure 155. Moment-deflection relation of SM18

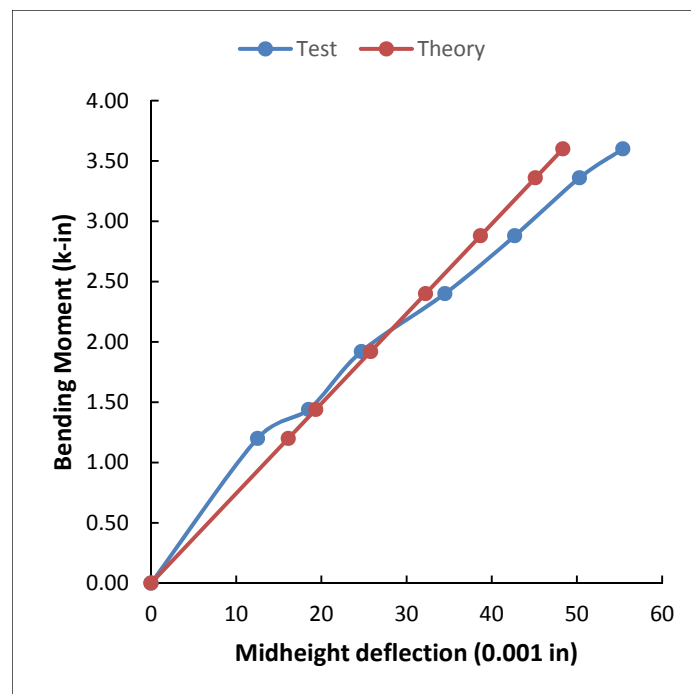


Figure 156. Moment-deflection relation of SM19

4.3 Cracking Torsional Strength

The experimental and theoretical values of cracking torque for specimens tested under torsional moment only are shown in Table 11. The theoretical values are calculated using the procedure outlined in Section 3.7. The maximum difference between theoretical and experimental values was found to be 18 percent in the case of SM17 whereas the minimum is 3 percent in the case of SM05. The average of the differences is 4 percent, which is indication that the theory and experiments are in reasonable agreement.

Table 11. Torque at cracking under pure torsion

Specimen	$T_{cr,test}$ (k-in)	$T_{cr,calc}$ (k-in)	$T_{cr,test} / T_{cr,calc}$
SM04	3.32	3.71	0.89
SM05	4.04	4.16	0.97
SM08	4.44	4.25	1.04
SM11	4.08	4.45	0.92
SM14	4.95	4.47	1.11
SM17	3.60	4.38	0.82

Table 12 shows the results of cracking torque for the specimens subjected to combined bending and torsional moments. The maximum difference between theoretical and experimental values was found to be 22 percent in the case of SM19 whereas the minimum is 3 percent in the case of SM10. The average of the differences is 12 percent. The agreement of theory and experiments is reasonably good.

Table 12. Cracking torsional strength under combined bending and torsion

Specimen	M_{applied} (k-in)	$T_{cr, \text{test}}$ (k-in)	$T_{cr, \text{calc}}$ (k-in)	$T_{cr, \text{test}} / T_{cr, \text{calc}}$
SM01	1.44	9.11	10.38	0.88
SM02	1.44	9.90	11.06	0.89
SM03	6.00	13.82	13.97	1.03
SM07	3.84	5.15	6.13	0.84
SM10	2.40	5.43	5.59	0.97
SM12	2.64	5.12	5.94	0.86
SM15	3.60	6.02	6.64	0.91
SM16	3.60	5.76	7.17	0.80
SM19	3.60	4.83	6.23	0.78

4.4 Ultimate Torsional Strength

Table 13 gives a comparison of the ultimate torsional strength for the spandrel members tested under torsional moment only. The theory and experiments are in very good agreement except for specimen SM17. This specimen showed signs of poor construction so the experimental strength was less than anticipated. For the rest of specimens, the theory and experiments are in excellent agreement where the average difference between the two is only 2%.

Table 13. Peak torque under pure torsion

Specimen	$T_{n,test}$ (k-in)	$T_{n,test} / T_{n,calc}$	
		Original Skew Bending	Modified Skew Bending
SM04	3.32	1.03	-
SM05	4.99	1.09	-
SM08	5.15	1.08	1.01
SM11	4.83	1.01	0.96
SM14	5.23	1.10	0.99
SM17	4.32	0.91	0.75

4.5 M-T Interaction for ultimate torque

Figure 157 through Figure 166 show the interaction of bending and torsional moment strengths for isolated members. The figures also have the data point obtained from tests results.

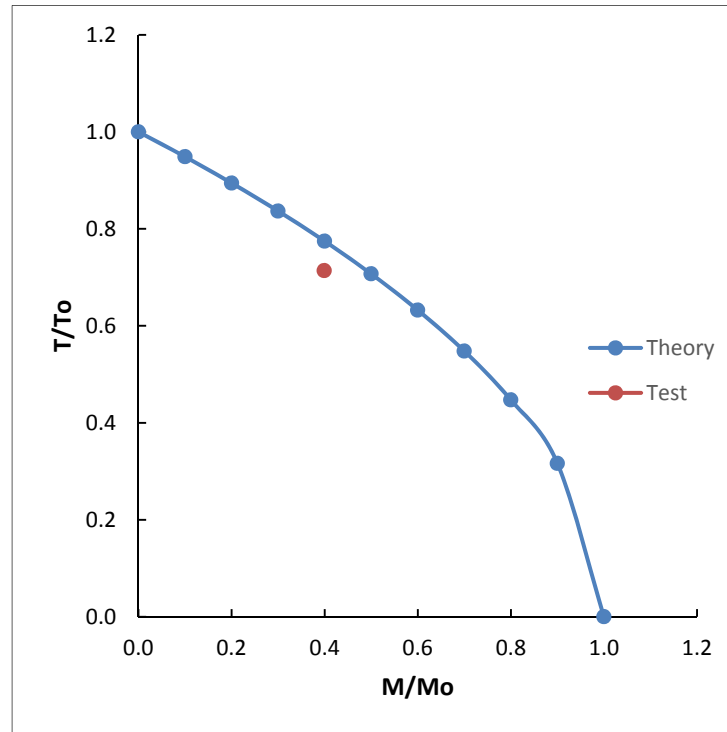


Figure 157. M-T interaction for SS01

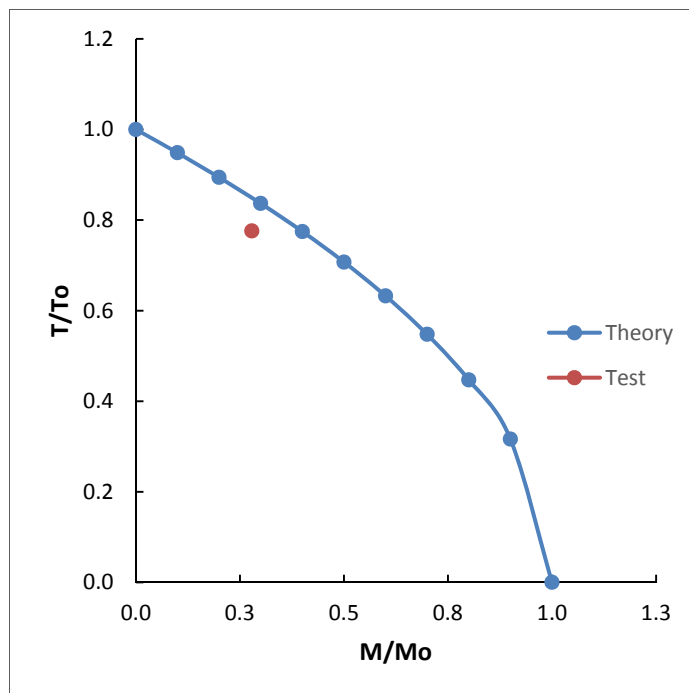


Figure 158. M-T interaction for SS02

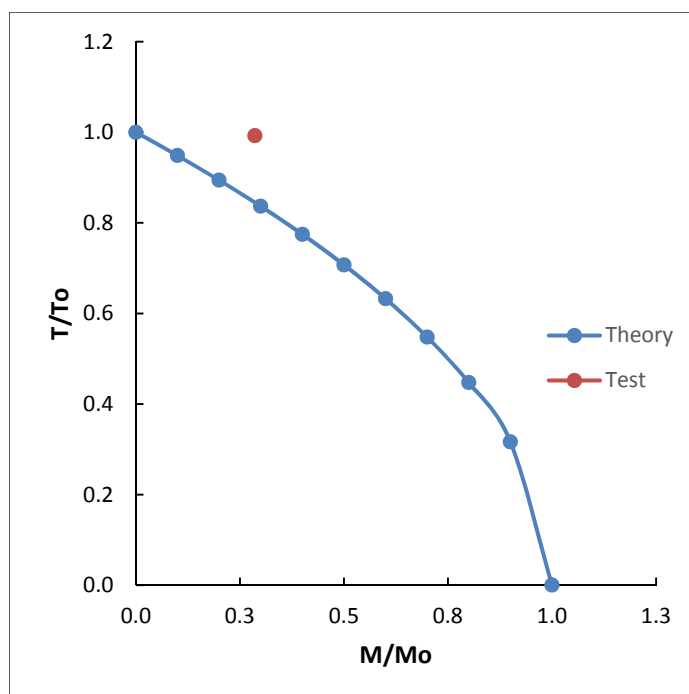


Figure 159. M-T interaction for SS03

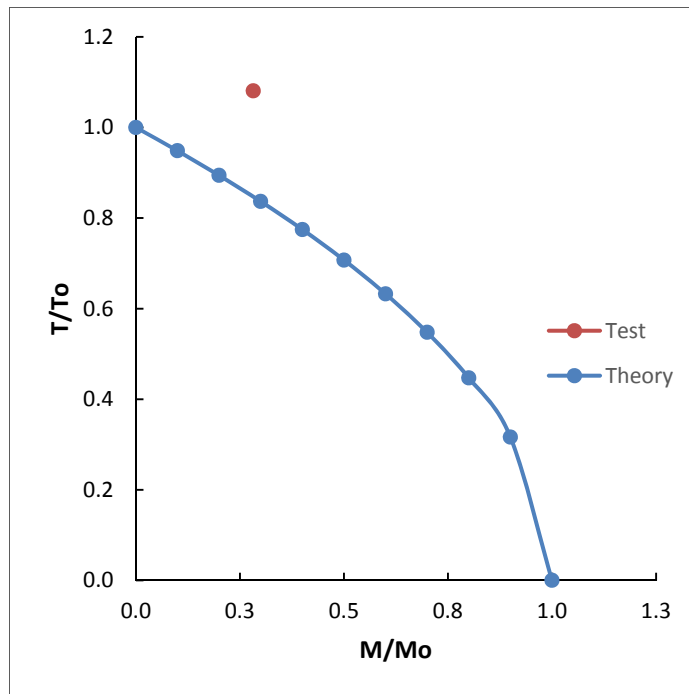


Figure 160. M-T interaction for SM07

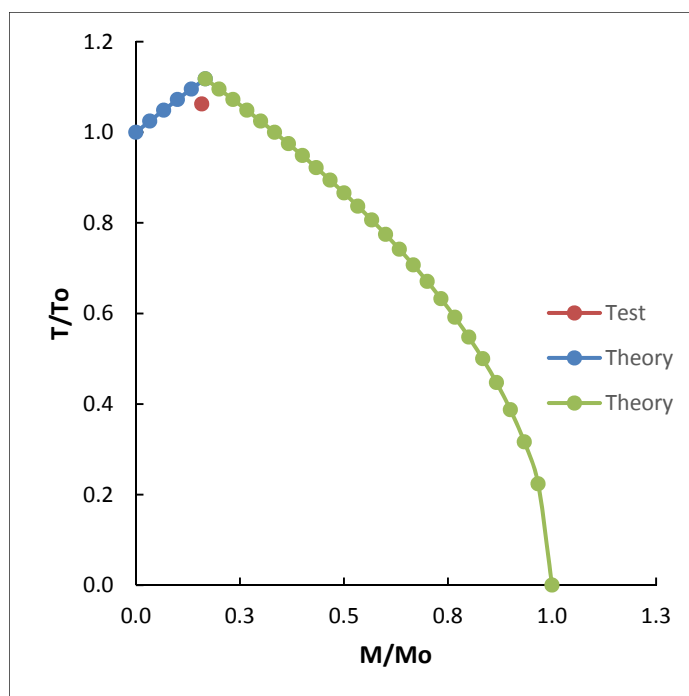


Figure 161. M-T interaction for SM10

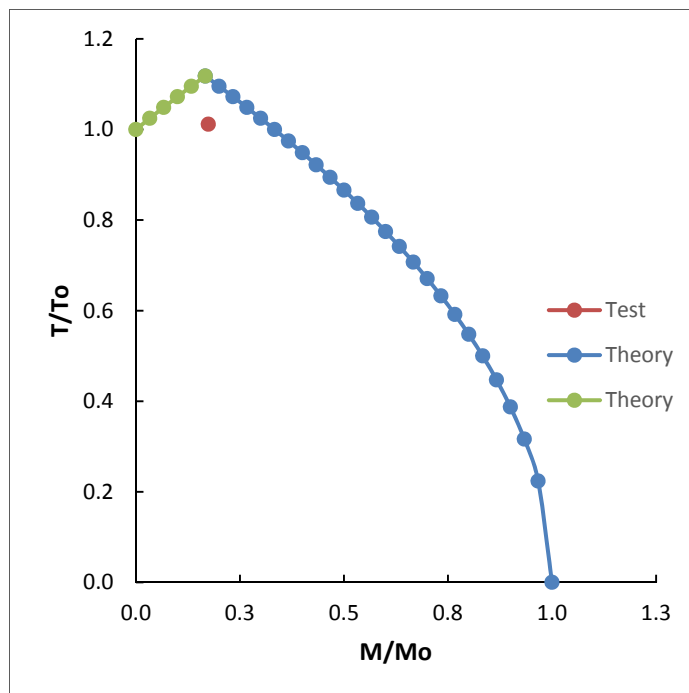


Figure 162. M-T interaction for SM12

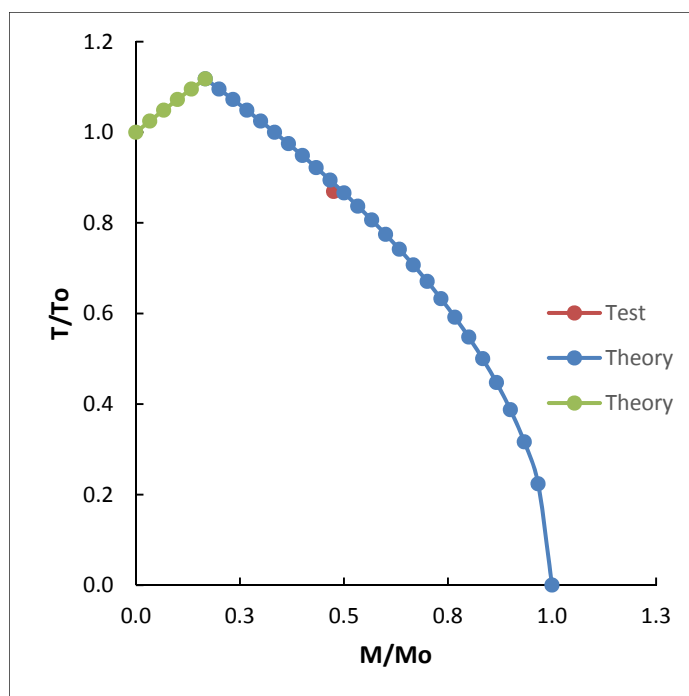


Figure 163. M-T interaction for SM13

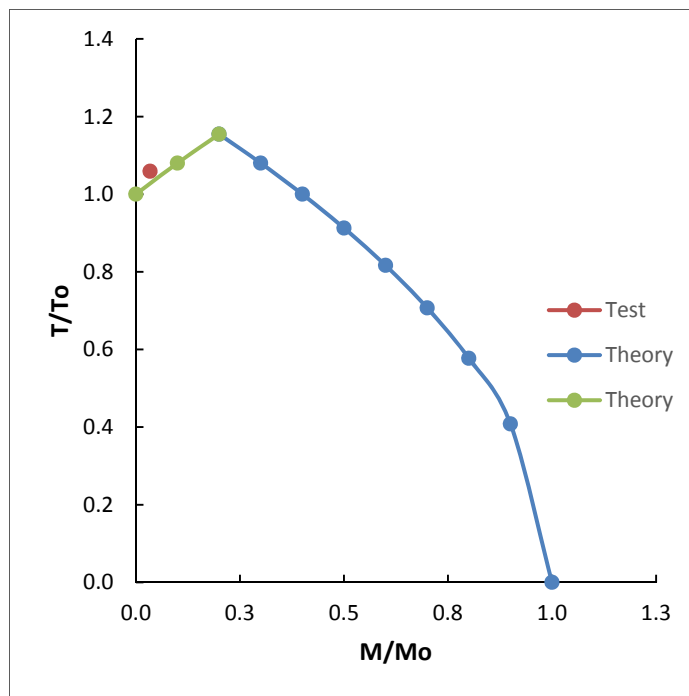


Figure 164. M-T interaction for SM15

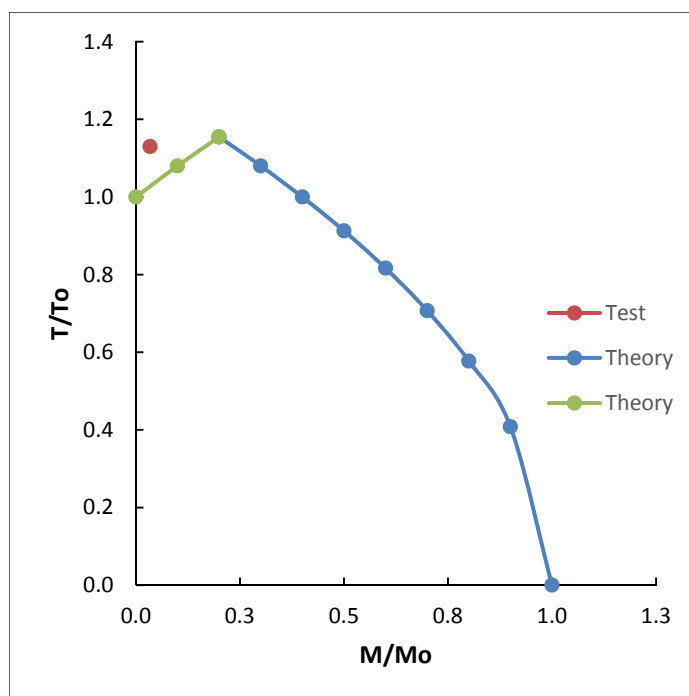


Figure 165. M-T interaction for SM16

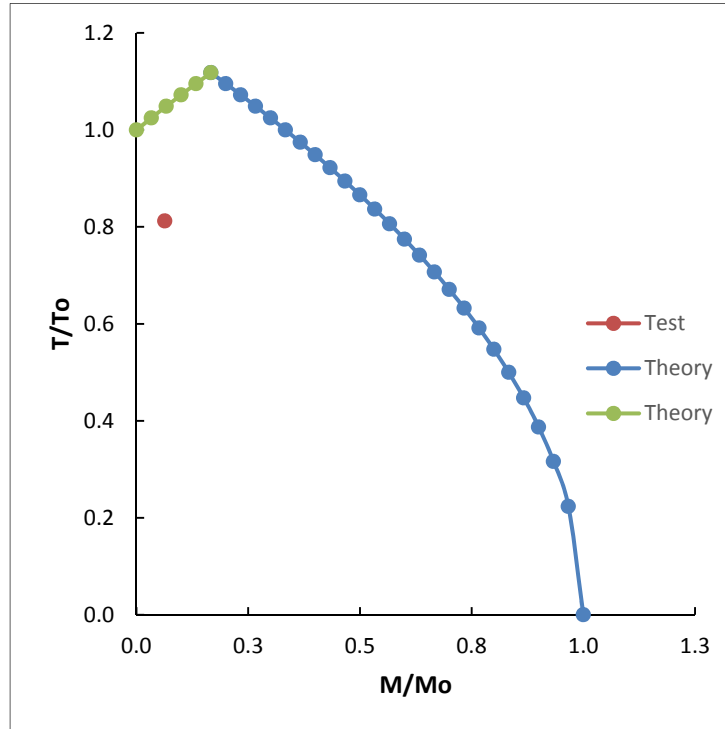


Figure 166. M-T interaction for SM17

Table 14 shows the summary of theoretical and experimental results for tests under combined bending and torsion. The maximum difference between theoretical and experimental values was found to be 19 percent in the case of SM19 whereas the minimum is 1 percent in case of SM10. The average of the differences is zero. The agreement of theory and experiments is good.

Table 14. Ultimate torsional strength under combined bending and torsion

Specimen	M_{applied} (k-in)	$T_{n,\text{test}}$ (k-in)	$T_{n,\text{calc}}$	$T_{n,\text{test}} / T_{n,\text{calc}}$
SM01	4.08	9.11	9.89	0.92
SM02	3.12	9.90	1083	0.91
SM03	6.00	13.82	0.96	1.07
SM07	3.84	5.15	4.76	1.08
SM10	2.40	5.43	5.11	1.06
SM12	2.64	5.12	5.06	1.01
SM13	7.20	4.40	4.30	1.02
SM15	3.60	6.61	6.02	1.06
SM16	3.60	7.89	6.98	1.13
SM19	3.60	4.67	5.75	0.81

4.6 Torque versus Angle of Twist Relations

The theoretical and experimental torque versus angle of twist relations are shown in Figure 167 through Figure 173. The predicted and tested strength values are in excellent agreement. However, the angle of twist values are slightly more in the experiments as compared to the calculated values for some specimens.

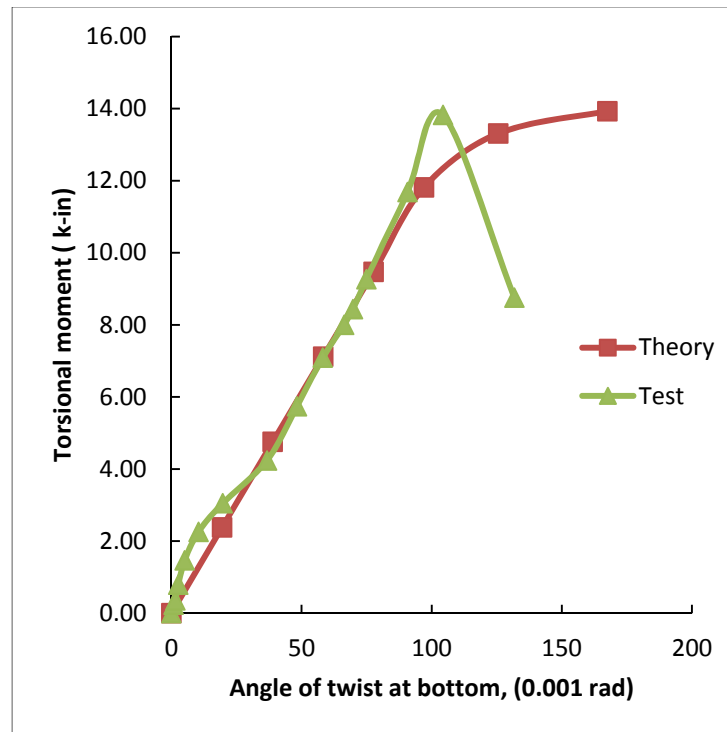


Figure 167. Torque versus angle of twist for SS03

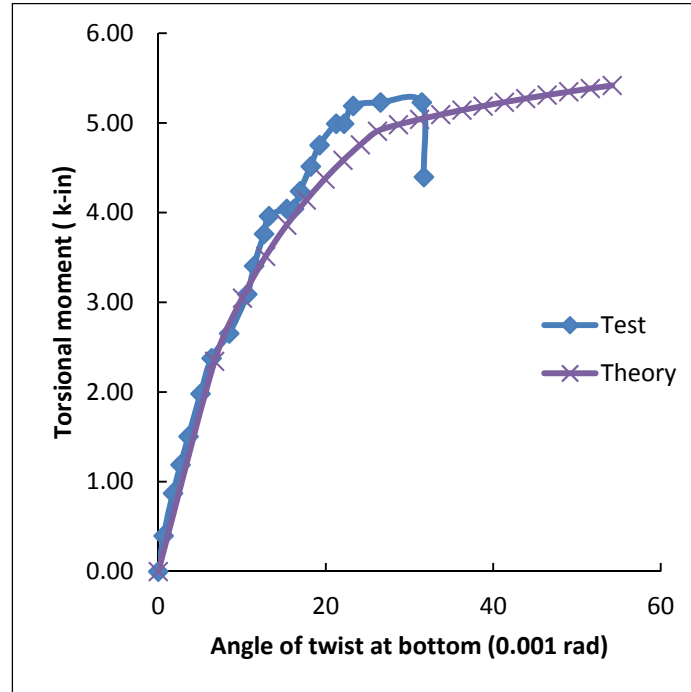


Figure 168. Torque versus angle of twist for SM05

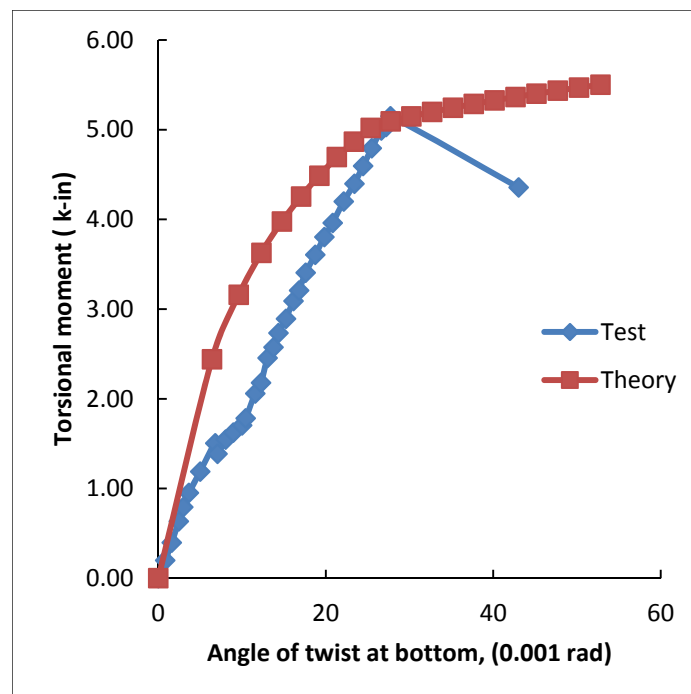


Figure 169. Torque versus angle of twist for SM07

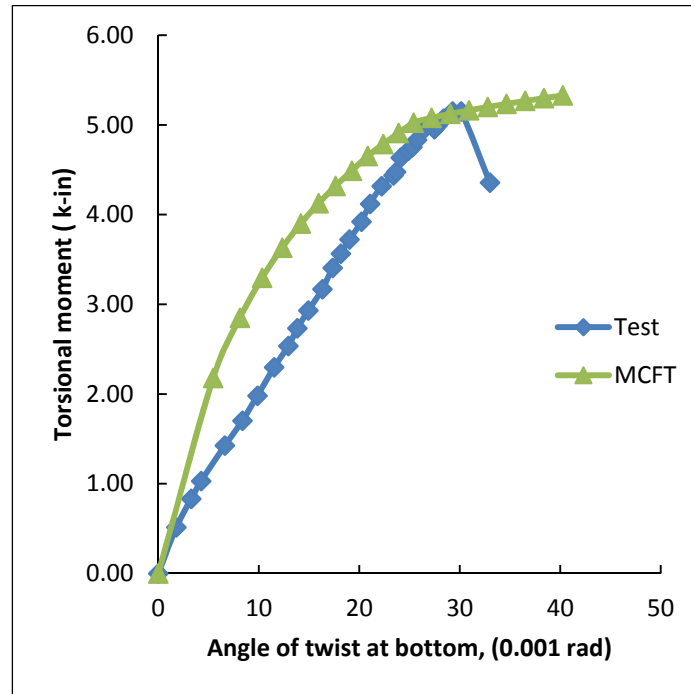


Figure 170. Torque versus angle of twist for SM08

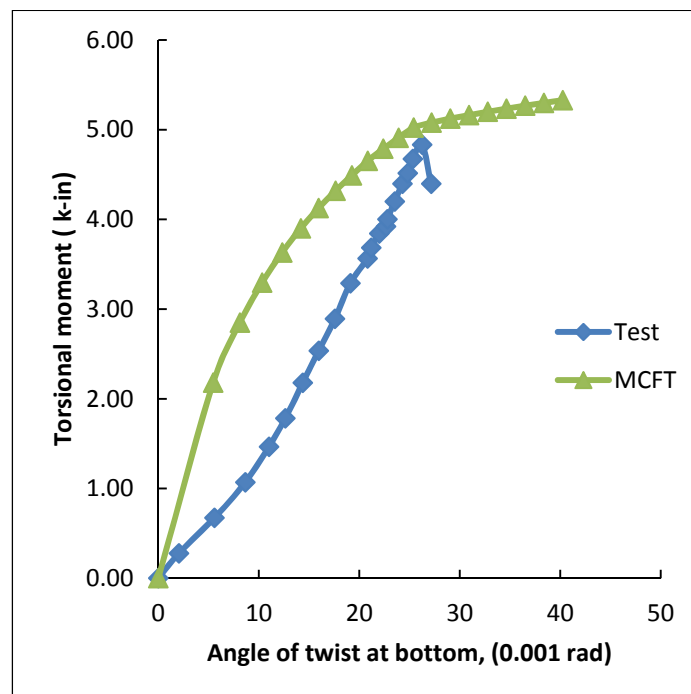


Figure 171. Torque versus angle of twist for SM11

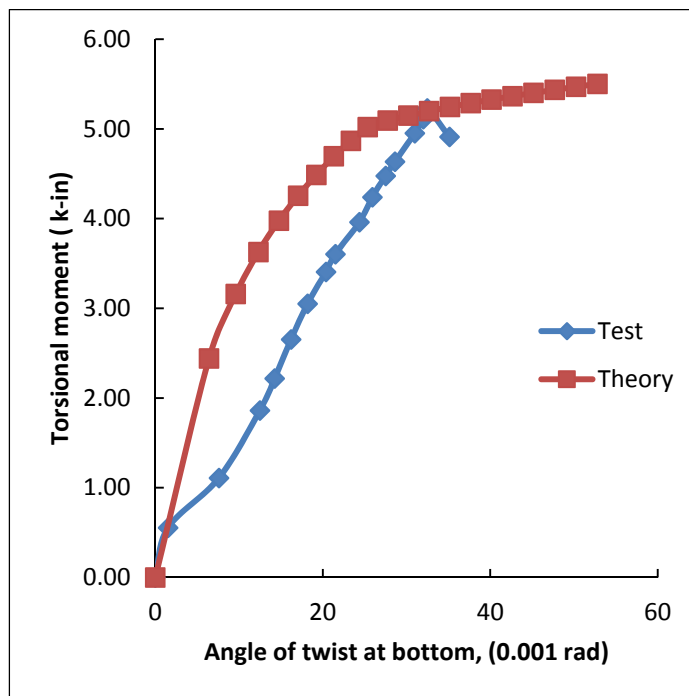


Figure 172. Torque versus angle of twist for SM14

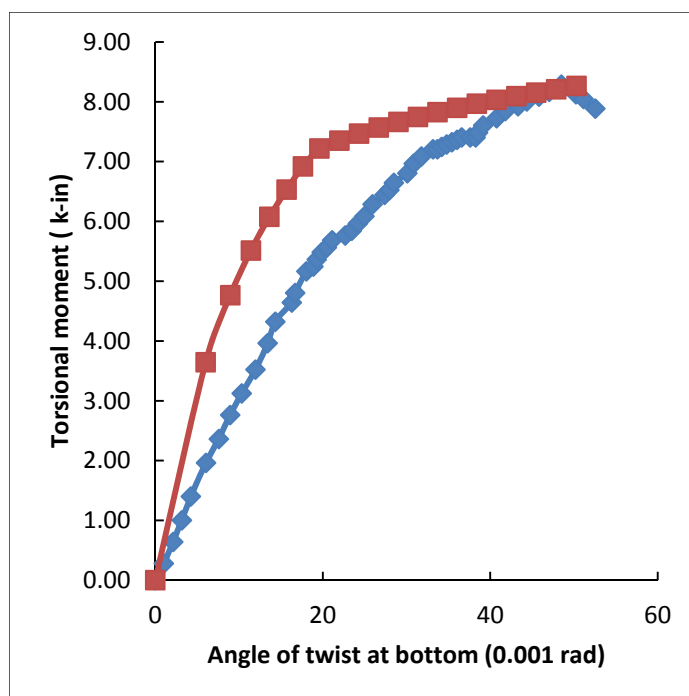


Figure 173. Torque versus angle of twist for SM16

4.7 Ultimate Load of Slab-beam Specimen

The ultimate load calculated for a slab-beam system along with test values is given in Table 15. The first two slab-beam systems failed due to cracking of the slabs so the ultimate load is calculated based on yield line theory. However, the final slab-beam system failed due to major cracking in the spandrel members so the bending-torsion interaction equation was used to find the ultimate load.

Table 15. Peak load of SL specimens

Specimen	$P_{n,test}$ (kips)	$P_{n,calc}$ (kips)	$P_{n,test}/P_{n,calc}$	Failure mode
SL01	27.24	29.03	0.94	Slab failure
SL02	17.80	19.24	0.93	Slab failure
SL03	17.77	16.16	1.10	SM failure

5. CONCLUSIONS AND FUTURE RESEARCH

5.1 Conclusions

Based on the study presented in this dissertation, the following main conclusions are drawn:

1. The materially nonlinear analysis, formulated and programmed, predicts the behavior and strength of both square and L-shaped members with reasonable degree of accuracy.
2. The bending capacity of L-shaped members is increased from 1.8 to 7 times by the application of an increased number of CFRP retrofitting strips at appropriate locations.
3. The location of CFRP strips for retrofitting plays an important role as exemplified through the use of six CFRP strips (SM15) which resulted in practically the same bending capacity as that obtained by using nine CFRP strips (SM16).
4. The modified ultimate strength torque-bending interaction expressions formulated to account for CFRP retrofitting predict the load-carrying capacities of the tested isolated members fairly accurately.
5. A comparison of the modified strength torque-bending interaction curves for CFRP retrofitted members to those based on ACI code for non-retrofitted members show a significant increase in the member load-carrying capacity.
6. The use of a rebar in the flange of an L-shaped section does not contribute significantly to the bending capacity due to its proximity to the neutral axis.
7. Two of the isolated spandrel members tested exhibited a localized failure at the location of the maximum applied bending moment owing to stress concentration effects near the top end gimbal.
8. In plain concrete members subjected to torsion, the cracks in the concrete penetrate across the member cross sections and divide the members into two pieces.
9. The failure under torsion in isolated spandrel members tested was observed to be sudden and brittle even for the members having steel reinforcement both with and without CFRP retrofitting.
10. For members with an L-shaped section, cracking starts at the flange-web junction near the bottom end of the member but failure is caused by an inclined crack near the top end passing through the flange width.

11. An addition of four longitudinal rebars in a member with L-shaped section resulted in a 50 percent increase in the ultimate torque capacity as compared with the plain concrete member.
12. The ultimate torque in combined bending and torsion tests was increased by 28 percent and 53 percent by the application of six and nine CFRP strips, respectively.
13. No de-bonding of CFRP strips from concrete members was observed during tests.
14. The slab with four spandrel members subjected to a single central concentrated load experienced major cracking in the slab without driving the spandrel members to their ultimate capacity.
15. When the slab with four spandrel members was subjected to a symmetrically-placed pair of concentrated loads applied at third-points, the dominant cracking occurred in the slab itself.
16. The spandrel members developed significant cracking only when a pair of concentrated loads was applied near the inner edge of the slab spandrel members.
17. The ultimate load-carrying capacity of the slab-beam systems under a single concentrated load as well as under a pair of third-point loads agreed well with those predicted using yield line theory.
18. The ultimate load-carrying capacity of the spandrel members in the slab-beam system was in good agreement with that predicted using flexural-torsional interaction expression when the concentrated loads were closer to the spandrel members.

5.2 Future Research

Future studies of reinforced concrete spandrel members can include the effect of an applied axial load along with bending and torsion. The behavior of RC members under cyclic torsion needs to be studied for application in earthquake-resistant structures.

REFERENCES

1. W. F. Chen, M.T.S., *Tangent stiffness method for biaxial bending of reinforced concrete columns*. 1972, Lehigh University.
2. Hsu, T. T. C., *Torsion of reinforced concrete / Thomas T. C. Hsu*. 1984: New York:Van Nostrand Reinhold, c1984.
3. Gere, J.M., *Mechanics of materials*. 2004: Belmont, CA:Thomson/Brooks/Cole, c2004. 6th ed.
4. Thomas, T. C. H., *Torsion of structural concrete-plain concrete rectangular sections*. ACI Special Publication 18.
5. Cowan, H. J. *An elastic theory for the torsional strength of rectangular reinforced concrete beams*. Magazine of Concrete Research, 1950. 2, 3-8 DOI: 10.1680/mac.1950.2.4.3.
6. Thomas, T. C. H., *Torsion of structural concrete-behavior of reinforced concrete rectangular members*. ACI Special Publication 18.
7. Hsu, T. C., *Ultimate torque of reinforced rectangular beams*. Journal of the Structural Division, 1968. 94: p. 485-510.
8. Nádai, A., *Theory of flow and fracture of solids*. Engineering Societies monographs. 1950: New York, McGraw-Hill, 1950-[63].
9. Joint ACI-ACCE Committee 445.1R-12: *Report on torsion in structural concrete*. Technical Documents.
10. McMullen, A. E. and H. R. Woodhead, *Experimental study of prestressed concrete under combined torsion, bending, and shear*. PCI Journal, 1973. 18(5): p. 85-100.
11. Kemp, E. L., M. A. Sozen, and C. P. Siess, *Torsion in reinforced concrete*. 1961, University of Illinois Urbana, Illinois.
12. Zia, P., *What do we know about torsion in concrete members*. Journal of the Structural Division.
13. Thomas, T. C. H., *Torsion of structural concrete-interaction surface for combined torsion, shear, and bending in beams without stirrups*. Journal Proceedings. 65(1).
14. McMullen, A. E. and J. Warwaruk, *The torsional strength of rectangular reinforced concrete beams subjected to combined loading*. 1967, Department of Civil Engineering, University of Alberta.
15. Onsongo, W. M., *The diagonal compression field theory for reinforced concrete beams subjected to combined torsion, flexure and axial load*, in *Department of Civil Engineering*. 1978, University of Toronto.: Toronto, ON, Canada.
16. Jian, Y., *Unified calculation method for symmetrically reinforced concrete section subjected to combined loading*. ACI Structural Journal, 2013. 110(6): p. 1121-1124.
17. David, J. V. and M. F. Phil, *Reinforced concrete T-beams without stirrups under combined moment and torsion*. Journal Proceedings. 65(1).

18. Lim, S. N. and M. S. Mirza, *Discussion of "Reinforced concrete T-beams without stirrups under combined moment and torsion"*, by D. J. Victor and P. M. Fergusson. ACI Journal 1968. 65(7): p. 560-563.
19. Zararis, P. D. and G. G. Penelis, *Reinforced concrete T-beams in torsion and bending*. Journal Proceedings. 83(1).
20. Hsu, T. C., *Torsion of reinforced concrete*. 1984, New York: Van Nostrand Reinhold Company Inc.
21. MacGregor, J. G. and M. G. Ghoneim, *Design for torsion*. Structural Journal. 92(2).
22. Lin, T. Y. and N. H. Burns, *Design of prestressed concrete structures / T. Y. Lin, Ned H. Burns*. 1981:New York:Wiley, c1981. 3d ed.
23. Ramanna-Sanjeeviah, N., *Static and impact response of reinforced concrete beams and slabs with and without NSM retrofitting using CFRP strips*, in *Civil and Environmental Old Dominion University*.
24. A.C.I. Institute., *Building code requirements for structural concrete*. 2011: Farmington Hills, MI.
25. Razzaq, Z. and W. W. McVinnie, *Theoretical and experimental behavior of biaxially loaded columns*. Journal of Structural Mechanics, 1986. 14(3).
26. Sanders, E. C., *Experimental investigation of steel angle column buckling and comparison to seven international design specifications*. 2009, Old Dominion University.
27. Zhao, Y., *Thermo-elasto-plastic behavior of biaxially loaded steel beam-columns inducing those from World Trade Center towers*. 2013, Old Dominion University:Norfolk. p. 222.
28. Konate, M., *Inelastic behavior and strength of steel beam-columns with applied Torsion*, in *Civil and Environmental Engineering*. 2015, Old Dominion University.
29. Popov, E.P., *Engineering mechanics of solids*. 2nd ed.. ed, ed. T.A. Balan. 1998, Upper Saddle River, N.J.:Prentice Hall.
30. ACI Committee 318, *318-11: Building code requirements for structural concrete and commentary*. 2014.
31. Ali, M. O., *Ultimate strength of reinforced concrete spandrel beams subjected to unsymmetrical bending*, in *Civil and Environmental Engineering*. 2006, Old Dominion University: VA, USA.
32. Chen, W. F. and M. T. Shoraka, *Tangent stiffness method for biaxial bending of reinforced concrete columns*. 1972, Lehigh Univeristy: Fritz Engineering Laboratory.
33. Connor, J. J., *Analysis of structural member systems*. 1976, New York: New York:Ronald Press Co.
34. Elfren, L., I. Karlsson, and A. Losberg, *Torsion-bending-shear-interaction for concrete beams*. ASCE Journal of the Structural Division, 1974. 100(ST8): p. 1657-1676.
35. Denis, M. and P. C. Michael, *Diagonal ompression field theory-A rational model For structural concrete in pure torsion*. Journal Proceedings. 71(8).

36. Bernardo, L. F. A., J. M. A. Andrade, and N. C. G. Nunes, *Generalized softened variable angle truss-model for reinforced concrete beams under torsion*. *Materials and Structures*, 2015. 48(7): p. 2169-2193.
37. Hsu, T.T.C., *Unified theory of concrete structures [e-book]*. 2nd ed..Y. L. Mo. 2010, Hoboken:John Wiley & Sons, Ltd.
38. William, L. G., *Moments in beam supported slabs*. *Journal Proceedings*. 69(3).

APPENDICES

A. ACI CODE PROVISIONS FOR TORSION

Introduction

The ACI [30] provisions for torsion are based on thin-walled tube, space truss analogy. The core concrete in a solid section is neglected. The torsional resistance is assumed to be provided by an outer tube roughly centered on closed stirrups. After cracking of concrete, the torsional resistance is provided primarily by closed stirrups and longitudinal rebars near the surface.

According to the thin-walled theory, the shear stress due to torsion T at any point along the perimeter of the tube having thickness t is given as:

$$\tau = \frac{T}{2A_o t} \quad (\text{A-1})$$

where A_o is the area enclosed by the path of the shear flow.

Cracking Torque

Cracking is assumed to occur when the maximum tensile stress reaches the value $4\sqrt{f'_c}$. In a pure torsion problem, the maximum tensile stress is equal to the shear stress produced by torsion. The wall thickness and area enclosed by the wall of the tube are assumed to be $0.75A_{cp}/p_{cp}$ and $2A_{cp}/3$ respectively. Substituting these values in Eq. (A-1) the cracking torsional moment is given as:

$$T_{cr} = 4\sqrt{f'_c} \left(\frac{A_{cp}^2}{p_{cp}} \right) \quad (\text{A-2})$$

Threshold Torsion

Torsion effects are neglected if the factored torsional moment T_u is less than the following threshold value:

$$T_{tt} = \phi \sqrt{f'_c} \left(\frac{A_{cp}^2}{P_{cp}} \right) \quad (\text{A-3})$$

Torques less than approximately one-quarter of the cracking torque do not cause a significant reduction in flexural and shear strengths of a member and can therefore be ignored. For instance, based on the interaction (approximately circular or elliptical) between a cracking torque and an inclined cracking shear of solid sections, a torque of $0.25T_{cr}$ corresponds to only a 3% reduction in the inclined cracking shear, therefore it is assumed to be negligible.

Reduction of Factored Torsional Moment

The factored torsional moment in case of compatibility torsion in a statically indeterminate structure can be reduced to the cracking torsion of the member as given below.

$$T_u = \phi 4 \sqrt{f'_c} \left(\frac{A_{cp}^2}{P_{cp}} \right) \quad (\text{A-4})$$

Requirement for Cross-Sectional Dimensions

The crushing of surface concrete due to inclined compressive stresses caused by shear and torsion is prevented by enforcing cross-sectional dimensions such that the following equation holds:

$$\sqrt{\left(\frac{V_u}{b_w d} \right)^2 + \left(\frac{T_u P_h}{1.7 A_{oh}^2} \right)^2} \leq \phi \left(\frac{V_c}{b_w d} + 8 \sqrt{f'_c} \right) \quad (\text{A-5})$$

Transverse Torsional Reinforcement

The transverse reinforcement to resist torsion is calculated based on the equation for nominal torsional strength given below:

$$T_n = \frac{2A_o A_t f_{yt}}{s} \cot \theta \quad (\text{A-6})$$

Rearranging this equation, the area of one leg of a closed stirrup to resist torsion is given as:

$$\frac{A_t}{s} = \frac{T_n}{2A_o A_t f_{yt} \cot \theta} \quad (\text{A-7})$$

In these equations, A_o is the gross area enclosed by shear flow path. It shall be determined by analysis or taken as $0.85A_{oh}$ where A_{oh} is the area enclosed by centerline of the outermost closed transverse torsional reinforcement. The angle θ is between concrete compression diagonals and tension chord of the member. Its value varies from 30° to 60° and can be assumed as 45° . The nominal torsion strength provided by concrete is taken as zero.

Longitudinal Torsional Reinforcement

The area of the additional longitudinal reinforcement to resist torsion shall not be less than:

$$A_t = \frac{A_t}{s} p_h \left(\frac{f_{yt}}{f_y} \right) \cot^2 \theta \quad (\text{A-8})$$

Here A_t/s is based on Eq. (A-7), irrespective of any modifications due to spacing requirements.

Minimum Torsion Reinforcement

When the factored torsion exceeds threshold value, a minimum area of closed stirrups shall be provided in all regions as computed by the following equation.

$$(A_v + 2A_t) = 0.75 \sqrt{f'_c} \frac{b_w s}{f_{yt}} \geq \frac{50 b_w s}{f_{yt}} \quad (\text{A-9})$$

Similarly a minimum area of longitudinal rebars shall also be provided as computed by the equation given below.

$$A_{t,\min} = \frac{5 \sqrt{f'_c} A_{cp}}{f_y} - \left(\frac{A_t}{s} \right) p_h \frac{f_{yt}}{f_y} \quad (\text{A-10})$$

where A_t/s shall not be taken less than $25b_w/f_{yt}$.

Maximum Spacing for Torsion Reinforcement

The maximum spacing for transverse torsion reinforcement is the smaller of $p_h/8$ and 12 in. The longitudinal bars shall be distributed around the inside perimeter of the stirrups with a maximum spacing of 12 in. There shall be at least one longitudinal bar in each corner of the stirrups. The diameter of the longitudinal bars shall be at least 0.042 times the stirrup spacing, but not less than 3/8 in.

Additional Requirements for Torsion

1. The yield strength of the rebars used as torsion reinforcement shall not exceed 60,000 psi.
2. The axial tension due to torsion is partly offset by compression in the flexural compression zone. Therefore it is permitted to reduce the area of longitudinal torsion reinforcement in this zone by $M_u / (0.9df_y)$.
3. Transverse torsional reinforcement shall be anchored by a 135 degree hook. A 90 degree hook is allowed if concrete surrounding the anchorage is restrained against spalling by another member.
4. Torsion reinforcement shall be provided for a distance of at least $(b_t + d)$ beyond the point required by the analysis.

B. ULTIMATE BENDING STRENGTH PROGRAM USING PATTERNS

```

%Program: Ultimate bending strength of L-shaped cross sections.
%Specimens: SM05, SM06, SM07
%Authors: Muhammad Fahim and Zia Razzaq
tic
clear; clc;
%-----
% Concrete Geometric Data
b=5;%total flange width
h=4;%total depth
bw=3;%width of web part
hf=2;%depth of flange/slab
bf=b-bw;%width of flange part
hw=h-hf;%depth of web part
n=1;%factor for calculating width of projected part of flange
beta=0.80;
%-----
% Concrete material Data
fc=5.765;%ksi
ecu=0.00398;%strain in concrete cylinder at failure
%-----
% Steel material Data
Es=29200;%ksi
fy=52.3;%ksi
ey=fy/Es;
%-----
% CFRP: data
a=0.63;%width
b_f=0.079;%thickness
Acf=a*b_f;%Area
fcfu=255.6;%Tensile strength.
Ecfu=20000;%Modulus of elasticity
ecfu=fcfu/Ecfu;%ultimate strain
%-----
% Iteration Data
p_un=0.01;%unbalanced axial force.
My_un=0.1;%unbalanced My
%-----
% Calculated Data
kxmax=(1+ ((hf*n*hf)/((h-hf)*(n*hf+bw))))/beta;
kymax=(1+(((h-hf)*bw)/(n*hf*h)))/beta;
%-----
% Start main program
num=0;
while~0
    num=num+1;
    for ky=0.001:0.001:kymax%Assume ky
        for teta=89.90:-0.01:0.01%Assume theta for each kx
            kx=ky*tan(teta*(pi/180));%Calculate kx.
        end
    end
%-----
% Limits to find Neutral Axis
x=(kx*(n*hf+bw))/ky; y=(ky*h)/kx;
x1=(hf*kx*(n*hf+bw))/(ky*h);
x2=(beta*kx*(n*hf+bw))-x1-bw;
x3=(beta*kx*(n*hf+bw))-x;
y1=(bw*ky*h)/(kx*(n*hf+bw));

```

```

y2=(beta*ky*h)-y1-hf;
y3=(beta*ky*h)-y;
y4=(y1*x3)/bw;
x4=(x1*y3)/hf;
%-----
% check for no tension region
if y2>=h-hf && y3>=hf && x2>=n*hf && x3>=bw
    disp('something is wrong')
    return
end
%-----
% Concrete: pattern 1
if beta*kx<=1 && beta*ky<=1 && x2<=0 && y2<=0
xbar=(beta*kx*((n*hf)+bw))/3;
ybar=(beta*ky*h)/3;
Pc=0.85*fc*0.5*(beta*kx*((n*hf)+bw))*(beta*ky*h);
Myc=Pc*xbar;
Mxc=Pc*ybar;
pattern=1;
end
%-----
%pattern 2
if beta*kx>1 && beta*ky<1 && y3>0 && y3<hf && x2<0 && y2<0
A11=(n*hf+bw)*y3;
A22=0.5*(n*hf+bw)*y;
x11=((n*hf)+bw)/2;
x22=((n*hf)+bw)/3;
y11=y3/2;
y22=y3+(y/3);
xbar=((A11*x11)+(A22*x22))/(A11+A22);
ybar=((A11*y11)+(A22*y22))/(A11+A22);
Pc=0.85*fc*((y3*((n*hf)+bw))+(0.5*((n*hf)+bw)*y));
Myc=Pc*xbar;
Mxc=Pc*ybar;
pattern=2;
end
%-----
% Upper rebars
nu=2;%No. of upper bars.
su=1.75;%spacing of upper bars
Abu=.05;%bar area of top beam rebars
cxu=0.625;%Concrete side cover
cyu=0.625;%Concrete bottom cover
Psu=0;%total axial force in upper rebars
Myu=0;%total My caused by upper bars
Mxu=0;%total Mx caused by upper bars
esU=zeros(1,nu);%Strain in the upper bars
fsU=zeros(1,nu);%Stress in the upper bar
for i=1:nu
eu=ecu*(1- ( cyu/(ky*h) ) - ( ((i-1)*su)+cxu)/((n*hf+bw)*kx) ) );
if eu>=ey
fsu=fy;
elseif ey>eu && eu>=-ey
fsu=eu*Es;
elseif eu<=-ey
fsu=-fy;

```



```

end
Fu=fsu*Abu;%force in each rebar
Psu=Psu+Fu;
Myu=Myu+Fu*((i-1)*su) + cxu);
Mxu=Mxu+Fu*cyu;
esU(i)=eu;
fsU(i)=fsu;
end
%-----
% Lower rebars
nL=2;%No. of lower bars.
sL=1.75;%spacing of lower bars
AbL=.05;%bar area of lower rebars
cxL=0.625;%Concrete side cover
cyL=0.625;%Concrete bottom cover
PsL=0;%total axial force in lower rebars
MyL=0;%total My caused by lower bars
MxL=0;%total Mx caused by lower bars
esl=zeros(1,nL);%Strain in the lower bars
fsl=zeros(1,nL);%Stress in the lower bar
for i=1:nL
eL=ecu*(1- ((h-cyL)/(ky*h) )- ((i-1)*sL+cxL) / (kx*(n*hf+bw)) );
if eL>=ey
fsl=fy;
elseif ey>eL && eL>-ey
fsl=eL*Es;
elseif eL<=-ey
fsl=-fy;
end
FL=fsl*AbL;%force in each rebar
PsL=PsL+FL;
MyL=MyL+FL*((i-1)*sL) + cxL);
MxL=MxL+FL*(h-cyL);
esl(i)=eL;
fsl(i)=fsl;
end
%-----
% Rebars in flange part
%-----
ns=0;%No. of lower bars.
ss=0;%spacing of lower bars
Abs=.05;%bar area of lower rebars
cxs=1;%Concrete side cover
cys=0.75;%Concrete bottom cover
Pss=0;%total axial force in lower rebars
Mys=0;%total My caused by lower bars
Mxs=0;%total Mx caused by lower bars
esS=zeros(1,nL);%Strain in the lower bars
fsS=zeros(1,nL);%Stress in the lower bar
for i=1:ns
es=ecu*(1-(((i-1)*ss)+(bw+cxs))/(kx*((n*hf)+bw))-((hf-cys)/(ky*h)));
if es>=ey
fss=fy;
elseif ey>es && es>-ey
fss=es*Es;
elseif es<=-ey

```

```

fss=-fy;
end
Fs=fss*Abs;%force in each rebar
Pss=Pss+Fs;
Mys=Mys+Fs*( bw +( (i-1)*ss +cxs) );
Mxs=Mxs+Fs*(hf-cys);
esS(i)=es;
fsS(i)=fss;
end
%-----
% CFRP: bw face
nbw=0;%No of strips
sbw=bw-a;%Spacing between strips
xbw=a/2;%x coordinate of first strip
ybw=h;%y coordinate of first strip
Pbw=0;%total axial force due to CFRP on bw
Mybw=0;%total My due to CFRP on bw
Mxbw=0;%total Mx due to CFRP on bw
efbw=zeros(1,2);
ffbw=zeros(1,2);
for i=1:nbw
ebw=ecu*(1- ( (ybw)/(ky*h) )- ( (i-1)*sbw+xbw) / (kx*(n*hf+bw)) );
if ebw>=ecfu
fbw=0;
elseif ecfu>ebw && ebw>-ecfu
fbw=ebw*Ecfu;
elseif ebw<=-ecfu
fbw=0;
end
Fbw=fbw*Acf;%force in each strip
Pbw=Pbw+Fbw;
Mybw=Mybw+Fbw*( (i-1)*sbw + xbw );
Mxbw=Mxbw+Fbw*ybw;
efbw(i)=ebw;
ffbw(i)=fbw;
end
%-----
% CFRP: hw face
nhw=0;%No of strips
shw=hw-a;%Spacing between strips
xhw=bw;%x coordinate of first strip
yhw=hf+a/2;%y coordinate of first strip
Phw=0;%total axial force due to CFRP on bw
Myhw=0;%total My due to CFRP on bw
Mxhw=0;%total Mx due to CFRP on bw
efhw=zeros(1,nhw);
ffhw=zeros(1,nhw);
for i=1:nhw
ehw=ecu*(1- ( ( (i-1)*shw+yhw)/(ky*h) ) - (xhw)/(kx*(n*hf+bw)) );
if ehw>=ecfu
fhw=0;
elseif ecfu>ehw && ehw>-ecfu
fhw=ehw*Ecfu;
elseif ehw<=-ecfu
fhw=0;
end

```

```

Fhw=fhw*Acf;%force in each strip
Phw=Phw+Fhw;
Myhw=Myhw+Fhw*xhw;
Mxhw=Mxhw+Fhw*( (i-1)*shw+yhw);
efhw(i)=ehw;
ffhw(i)=fhw;
end
%-----
% CFRP: bf face
nbf=0;%No of strips
sbf=bf-a;%Spacing between strips
xbf=bw+a/2;%x coordinate of first strip
ybf=hf;%y coordinate of first strip
Pbf=0;%total axial force due to CFRP on bw
Mybf=0;%total My due to CFRP on bw
Mxbf=0;%total Mx due to CFRP on bw
efbf=zeros(1,nbf);
ffbf=zeros(1,nbf);
for i=1:nbf
ebf=ecu*(1- ( (ybf)/(ky*h) )- ((i-1)*sbf+xbf) / (kx*(n*hf+bw)) );
if ebf>=ecfu
fbf=0;
elseif ecfu>ebf && ebf>-ecfu
fbf=ebf*Ecfu;
elseif ebf<=-ecfu
fbf=0;
end
Fbf=fbf*Acf;%force in each strip
Pbf=Pbf+Fbf;
Mybf=Mybf+Fbf*( (i-1)*sbf + xbf );
Mxbf=Mxbf+Fbf*ybf;
efbf(i)=ebf;
ffbf(i)=fbf;
end
%-----
% CFRP: hf face
%None installed in any specimen
%-----
% CFRP: b face
nbb=0;%No of strips
sbb=b-a;%Spacing between strips
xbb=a/2;%x coordinate of first strip
ybb=0;%y coordinate of first strip
Pbb=0;%total axial force due to CFRP on bw
Mybb=0;%total My due to CFRP on bw
Mxbb=0;%total Mx due to CFRP on bw
efbb=zeros(1,nbb);
ffbb=zeros(1,nbb);
for i=1:nbb
ebb=ecu*(1- ( (ybb)/(ky*h) )-((i-1)*sbb+xbb)/(kx*(n*hf+bw)));
if ebb>=ecfu
fbb=0;
elseif ecfu>ebb && ebb>-ecfu
fbb=ebb*Ecfu;
elseif ebb<=-ecfu
fbb=0;

```

```

end
Fbb=fbb*Acf;%force in each strip
Pbb=Pbb+Fbb;
Mybb=Mybb+Fbb*( (i-1)*sbb + xbb );
Mxbb=Mxbb+Fbb*ybb;
efbb(i)=ebb;
ffbb(i)=fbb;
end
%-----
% CFRP: h face
nhh=0;%No of strips
shh=0;%Spacing between strips
xhh=0;%x coordinate of first strip
yhh=h/2;%y coordinate of first strip
Phh=0;%total axial force due to CFRP on bw
Myhh=0;%total My due to CFRP on bw
Mxhh=0;%total Mx due to CFRP on bw
efhh=zeros(1,nhh);
ffhh=zeros(1,nhh);
for i=1:nhh
ehh=ecu*(1- ( ( (i-1)*shh+yhh)/(ky*h) ) - (xhh)/(kx*(n*hf+bw)) );
if ehh>=ecfu
fhh=0;
elseif ecfu>ehh && ehh>=-ecfu
fhh=ehh*Ecfu;
elseif ehh<=-ecfu
fhh=0;
end
Fhh=fhh*Acf;%force in each strip
Phh=Phh+Fhh;
Myhh=Myhh+Fhh*xhh;
Mxhh=Mxhh+Fhh*( (i-1)*shh+ yhh );
efhh(i)=ehh;
ffhh(i)=fhh;
end
%-----
% Calculate actions
Pt=Pc+Psu+Psl+Pss+Pbw+Phw+Pbf+Pbb+Phh;
Myt=Myc+Myu+MyL+Mys+Mybw+Myhw+Mybf+Mybb+Myhh ;
%-----
% Equilibrium check
if abs(Pt) < p_un && abs(Myt) < My_un
Mxt=Mxc+Mxu+MxL+Mxs+Mxbw+Mxhw+Mxbf+Mxbb+Mxhh;
break
end
end%-----end of for loop for teta
if abs(Pt) < p_un && abs(Myt) < My_un,break,end
end%-----end of for loop for kx.
if abs(Pt) < p_un && abs(Myt) < My_un,break,end
end%end of while loop
%-----
% Output
Beta=90-(180/pi)*atan((kx*b)/(ky*h));
phiy=(ecu/(ky*h*sin(teta*pi/180)))*sin((Beta)*pi/180);
phix=(ecu/(ky*h*sin(teta*pi/180)))*cos((Beta)*pi/180);
if kx*b > b

```

```
        y2=(kx*b-b)*tan((Beta)*(pi/180));
else
    y2=0;
end
disp('Axial force = ')
disp(Pt)
disp('My = ')
disp(Myt)
disp('Mux = ')
disp(-Mxt)
disp('Curvature about x-axis (rad/in) = ')
disp(phix)
disp('pattern = ')
disp(pattern)
disp('Beta = ')
disp(Beta)
disp('Y1 = ')
disp(ky*h)
disp('Y2 = ')
disp(y2)
disp('Width of NA = ')
disp(kx*b)
toc
```

C. MOMENT-CURVATURE PROGRAM USING TANGENT STIFFNESS METHOD

```

%Program: Moment-curvature plots
%Specimens: SM16
%Authors: Muhammad Fahim and Zia Razzaq
tic
clear;
clc;
%-----
% Concrete Geometric Data
bf=5;%flange width in inches
hf=2;%flange depth in inches
hw=4;%Web depth in inches
bw=3;%Web Width in inches
cr=0.625;%cover to main rebar center.
cc=0.25;%clear cover
%-----
% Concrete material Data
k1=0.85;%Constant as in Whitney block.
fcP=5.765;%Concrete compressive strength.
ecP=0.00362;%Concrete strain corresponding to ultimate strength.
ecu=0.00398;%Ultimate strain of concrete.
%-----
% Steel Geometric Data
Ns=4;%Number of reinforcement rebars.
Ab=0.05;%Area of one rebar.
%-----
% Steel material Data
fy=52.3;
Es=29200;
%-----
% CFRP Data
a=0.63;%width
b=0.079;%thickness
Acf=a*b;%Area
fcfu=255.6;%Tensile strength.
Ecfu=20000;%Modulus of elasticity
ecfu=fcfu/Ecfu;%ultimate strain
%-----
% CFRP Coordinates:9 strips
xcf1=a/2;ycf1=hw;
xcf2=bw-a/2;ycf2=hw;
xcf3=bw;ycf3=hw-a/2;
xcf4=bw;ycf4=hf+a/2;
xcf5=bw+a/2;ycf5=hf;
xcf6=bf-a/2;ycf6=hf;
xcf7=bf-a/2;ycf7=0;
xcf8=a/2;ycf8=0;
xcf9=0;ycf9=hw/2;
xcf10=0;ycf10=0;
xcf=[xcf1 xcf2 xcf3 xcf4 xcf5 xcf6 xcf7 xcf8 xcf9 xcf10];
ycf=[ycf1 ycf2 ycf3 ycf4 ycf5 ycf6 ycf7 ycf8 ycf9 ycf10];
%-----
% Iteration Data
Nh=400;%Number of layers along depth,along y.
Nb=500;%Number of layers along width, along x.
Nhs=2;%for rebars

```

```

Nbs=2;%for rebars
del_Mx=0.24; %Interval for external Mx
iter=100;%Max. No. of iterations of while loop.
%-----
% Calculated data
Ag=bf*hf+bw*(hw-hf);%Gross cross sectional area of concrete.
Nc=Nh*Nb;%Number of small area elements.
delAc=(hw/Nh)*(bf/Nb);%Elemental concrete area
klfcP=kl*fcP;%Concrete ultimate strength.
Ec=(57600/1000)*sqrt(fcP*1000); %Modulus of elasticity of concrete.
fr=(1/1000)*7.5*sqrt(fcP*1000);%Modulus of rupture/Tensile strength of
concrete.
er1=0.5*(2*ecP+2*sqrt( ((ecP^2)) -((ecP^2)*fr/fcP) ));
er2=0.5*(2*ecP-2*sqrt( ((ecP^2)) -((ecP^2)*fr/fcP) ));
er=min(er1,er2);
ey=fy/Es;
Ast=(Ns/2)*Ab;%Top reinforcement area
Asb=(Ns/2)*Ab;%bottom reinforcement area.
As=Nb*Ab;%Total rebars area
%-----
% Normalizing factors
Ixo=(bw*hw^3)/12;%MOI of a rectangle without the flange.
yo=hw/2;
Mo=(fr*Ixo)/yo;
phio=0.5*hw*er;
%-----
% Centroids of elemental areas: Origin is assumed at the upper left corner.
xi=zeros(Nh,Nb);%Centroid of elemental area along x axis.
yj=zeros(Nh,Nb);%Centroid of elemental area along y axis.
for i=1:Nh;
for j=1:Nb;
xi(i,j)=(bf/(2*Nb))+(j-1)*(bf/Nb);
yj(i,j)=(hw/(2*Nh))+(i-1)*(hw/Nh));
if xi(i,j)> bw && yj(i,j)>(hw-hf)
xi(i,j)=0;
yj(i,j)=0;
else
xi(i,j)=xi(i,j);
yj(i,j)=yj(i,j);
end
end
end
%-----
% Distances of rebars from origin
xr=zeros(Nhs,Nbs);%Distance of steel bars along x.
yr=zeros(Nhs,Nbs);%Distance of steel bars along y.
nb=(Ns/4)+1;%Number of bars along each side of the cross section.
row=round(linspace(1,Nhs,nb));%Bars location in the matrix along y axis.
col=round(linspace(1,Nbs,nb));%Bars location in the matrix along x axis.
s1=zeros(length(row),1);%Position of the bars without cover along the depth.
s2=zeros(length(col),1);%Position of the bars without cover along the width.
for i = 1:length(row)
s1(i) = ((hw-2*cr)*(i-1))/(nb-1));
end
for i = 1:length(col)
s2(i) = ((bw-2*cr)*(i-1))/(nb-1));

```

```

end
xr(1,col)=cr+s2;%First row of bars along x axis.
xr(Nhs,col)=cr+s2;%Last row of bars along x axis.
xr(col(2:length(col)-1),1)=cr;%First Column of bars along x axis.
xr(col(2:length(col)-1),Nbs)=bw-cr;%Last Column of bars along x axis.
yr(row,1)= cr + s1;%First Column of bars along y axis.
yr(row,Nbs)= cr + s1;%Last Column of bars along y axis.
yr(1, row(2:length(row)-1)) = hw-cr;%First Row of bars along y axis.
yr(Nhs,row(2:length(row)-1)) = cr;%Last Row of bars along y axis.
%-----
% TS Matrix assuming zero stress/strains on the cross section.
eci=zeros(Nh,Nb);%strains in each concrete element.
Eci=zeros(Nh,Nb);%MOE of each concrete element.
fci=zeros(Nh,Nb);%stress in each concrete element.
esr=zeros(Nhs,Nbs);%strains in each rebar.
Esr=zeros(Nhs,Nbs);%stress in each rebar.
fsr=zeros(Nhs,Nbs);%MOE of reach rebar.
ecri=zeros(Nhs,Nbs);
fcri=zeros(Nhs,Nbs);
Ecri=zeros(Nhs,Nbs);
ecf=zeros(1,length(xcf));
fcf=zeros(1,length(xcf));
Ecf=zeros(1,length(xcf));
for i = 1:Nh
    for j = 1:Nb
        if xi(i,j)~=0
            Eci(i,j)=fcP*((2/ecP)-((2*eci(i,j))/(ecP^2)));
        else
            Eci(i,j)=0;
        end
    end
end
for i = 1:Nhs
    for j = 1:Nbs
        Esr(i,j)=Es;
        Ecri(i,j)=fcP*((2/ecP)-((2*esr(i,j))/(ecP^2)));
    end
end
for i = 1:length(xcf)
    Ecf(i)=Ecfu;
end
k11=sum(sum(Eci))*delAc+sum(sum(Esr))*Ab +sum(Ecf)*Acf -sum(sum(Ecri))*Ab;
k12=-(sum(sum(xi.*Eci))*delAc-(sum(sum(xr.*Esr))*Ab-sum(xcf.*Ecf)*Acf +
sum(sum(xr.*Ecri))*Ab;
k13=-(sum(sum(yj.*Eci))*delAc-(sum(sum(yr.*Esr))*Ab-sum(ycf.*Ecf)*Acf +
sum(sum(yr.*Ecri))*Ab;
k21=k12;
k22=sum(sum((xi.^2).*Eci))*delAc+sum(sum((xr.^2).*Esr))*Ab
+sum((xcf.^2).*Ecf)*Acf-sum(sum((xr.^2).*Ecri))*Ab;
k23=sum(sum((xi.*yj).*Eci))*delAc+sum(sum((xr.*yr).*Esr))*Ab+sum((xcf.*ycf).*
Ecf)*Acf -sum(sum((xr.*yr).*Ecri))*Ab;
k31=k13;
k32=k23;
k33=sum(sum((yj.^2).*Eci))*delAc+sum(sum((yr.^2).*Esr))*Ab+sum((ycf.^2).*Ecf)
*Acf -sum(sum((yr.^2).*Ecri))*Ab;

```



```

K=[k11,k12,k13;k21,k22,k23;k31,k32,k33];
%-----
% Main program
Mx(1)=0;
phix(1)=0;%Total curvature about x axis.
Vd=[0;0;0];%Initial displacement vector.
Vf=[0;0;0];%Initial force vector.
Deto=det(K);
Det(1)=det(K);
N = 2;%Counter
while ~0
DMxe=del_Mx;%D for delta. increment in external Mx.
DVf=[0;0;DMxe];%Change in force vector.
DVd=K\DVf;%Change in displacement vector.
Vf=Vf + DVf;
Vd=Vd + DVd;
m = 0;
while m < iter
m=m+1;%Counter for number of iterations.
%-----
% Strains in concrete elements
for i = 1:Nh
for j = 1: Nb
    eci(i,j)= -xi(i,j)*Vd(2,1) - yj(i,j)*Vd(3,1);

if eci(i,j) ~= 0
    eci(i,j)=eci(i,j)+Vd(1,1);
else
    eci(i,j)=0;
end
%1.Element cracked in Tension
if eci(i,j) < 0 && eci(i,j) < -er
    fci(i,j)=0;
    Eci(i,j)=0;
%2.Element uncracked in Tension
elseif eci(i,j) < 0 && eci(i,j) >= -er
    fci(i,j)=fcP*((2*eci(i,j)/ecP)-((eci(i,j)/ecP)^2));%stress in each
concrete element.
    Eci(i,j)=fcP*((2/ecP)-((2*eci(i,j))/(ecP^2)));%MOE of each concrete
element.
%3.Element in compression
elseif eci(i,j)>0 && eci(i,j) <= ecu
    fci(i,j)=fcP*((2*eci(i,j)/ecP)-((eci(i,j)/ecP)^2));%stress in each
concrete element.
    Eci(i,j)=fcP*((2/ecP)-((2*eci(i,j))/(ecP^2)));%MOE of each concrete
element.
%4.Element has crushed in compression
else
    Eci(i,j)=0;
    fci(i,j)=0;
end
end%end of i for loop.
end%end of j for loop.
%-----
% Strains in steel elements
for i = 1:Nhs

```

```

for j = 1: Nbs
esr(i,j)=Vd(1,1)-xr(i,j)*Vd(2,1)-yr(i,j)*Vd(3,1);
%1.Element yielded in Tension
if esr(i,j)< 0 && esr(i,j) < -ey
    fsr(i,j)=-fy;
    Esr(i,j)=0;
%2.Element elastic in Tension
elseif esr(i,j) < 0 && esr(i,j) >= -ey
    Esr(i,j)=Es;
    fsr(i,j)=Esr(i,j)*esr(i,j);
%3.Zero araa elements
elseif esr(i,j)==0
    fsr(i,j)=0;
    Esr(i,j)=0;
%4.Element elastic in compression
elseif esr(i,j) > 0 && esr(i,j) <= ey
    Esr(i,j)=Es;
    fsr(i,j)=Esr(i,j)*esr(i,j);
%5.Element plastic in compression
else
    fsr(i,j)=fy;
    Esr(i,j)=0;
end
end%end of i for loop.
end%end of j for loop.
%-----
% Concrete elements at location of rebars
for i = 1:Nhs
for j = 1: Nbs
%1.Element cracked in Tension
if esr(i,j) < 0 && esr(i,j) < -er
    fcric(i,j)=0;
    Ecric(i,j)=0;
%2.Element uncracked in Tension
elseif esr(i,j) < 0 && esr(i,j) >= -er
    fcric(i,j)=fcP*((2*esr(i,j)/ecP)-((esr(i,j)/ecP)^2));%stress in each
concrete element.
    Ecric(i,j)=fcP*((2/ecP)-((2*esr(i,j))/(ecP^2)));%MOE of each concrete
element.
%3.Element in compression
elseif esr(i,j)>0 && esr(i,j) <= ecu
    fcric(i,j)=fcP*((2*esr(i,j)/ecP)-((esr(i,j)/ecP)^2));%stress in each
concrete element.
    Ecric(i,j)=fcP*((2/ecP)-((2*esr(i,j))/(ecP^2)));%MOE of each concrete
element.
%4.Element has crushed in compression
else
    Ecric(i,j)=0;
    fcric(i,j)=0;
end
end%end of i for loop.
end%end of j for loop.
%-----
%Find Strains and stress in CFRP Strips.
for i = 1:length(xcf)
    if xcf(i) ~=0 || ycf(i) ~=0

```

```

        ecf(i)=Vd(1,1)- xcf(i)*Vd(2,1)-ycf(i)*Vd(3,1);
    if ecf(i)>= -ecfu && ecf(i) <=ecfu
        Ecf(i)=Ecfu;
        fcf(i)=Ecfu*ecf(i);
    else
        fcf(i)=0;
        Ecf(i)=0;
    end
else
    ecf(i)=0;
    fcf(i)=0;
    Ecf(i)=0;
end
end

end

%if min(min(eci))< -er || m >= iter, break,end %To find cracking moment
if max(max(eci))> ecu,break,end
%-----
% Stiffness matrix
k11=sum(sum(Eci))*delAc+sum(sum(Esr))*Ab +sum(Ecf)*Acf -sum(sum(Ecri))*Ab;
k12=- (sum(sum(xi.*Eci))*delAc-(sum(sum(xr.*Esr))*Ab-sum(xcf.*Ecf)*Acf +
sum(sum(xr.*Ecri))*Ab);
k13=- (sum(sum(yj.*Eci))*delAc-(sum(sum(yr.*Esr))*Ab-sum(ycf.*Ecf)*Acf +
sum(sum(yr.*Ecri))*Ab);
k21=k12;
k22=sum(sum((xi.^2).*Eci))*delAc+sum(sum((xr.^2).*Esr))*Ab
+sum((xcf.^2).*Ecf)*Acf - sum(sum((xr.^2).*Ecri))*Ab;
k23=sum(sum((xi.*yj).*Eci))*delAc+sum(sum((xr.*yr).*Esr))*Ab+sum((xcf.*ycf).*
Ecf)*Acf -sum(sum((xr.*yr).*Ecri))*Ab;
k31=k13;
k32=k23;
k33=sum(sum((yj.^2).*Eci))*delAc+sum(sum((yr.^2).*Esr))*Ab+sum((ycf.^2).*Ecf)
*Acf -sum(sum((yr.^2).*Ecri))*Ab;
K=[k11,k12,k13;k21,k22,k23;k31,k32,k33];
%-----
% Find actions
Mxe=Vf(3,1);
Pn=((sum(sum(fci))*delAc)+((sum(sum(fsr))*Ab)+sum(fcf)*Acf-
sum(sum(fcricri))*Ab);
Myn=-((sum(sum(xi.*fci))*delAc)-((sum(sum(xr.*fsr))*Ab)-sum(xcf.*fcf)*Acf
+sum(sum(fcricri))*Ab);
Mxn=-((sum(sum(yj.*fci))*delAc)-((sum(sum(yr.*fsr))*Ab)-sum(ycf.*fcf)*Acf
+((sum(sum(yr.*fcricri))*Ab));
%-----
% Equilibrium Check
if abs(Pn) <= 0.001 && abs(Myn)<=0.1 && abs(Mxe-Mxn) <=
0.1*max(0.1,0.002*Mxe)
phix(N)=Vd(3,1);%/phio;
Mx(N)=Mxn;%/Mo;
Det(N)=det(K);
N=N+1;
ecif=eci;
fcif=fci;
esrf=esr;
fsrf=fsr;
fecf=ecf;

```

```

ffcf=fcf;
break%end while loop.
else
%-----
% Unbalanced actions
UVf= [-Pn;-Myn;Mxe-Mxn];
UVd=K\UVf;
Vd=Vd+UVd;
end%end of Equilibrium check.
end%end of while loop.
%-----
% Stopping criteria:Concrete compressive strain reaches limiting value.
%-----
if max(max(eci))> ecu || m >= iter, break,end
end%end of for loop for Mx.
%-----
% Output
[I,J]=find(ecif>0);
y1=(hw/Nh)*(max(I));
y2=(hw/Nh)*I(end);
Beta=(180/pi)*atan((y1-y2)/bf);
plot(phix,Mx)
disp('max concrete compressive strain = ')
disp(max(max(ecif)))
disp('Beta = ')
disp(Beta)
disp('Y1 = ')
disp(y1)
disp('Y2 = ')
disp(y2)
disp('Max Mx (k-in) = ')
disp(max(Mx))
disp('Max curvautre about x-axis(rad/in) = ')
disp(max(phix))
toc

```

D. MOMENT-DEFLECTION PROGRAM USING PLFD

```

%Program: Moment-deflection using PLFD
%Author: Muhammad Fahim and Zia Razzaq
clc;
clear;
%-----
% Data
L=24;%clear length of specimen
Lo=6;%distance from specimen end to center of gimbal.
Lt=L+2*Lo;%distance between centerlines of gimbals.
np=12; %No of segments
hi=Lt/(np);%height of each segment.
Mt=[0 0.48 0.72 1.20 1.44 1.68 2.16 2.40];%Applied moment at the top.
% Main program
Mz=zeros(1,length(np+1));
phi=zeros(1,length(np+1));
del_Mid=zeros(1,length(Mt));
for k=1: numel(Mt)
    z=0;
    for i=1:np+1
        %-----
        % moment and curvature at sections of specimen
        Mz(i)=Mt(k)*((Lt-z*hi)/(Lt));%moment at each section
        phi(i)=0.1438*Mz(i);
        z=i;
    end
    %Coefficient matrix, made for 12 segments and 13 stations
    %
    C = [1  1  2  3  4  5  6  7  8  9  10  11  12  13
         0  -2  1  0  0  0  0  0  0  0  0  0  0  0;... %1
         0  1  -2  1  0  0  0  0  0  0  0  0  0  0;... %2
         0  0  1  -2  1  0  0  0  0  0  0  0  0  0;... %3
         0  0  0  1  -2  1  0  0  0  0  0  0  0  0;... %4
         0  0  0  0  1  -2  1  0  0  0  0  0  0  0;... %5
         0  0  0  0  0  1  -2  1  0  0  0  0  0  0;... %6
         0  0  0  0  0  0  1  -2  1  0  0  0  0  0;... %7
         0  0  0  0  0  0  0  1  -2  1  0  0  0  0;... %8
         0  0  0  0  0  0  0  0  1  -2  1  0  0  0;... %9
         0  0  0  0  0  0  0  0  0  1  -2  1  0  0;... %10
         0  0  0  0  0  0  0  0  0  0  1  -2  1  0;... %11
         0  0  0  0  0  0  0  0  0  0  0  1  -2  0;... %12
         0  0  0  0  0  0  0  0  0  0  0  0  1  1];... %13
    %-----
    ui = C\((-hi^2)*(phi')); %ui=deflection at each joints
    del_Mid(k) = ui(7);%u(7) corresponds to the deflection at mid height.
    % Output
    disp('=====')
    disp('Applied moment (k-in) = ')
    disp(Mt(k))
    disp('Deflection at midheigh (in) = ')
    disp(del_Mid(k))
end %end of for loop
%disp(ui)
plot(del_Mid,Mt)

```

VITA

Muhammad Fahim
Civil Engineering Department
University of Engineering and Technology, Peshawar, Pakistan.

Muhammad Fahim was born in Charsaddah, Khyber Pukhtoonkhwa, Pakistan on January 21, 1985. He received his Bachelor's degree in Civil Engineering (November 2007) and Master's degree in Structural Engineering (May 2010) from University of Engineering and Technology (UET), Peshawar, Pakistan. After graduation, Muhammad joined UET as Lecturer and taught various courses. Muhammad joined ODU in the fall of 2011 to pursue a PhD degree program in Civil Engineering. He has published one journal paper, coauthor another journal paper and one conference paper. His research interests include retrofitting and rehabilitation of concrete structures with Fiber Reinforced Polymers, earthquake resistant design of reinforced concrete and masonry structures, and behavior and fracture studies of high strength concrete members.